Supramolecular Templating of Mesoporous Zirconia-based Nanocomposite Catalysts

by

Michael Sha-Nang Wong

M. S. Chemical Engineering Practice
Massachusetts Institute of Technology, 1997

B. S., Chemical Engineering
California Institute of Technology, 1994

Submitted to the Department of Chemical Engineering in Partial Fulfillment of the Requirements for the Degree of

Doctor of Philosophy in Chemical Engineering

at the

MASSACHUSETTS INSTITUTE OF TECHNOLOGY

June 2000

Author:_____
Department of Chemical Engineering
May 24, 2000

Certified by:_____
Professor Jackie Y. Ying
Associate Professor of Chemical Engineering
Thesis Supervisor

Accepted by:_____
Professor Robert E. Cohen
St. Laurent Professor of Chemical Engineering
Chairman, Committee for Graduate Studies

Supramolecular Templating of Mesoporous Zirconia-based Nanocomposite Catalysts

by

Michael Sha-Nang Wong

M. S. Chemical Engineering Practice
Massachusetts Institute of Technology, 1997

B. S., Chemical Engineering
California Institute of Technology, 1994

Submitted to the Department of Chemical Engineering
on May 24, 2000 in Partial Fulfillment of the
Requirements for the Degree of Doctor of Philosophy in
Chemical Engineering

Abstract

Acid catalysis forms the basis of major hydrocarbon reactions in the petroleum industry, including paraffin isomerization, catalytic cracking, and alkylation. The environmental problem associated with the refining of hydrocarbons stems from the corrosive catalysts relied upon by many acid catalytic processes. These catalysts are environmentally dangerous, toxic, hard to handle, and hard to dispose of. Zeolites are well-known as environmentally friendly solid acid catalysts but they suffer from deactivation. Zirconia is of particular interest in acid catalysis because its surface acidic properties can be flexibly tailored. However, the zirconia-based materials typically have low surface areas and poorly controlled textural properties. This thesis reports on the design and synthesis of nanostructured zirconia-based materials through the development of supramolecular templating chemistry. The unique surface and structural properties of these zirconia-based mesoporous materials are related to their activities in solid acid catalysis. The three systems of interest, (i) phosphated zirconia, (ii) zirconia-silica, and (iii) tungstated zirconia, represent mesoporous materials of different acidic strengths and thermal stabilities.

The synthesis of mesoporous phosphated zirconia was achieved through the use of alkylphosphate surfactants and zirconium n-propoxide. The surfactant tail groups self-organized via hydrophobic interaction to form micellar cores, around which the alkoxide hydrolyzed and condensed to form an organic-inorganic mesostructure. The phosphate head group reacted with the zirconium alkoxide to form a covalent linkage, which was found necessary for formation of the mesostructure. The phosphate head group allowed the surfactant to be removed without mesostructure collapse and enhanced the thermal stability of the porous phosphated zirconia framework. The phosphate groups also enhanced the surface acidity of zirconia, and mesoporous phosphated zirconia was demonstrated to have moderate acidity.

Stronger acidity was successfully achieved through the synthesis of mesoporous zirconia-silicates with high thermal stability, well-defined pores, and a Zr content of up to 20 wt%. The supramolecular templating chemistry utilized was sensitive to the synthesis pH and the nature of the Zr salt precursor. Extremely low pH's were found an important synthesis parameter for controlling the amount of Zr incorporated. The Zr cations were highly dispersed throughout the silicate framework. These Zr-doped silicates were active for acid and oxidation catalysis. Surface sulfates further enhanced the acidic strength and isomerization activity.

Mesoporous tungstated zirconia was successfully produced through a novel surfactant/colloid templating approach. This new synthesis route involved the cooperative self-assembly of a metatungstate salt, zirconia colloid particles, and triblock copolymer surfactants. The metatungstate species bound to the zirconia nanoparticles and the polymer surfactant to create the mesostructure. The removal of the templating surfactants via calcination was accomplished without collapse of the pore structure. Structural stability came from the incorporation of crystalline zirconia nanoparticles in the mesoporous framework. Other tungstated metal oxides could also be derived by surfactant/colloid templating, illustrating the generality of this synthetic route for the synthesis of two-component oxide nanocomposites. These materials demonstrated the successful integration of nanoporosity and nanocrystallinity through wet-chemical processing techniques.

Thesis Supervisor: Jackie. Y. Ying
Title: Associate Professor of Chemical Engineering

Acknowledgments

I wish to thank Prof. Jackie Ying for being my advisor, mentor and friend. She was instrumental in my personal and professional development, and I cannot thank her enough for that. I would like to acknowledge the members of my thesis committee, Prof. T. Alan Hatton, Prof. Klavs F. Jensen, and Prof. Charles N. Satterfield, for their advice and constructive criticism over the course of my graduate studies.

I would also like to acknowledge my colleagues in the Nanostructured Materials Research Laboratory with whom I have thoroughly enjoyed working. First, I thank my classmates Dr. Andrey Zarur, Dr. Mark Fokema, Dr. Larry Panchula, Dr. Chen-Chi Wang, and Ed Ahn for their friendship and support. They made my experience in the group an unforgettable one. I want to acknowledge the two MIT undergraduates who worked under my supervision, Howard Huang and Esther Jeng. They contributed greatly to my thesis work, and were a joy to teach and to work with. I had the great pleasure of working with the first doctoral students of the Nano Group, Dr. Ken Bryden, Dr. Doron Levin, Dr. Darren Castro, and Dr. Lei Zhang, and I thank them for all their help. I would like to acknowledge the members of NMRL who have contributed to my research: Dr. David Antonelli, Ruma Chakravorty, Nate Gleason, Dr. Deijian Huang, Henry Hwu, Tom Lancaster, John Lettow, Justin McCue, Dr. Christian Mehnert, Suniti Moudgil, Duane Myers, Dr. Atsushi Nakahira, Pemakorn Pitukmanorom, Wolfgang Rupp, Neeraj Sangar, Yee Su, Dr. Tao Sun, Jason Sweeney, Steve Weiss, Dr. Jinsuo Xu, and Todd C. Zion.

I would like to thank Mike Frongillo for his friendship and for teaching me the ways of electron microscopy. I thank other staff members of the MIT CMSE, Dr. Tony Garratt-Reed, Libby Shaw, Peter Kloumann, and Joe Adario, for their expertise and assistance with various characterization techniques. I thank Ellen Weene, Arline Benford, Joan Chisholm, and Carol Phillips for their support and friendship, and especially Linda Mousseau, for taking care of the group. I thank Janet Fischer and Elaine Aufiero for their help throughout my years in the Department, especially during the last few months prior to the conclusion of my thesis. I acknowledge Prof. Israel Wachs and Dr. Jih-Mirn Jehng of Lehigh University for being so generous with their knowledge and time. Financial support from the Packard Foundation and the Office of Naval Research is appreciated.

I found great friends in Dr. Gary Adamkiewicz, Dr. Mark Angelino, Dr. Seth Rodgers, and Dr. Raj Venkataramani. They made the good times great, and the rough times bearable. I thank the many who have passed through the "1 Fifth Chateau," for making my five years of living there something to remember.

My parents, Gin and Kit, have always supported and encouraged me to be my best, and always helped to remind me that there is more to life than work. My brothers David and Allen, and my sister Karine and her husband Ted, have likewise shown their love and support. I thank Susan Shi for all her love, support, and patience. It is through her that I learned to become a better person. To my family and Susan I dedicate this thesis.

Contents

List of Figures

List of Tables

List of Symbols

E_g	band-gap energy
n	carbon number of amphiphile
a_0	center-to-center repeat distance
c	concentration
X^-	counteranion
d_{hk0}	d-spacing of (hk0) XRD peak
d_{100}	d-spacing of main (100) XRD peak
a_0	effective head group area
$h\nu$	incident photon energy
I	ionic strength
IP	ionization potential
$F(R_\infty)$	Kubelka-Munk function
M^+	metal cation
h,k	Miller indices
I^-	negatively-charged inorganic precursor
S^-	negatively-charged surfactant head group
S^0	neutral surfactant
V	overall volume of the surfactant
g	packing parameter
pzc	point-of-zero charge
S^+	positively-charged surfactant head group
I^+	positively-charged inorganic precursor
R_∞	reflectance at infinite thickness
Q^n	Si cation bonded to *n* other Si cations via oxygen
l	surfactant chain length
I^0	uncharged inorganic precursor
z	valence charge
λ	wavelength

Chapter 1. Background and Research Motivation

1.1 Porous Materials

The general class of inorganic porous materials has found its place in applications of heterogeneous catalysis, separations, and adsorption [1]. Recent advances in porous materials research have come from the development of new synthetic tools and the discovery of new porous solids. Non-traditional uses of porous materials have come about as well, e.g. optical waveguides, photonic crystals, and materials for host-guest chemistry.

Porous materials are classified by IUPAC into three categories according to their pore sizes: microporous (<20 Å), mesoporous (20-500 Å), and macroporous (>500 Å) [2]. With pore sizes on the order of small molecules, inorganic microporous materials include molecular sieves and activated carbon. Molecular sieve materials, typified by zeolites, have outstanding structural, surface, and size-selective properties that are desirable for catalytic and separation processes. Macroporous materials, such as porous glasses, are on the other end of the pore size range and have less utility in catalysis.

Mesoporous materials are of interest in applications in which deficiencies of zeolites arise, with pore size limitation being the most obvious. Traditional examples of mesoporous materials are pillared layered solids and aerogels. While the pores are larger, these materials lack the extremely narrow pore size distributions found in zeolites. The lack of pore size uniformity reduces the usefulness of these mesoporous materials in catalysis (e.g. they do not provide for size and shape selectivity), and limits their potential in other applications. Constructing mesoporous materials with controlled, uniform pore sizes remained a synthetic challenge until the announced discovery of MCM-41 in 1992.

1.2 Mesoporous Materials through Supramolecular Templating

Mesoporous (alumino)silicate MCM-41 and its related M41S group of materials first reported by the researchers at Mobil Research and Development Corporation have been the subject of great interest in the past decade [3]. These mesoporous materials, with well-defined pore sizes of 15-100 Å, break past the pore size constraint (<15 Å) of microporous zeolites. Among the many remarkable properties of MCM-41 are the precise control and uniformity of the pore sizes, the ordering of pore channels into a hexagonal packing, and the

extremely high surface areas (~1200 $m^2 g$) (Figure 1.1 [3b]). An in-depth review of supramolecular templating of mesoporous materials is provided by Ying *et al* [4].

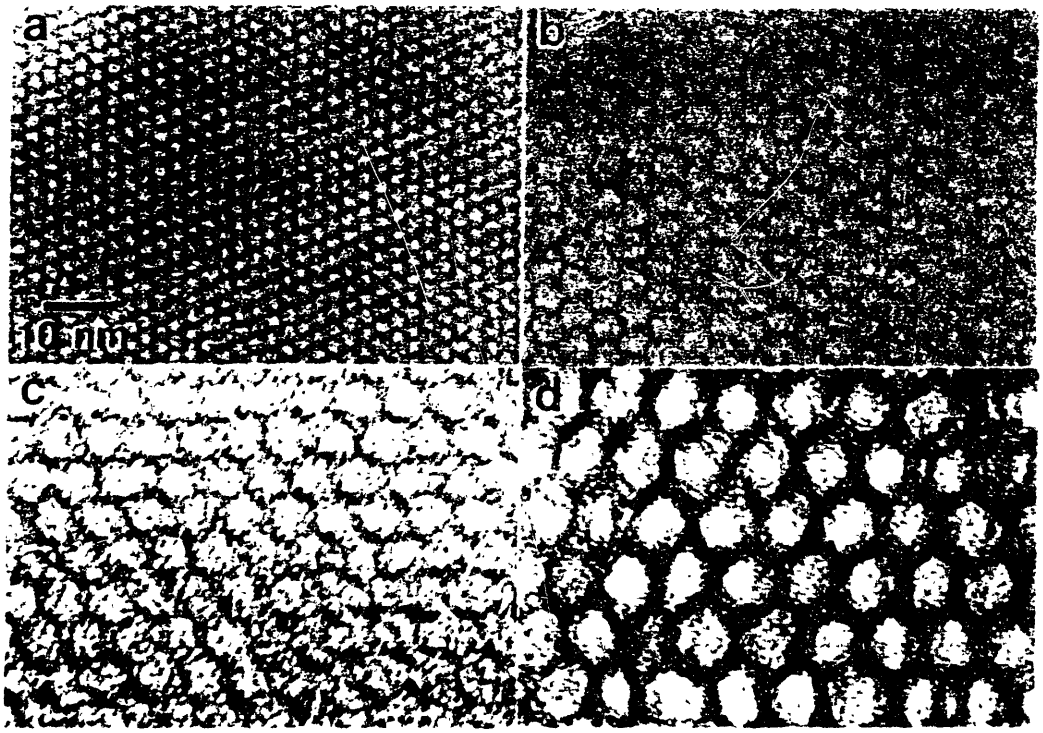

Figure 1.1. TEM images of MCM-41 with different pore sizes [3b].

MCM-41 has also ushered in a new approach in materials synthesis, in which self-assembled surfactant aggregates, or supramolecular assemblies, are employed as the structure-directing agents, instead of using single molecules as templating agents as in the case of zeolites. Surfactants are organic molecules that contain a hydrophilic functionality ("head group") and a long hydrocarbon chain ("tail group"). The molecules aggregate into micelles in an aqueous solution to minimize the unfavorable interactions between the tail group and water, and they can further self-organize into highly ordered liquid crystal (LC) phases.

1.2.1 Mechanism of Formation

Generally, MCM-41 is prepared by combining together appropriate amounts of a silica source (e.g. tetraethylorthosilicate (TEOS), Ludox, fumed silica, sodium silicate), a quaternary ammonium surfactant (e.g. cetyltrimethylammonium bromide (CTAB)), a base

(e.g. sodium hydroxide (NaOH), tetramethylammonium hydroxide (TMAOH)), and water. Aging the mixture at elevated temperatures results in a solid precipitate. This organic-inorganic mesostructured product is then recovered and calcined at 540 °C to burn off the surfactant, yielding mesoporous MCM-41 silicate.

A "liquid crystal templating" (LCT) mechanism was proposed by the Mobil researchers, based on the similarity between the M41S materials and liquid crystalline surfactant assemblies, i.e. lyotropic phases [3]. Traits common to M41S and LC phases were the dependence on the hydrocarbon chain length of the surfactant tail group [5], the effect of varying surfactant concentrations, and the influence of organic swelling agents. Two mechanistic pathways for MCM-41 formation were postulated by Beck *et al.*: (1) the silicate precursor species occupies the region between the micellar rods in a pre-existing hexagonal lyotropic LC phase; and (2) the inorganics mediate the ordering of the surfactants into the hexagonal arrangement in some manner (Figure 1.2) [3b].

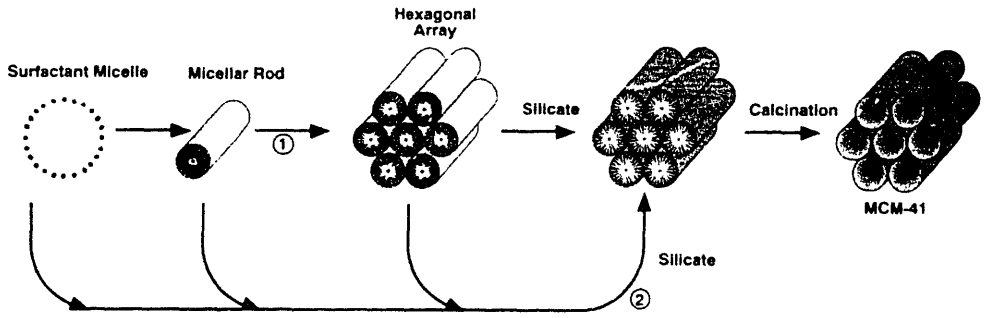

Figure 1.2. Liquid crystal templating mechanism proposed for MCM-41 formation [3b].

The negatively-charged silicate species interact with the positively-charged ammonium head groups through electrostatic interaction and condense into a solid, continuous framework at the high pH's used. The resulting organic-inorganic mesostructure could be viewed as a hexagonal array of surfactant micellar rods embedded in a silica matrix. Removal of the surfactant produces the mesoporous MCM-41 framework. The mesopores can be tuned in diameter by using longer surfactant molecules and/or adding an oil-like compound such as benzene or mesitylene as swelling agents (Figure 1.1).

Pathway (1) has since been known not to have taken place because the surfactant concentrations used were far below the critical micelle concentration (CMC) required for

hexagonal LC formation [6]. This mechanistic pathway was later shown possible under special synthesis conditions [7]. Pathway (2) of the LCT mechanism was postulated as a cooperative self-assembly of the ammonium surfactants and the silicate precursor species, i.e. the silicate species promoted LC phase formation below the CMC. This pathway was confirmed by Firouzi *et al.* [8]. They showed that the silicate anions ion-exchanged with the surfactant halide counterions, forming a "silicatropic liquid crystal" (SLC) phase composed of silicate-encrusted cylindrical micelles. Heating the SLC caused the silicates to condense irreversibly into MCM-41 mesostructure.

A general model of formation proposed by Huo *et al.* [9] focused on the electrostatic interactions between the inorganic precursor *I* and the surfactant head group *S*. The formation of MCM-41 can be categorized as the S^+I^- pathway. Supramolecular-templated materials were found possible through other charge interaction pathways: S^+I^+, $S^+X^-I^+$ (X^- is a counteranion), and $S^-M^+I^-$ (M^+ is a metal cation).

Another aspect of mesophase formation is the manner in which the surfactant tail groups pack in the material. Huo *et al.* [10] applied the concept of an effective surfactant packing parameter $g = V/a_0l$ used for lyotropic LC phases to the silicate mesophases [11]. The packing parameter can be used to predict the phase of a given LC system as a first approximation; it is affected by the overall volume V of the surfactant, the effective head group area a_0, and the surfactant chain length l. Changing the molar ratio of surfactant to silicon precursor leads to the other M41S materials [12], such as MCM-48 and MCM-50, which possess a cubic *Ia3d* mesostructure and a lamellar mesostructure, respectively [13].

There is still a lack of consensus on the mechanism of mesostructure formation, as other models have been postulated: silicate rod assembly [14], silicate layer puckering [15], charge density matching [16,17], folding of layered sheets [18], and silicate rod clustering [19]. On the most common level, however, these models are predicated upon the presence of surfactants in a solution to guide the formation of the inorganic mesostructure from the solubilized inorganic precursors.

1.2.2 Pure and Doped Mesoporous Silicates

Various types of mesoporous silicates have been reported, taking advantage of the flexibility of the supramolecular templating chemistry: MSU materials by Pinnavaia and co-

workers prepared through the hydrogen-bonding interaction of an alkylamine [20] or of a polyethylene oxide surfactant [21] and TEOS; SBA materials by Stucky and co-workers prepared through charge interactions under low-pH conditions [9,22]; and disordered mesoporous silicates exhibiting a "sponge" (L_3) phase [23], similar to KIT-1 by Ryoo *et al.* [24].

As MCM-41 and other pure mesoporous silicates contain no specific catalytically active sites, there is great interest in doping these materials with active metal species. Metal dopant loadings typically reach values of 2-5 wt% through simple addition of the appropriate metal precursor into the synthesis mixture. Higher doping levels can be attained for particular metal cations, such as Al [25-27] and Nb [28]. However, there can be problems with significantly reduced mesostructure stability, presence of extraframework metal cations, or formation of secondary oxides in the heavily doped silicate systems.

1.2.3 Mesoporous Non-Silicates

Non-silicate-containing metal oxides with well-ordered mesopores provide uniquely tailored features, such as redox capability, surface acidity, attractive absorbent properties, and unique optical and electronic characteristics. The successful application of the supramolecular templating synthesis technique to non-silicates was not at all obvious, however. Initial studies found possible surfactant-inorganic mesostructures for metal cations such as Sb, Fe, Zn, Pb, W, and Mo [9,29], but most were layered and could not yield porous materials when the surfactant was removed. The few hexagonal phases collapsed upon surfactant removal (either by solvent extraction or by calcination), possibly due to the incomplete condensation and thinness of the pore walls [30-32], and to the propensity of the amorphous pore walls to crystallize, breaking down the pore structure in that process.

Ying and co-workers successfully developed a supramolecular templating method for transition metal oxides. The "ligand-assisted templating" route was based on the covalent bond interactions between a surfactant head group and the metal alkoxide precursor. They applied this to TiO_2 [33], Nb_2O_5 [34,35], Ta_2O_5 [36], and ZrO_2 [37,38] syntheses, and termed the resulting mesoporous materials "TMS," or Tech Molecular Sieves. Through this concept of covalent interactions, they were also able to derive microporous Nb_2O_5 using short-chained and bifunctional alkylamines [39,40]. Stucky and co-workers recently provided a new

supramolecular templating method applicable to a wide range of metal oxides, including silica [41]. They were able to bypass many of the synthetic difficulties of solution chemistry by preparing their materials through a non-aqueous route.

1.3 Heterogeneous Acid Catalysis

Heterogeneous catalysis has played a critical role in many chemical processes. The impact of heterogeneously catalyzed processes on the global economy has been estimated at 20% of the world GNP, or ca. $5 trillion/year [42]. The main industrial catalytic applications are petroleum refining, chemical production, and environmental protection. Petroleum refining involves the largest volume of materials processed, with the world oil refining capacity in excess of 3.6×10^{12} kg/year (at end of 1993) [43,44]. As fossil fuel is a finite energy source, there is the need for developing new and improved catalysts to meet the challenges of refining crude oil more effectively.

Acid catalysts play a crucial role in the refining of petroleum. Hydrocarbon feedstocks are converted into higher-value products through a number of processes. A generalized flowsheet for a petroleum refinery is shown in Figure 1.3 [45]. These processes, such as paraffin isomerization, alkylation, catalytic cracking, and naphtha reforming, rely on acidic materials to catalyze the reactions [43,46]. Improvements in catalytic performance would lead to more efficient use of the diminishing raw materials.

Environmental problems upstream of the refined hydrocarbon products have also spurred the search for improved acid catalysts. In the production of motor-grade fuel through alkylation of isobutane with alkenes, sulfuric acid and hydrofluoric acid are used as the catalysts. These liquid mineral acids are corrosive, dangerous to handle, and difficult to dispose of. Even some industrial solid acid catalysts are environmentally harmful. The bifunctional Pt-doped chlorinated alumina catalyst used in the n-butane isomerization process requires the addition of chlorinated compounds to maintain catalytic activity as it leaches corrosive hydrochloric acid during use. More significant are the problems concerning the downstream use of the hydrocarbon products, especially the deleterious emissions from the combustion of gasoline motor fuel. Addressing this was the Clean Air Act Amendments of 1990, which mandated the reformulation of motor fuel gasoline (40-50% of all petroleum

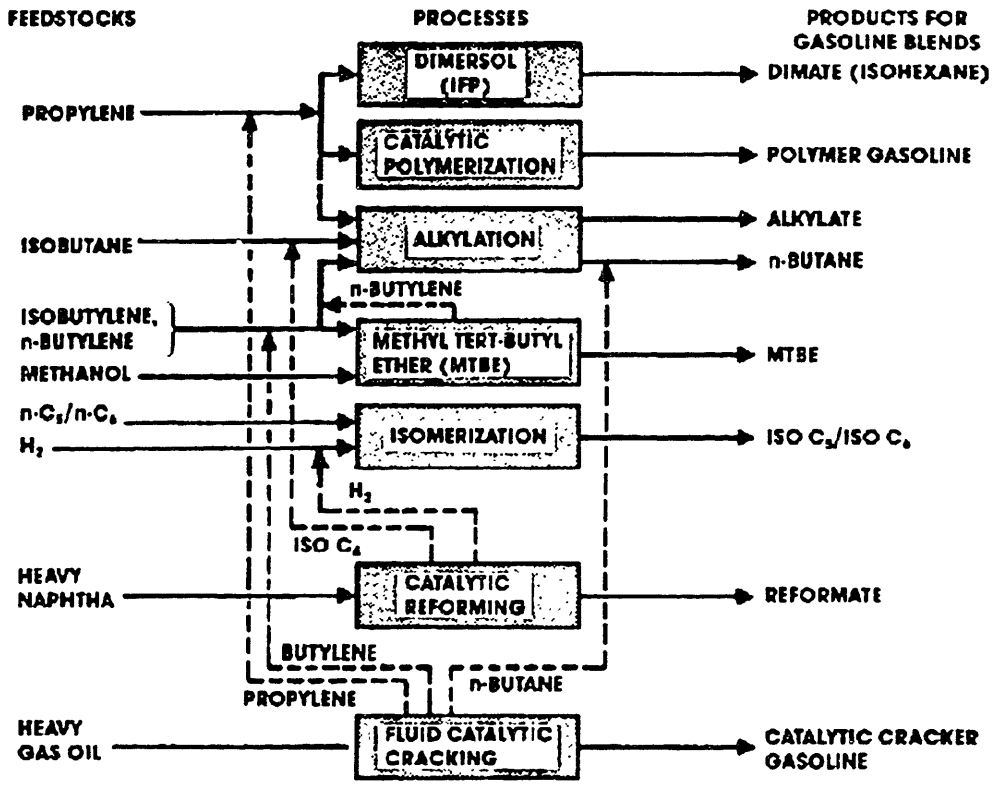

Figure 1.3. Schematic of petroleum refinery processes [45].

products in the U.S.). As a result, demand for particular blend components has heightened, increasing the load on the existing catalytic processes.

1.4 Microporous Zeolite Catalysts

Zeolites are microporous, crystalline acidic solids composed of AlO_4 and SiO_4 tetrahedra arranged around highly ordered channels and/or cavities [47,48]. Surface acidity is generated by protons required for charge balance of the framework and located near the Al cations. Zeolites have structural characteristics desired for solid acid catalysts, such as surface acidity, high internal surface areas, and uniform pore sizes. Examples of zeolites used as solid acids in petroleum refining include Pt/mordenite for C_5/C_6 isomerization, ZSM-5 for xylene isomerization and in methanol-to-gasoline conversion, sulfided NiMo/faujasite for hydrocracking of heavy petroleum fractions, and USY for fluidized catalytic cracking [43,44]. Zeolites are presently being investigated for other acid-catalyzed processes [49]. Major difficulties in employing zeolites as acid catalysts lie in their tendency to deactivate and their

limited usefulness in reactions involving large molecules. Zeolites are also being studied for other types of organic reactions. A notable example is titanium-containing silicalite (TS-1), which is used for industrial-scale oxidation of phenol with H_2O_2 to produce catechol and hydroquinone [50].

There are particular restrictions in the development of zeolites and molecular sieves as new catalysts. There are about 90 unique framework topologies found in molecular sieves, as tabulated by the International Zeolite Association Structure Commission [51]. The largest pore openings available are 7.5 Å × 10 Å for aluminosilicates (UTD-1), 12-13 Å for aluminophosphates (VPI-5), and 14.2 Å for naturally occurring zeolitic materials (cacoxenite). To obtain molecular sieves with a different pore structure or with larger pores obligates the synthesis of entirely new zeolitic structures. Another challenge is the lack of compositional flexibility, limiting zeolitic materials to aluminosilicates, aluminophosphates (AlPO's), silicoaluminophosphates (SAPO's), and their respective metal-doped analogues.

1.5 Research Motivation

Given the intrinsic challenges in investigating new zeolitic materials for heterogeneous catalysis, great opportunities exist for the development of novel mesoporous catalysts through supramolecular templating synthesis.

Of great interest to solid acid catalysis is zirconium oxide, a transition metal oxide known for its tunable surface acidic properties. Pure zirconia contains weak acid sites, and cannot catalyze reactions requiring moderate to strong acidity, such as isomerization or cracking. However, the acid strength of zirconia can be increased by combining with surface anionic species or by doping with a second metal oxide. These zirconia-based materials exhibit activity for reactions like the isomerization of n-butane and the cracking of octane [52,53]. While they have been studied as potential acid catalysts, little attention has been paid to their microstructure and textural properties. Improved catalytic performance might be achieved by well-defined mesoporous zirconia-based materials prepared through supramolecular templating.

One approach to mesoporous zirconia-based materials is to prepare pure mesoporous zirconia and to add a surface dopant in a second processing step. However, many studies have found that zirconia is very difficult to prepare in the supramolecular-templated

mesoporous form. The slight improvement in textural properties of the resultant templated zirconia compared to conventional zirconia materials (prepared through precipitation) does not justify the extra processing steps. Also, this two-step approach is not amenable to mesoporous doped zirconia. The supramolecular templating chemistry for doped zirconia synthesis is not well-developed.

In this thesis, supramolecular templating is applied to derive three zirconia-based systems that exhibit different surface acidic properties: (1) phosphated zirconia, (2) zirconia-silica, and (3) tungstated zirconia. The application of supramolecular templating to these systems poses interesting synthetic challenges, and we have developed the appropriate chemistries to achieve successfully each class of materials. The unique surface and structural properties of these templated zirconia-based materials are further demonstrated and related to their activities in solid acid catalysis.

1.6 References

[1] Barton, T. J.; Bull, L. M.; Klemperer, W. G.; Loy, D. A.; McEnaney, B.; Misono, M.; Monson, P. A.; Pez, G.; Scherer, G. W.; Vartuli, J. C.; Yaghi, O. M. *Chem. Mater.* **1999**, *11*, 2633.

[2] Behrens, P. *Adv. Mater.* **1993**, *5*, 127.

[3] (a) Kresge, C. T.; Leonowicz, M. E.; Roth, W. J.; Vartuli, J. C.; Beck, J. S. *Nature* **1992**, *359*, 710. (b) Beck, J. S.; Vartuli, J. C.; Roth, W. J.; Leonowicz, M. E.; Kresge, C. T.; Schmitt, K. D.; Chu, C. T.-W.; Olsen, D. H.; Sheppard, E. W.; McCullen, S. B.; Higgins, J. B.; Schlenker, J. L. *J. Am. Chem. Soc.* **1992**, *114*, 10834. (c) Kresge, C. T.; Leonowicz, M. E.; Roth, W. J.; Vartuli, J. C. US Patent No. 5,098,684, 1992.

[4] Ying, J. Y.; Mehnert, C. P.; Wong, M. S. *Angew. Chem. Int. Ed.* **1999**, *38*, 56.

[5] Beck, J. S.; Vartuli, J. C.; Kennedy, G. J.; Kresge, C. T.; Roth, W. J.; Schramm, S. E. *Chem. Mater.* **1994**, *6*, 1816.

[6] Vartuli, J. C.; Kresge, C. T.; Leonowicz, M. E.; Chu, A. S.; McCullen, S. B.; Johnson, I. D.; Sheppard, E. W. *Chem. Mater.* **1994**, *6*, 2070.

[7] Attard, G. S.; Glyde, J. C.; Göltner, C. G. *Nature* **1995**, *378*, 366.

[8] Firouzi, A.; Kumar, D.; Bull, L. M.; Besier, T.; Sieger, P.; Huo, Q.; Walker, S. A.; Zasadzinski, J. A.; Glinka, C.; Nicol, J.; Margolese, D.; Stucky, G. D.; Chmelka, B. F. *Science* **1995**, *267*, 1138.

[9] (a) Huo, Q.; Margolese, D. I.; Ciesla, U.; Feng, P.; Gier, T. E.; Sieger, P.; Leon, R.; Petroff, P. M.; Schüth, F.; Stucky, G. D. *Nature* **1994**, *368*, 317. (b) Huo, Q.; Margolese, D. I.; Ciesla, U.; Demuth, D. G.; Feng, P.; Gier, T. E.; Sieger, P.; Firouzi, A.; Chmelka, B. F.; Schüth, F.; Stucky, G. D. *Chem. Mater.* **1994**, *6*, 1176.

[10] Huo, Q.; Margolese, D. I.; Stucky, G. D. *Chem. Mater.* **1996**, *8*, 1147.

[11] Israelachvili, J. N. *Intermolecular and Surface Forces*, 2nd Ed.; Academic Press: London, 1992.

[12] Vartuli, J. C.; Schmitt, K. D.; Kresge, C. T.; Roth, W. J.; Leonowicz, M. E.; McCullen, S. B.; Hellring, S. D.; Beck, J. S.; Schlenker, J. L.; Olsen, D. H.; Sheppard, E. W. *Chem. Mater.* **1994**, *6*, 2317.

[13] Vartuli, J. C.; Kresge, C. T.; Roth, W. J.; McCullen, S. B.; Beck, J. S.; Schmitt, K. D.; Leonowicz, M. E.; Lutner, J. D.; Sheppard, E. W. In *Proceedings of the 209th ACS National Meeting, Division of Petroleum Chemistry*, 1995; p. 21.

[14] Chen, C.-Y.; Burkett, S. L.; Li, H.-X.; Davis, M. E. *Microporous Mater.* **1993**, *2*, 27.

[15] Steel, A.; Carr, S. W.; Anderson, M. W. *J. Chem. Soc., Chem. Commun.* **1994**, 1571.

[16] Monnier, A.; Schüth, F.; Huo, Q.; Kumar, D.; Margolese, D.; Maxwell, R. S.; Stucky, G. D.; Krishnamurty, M.; Petroff, P.; Firouzi, A.; Janicke, M.; Chmelka, B. F. *Science* **1993**, *261*, 1299.

[17] Stucky, G. D.; Monnier, A.; Schüth, F.; Huo, Q.; Margolese, D.; Kumar, D.; Krishnamurty, M.; Petroff, P.; Firouzi, A.; Janicke, M.; Chmelka, B. F. *Mol. Cryst. Liq. Cryst.* **1994**, *240*, 187.

[18] (a) Yanagisawa, T.; Shimizu, T.; Kuroda, K.; Kato, C. *Bull. Chem. Soc. Jpn.* **1990**, *63*, 988. (b) Inagaki, S.; Fukushima, Y.; Kuroda, K. *J. Chem. Soc., Chem. Commun.* **1993**, 680. (c) Fukushima, Y.; Inagaki, S. *Mater. Sci. Eng. A* **1996**, *217*, 116.

[19] Regev, O. *Langmuir* **1996**, *12*, 4940.

[20] Tanev, P. T.; Pinnavaia, T. J. *Science* **1995**, *267*, 865.

[21] Bagshaw, S. A.; Prouzet, E.; Pinnavaia, T. J. *Science* **1995**, *269*, 1242.

[22] Zhao, D.; Feng, J.; Huo, Q.; Melosh, N.; Fredrickson, G. H.; Chmelka, B. F.; Stucky, G. D. *Science* **1998**, *279*, 548.

[23] McGrath, K. M.; Dabbs, D. M.; Yao, N.; Aksay, I. A.; Gruner, S. M. *Science* **1997**, *277*, 552.

[24] (a) Ryoo, R.; Kim, J. M.; Ko, C. H.; Shin, C. H. *J. Phys. Chem.* **1996**, *100*, 17718. (b) Ryoo, R.; Kim, J. M.; Shin, C. H.; Lee, J. Y. In *Progress in Zeolite and Microporous Materials*, Studies in Surface Science and Catalysis, Vol. 105; Chon, H., Ihm, S.-K., Uh, Y. S., Eds.; Elsevier: Amsterdam, 1997; p. 45.

[25] Ryoo, R.; Ko, C. H.; Howe, R. F. *Chem. Mater.* **1997**, *9*, 1607.

[26] Luan, Z.; Cheng, C.-F.; Zhou, W.; Klinowski, J. *J. Phys. Chem.* **1995**, *99*, 1018.

[27] Fu, G.; Fyfe, C. A.; Schwieger, W.; Kokotailo, G. T. *Angew. Chem. Int. Ed. Engl.* **1995**, *34*, 1499.

[28] Zhang, L.; Ying, J. Y. *AIChE J.* **1997**, *43*, 2793.

[29] Ciesla, U.; Demuth, D.; Leon, R.; Petroff, P.; Stucky, G.; Unger, K.; Schüth, F. *J. Chem. Soc., Chem. Commun.* **1994**, 1387.

[30] Stein, A.; Fendorf, M.; Jarvie, T. P.; Mueller, K. T.; Benesi, A. J.; Mallouk, T. E. *Chem. Mater.* **1995**, *7*, 304.

[31] Janauer, G. G.; Dobley, A.; Guo, J.; Zavalij, P.; Whittingham, M. S. *Chem. Mater.* **1996**, *8*, 2096.

[32] (a) Luca, V.; MacLachlan, D. J.; Hook, J. M.; Withers, R. *Chem. Mater.* **1995**, *7*, 2220. (b) Luca, V.; Hook, J. M. *Chem. Mater.* **1997**, *9*, 2731.

[33] Antonelli, D. M.; Ying, J. Y. *Angew. Chem. Int. Ed. Engl.* **1995**, *34*, 2014.

[34] Antonelli, D. M.; Ying, J. Y. *Angew. Chem. Int. Ed. Engl.* **1996**, *35*, 426.

[35] Antonelli, D. M.; Nakahira, A.; Ying, J. Y. *Inorg. Chem.* **1996**, *35*, 3126.

[36] Antonelli, D. M.; Ying, J. Y. *Chem. Mater.* **1996**, *8*, 874.

[37] Wong, M. S.; Antonelli, D. M.; Ying, J. Y. *Nanostr. Mater.* **1997**, *9*, 165.

[38] Wong, M. S.; Ying, J. Y. *Chem. Mater.* **1998**, *10*, 2067.

[39] Sun, T.; Ying, J. Y. *Nature* **1997**, *389*, 704.

[40] Sun, T.; Ying, J. Y. *Angew. Chem. Int. Ed. Engl.* **1998**, *37*, 664.

[41] (a) Yang, P.; Zhao, D.; Margolese, D. I.; Chmelka, B. F.; Stucky, G. D. *Nature* **1998**, *396*, 152. (b) Yang, P.; Zhao, D.; Margolese, D. I.; Chmelka, B. F.; Stucky, G. D. *Chem. Mater.* **1999**, *11*, 2813.

[42] Lambert, R. M. In *Chemisorption and Reactivity on Supported Clusters and Thin Films: Towards an Understanding of Microscopic Processes in Catalysis*, NATO ASI Series E, Vol. 331; Lambert, R. M., Pacchioni, G., Eds.; Kluwer: Dordrecht, 1997; p. 1.

[43] Satterfield, C. N. *Heterogeneous Catalysis in Industrial Practice*, 2nd Ed.; McGraw-Hill: New York, 1991.

[44] Martino, G.; Courty, P.; Marcilly, C. In *Handbook of Heterogeneous Catalysis*, Vol. 4; Ertl, G., Knözinger, H., Weitkamp, J., Eds.; VCH: Weinheim, 1997; p. 1801.

[45] Scherzer, J. *Octane-Enhancing, Zeolitic FCC Catalysts: Scientific and Technical Aspects*; Marcel Dekker: New York, 1990.

[46] Chianelli, R. R.; Lyons, J. E.; Mills, G. A. *Catal. Today* **1994**, *22*, 361.

[47] Davis, M. E.; Lobo, R. F. *Chem. Mater.* **1992**, *4*, 756.

[48] Thompson, R. W. In *Molecular Sieves – Science and Technology*, Vol. 1; Karge, H. G., Weitkamp, J., Eds.; Springer-Verlag: Berlin, 1998; p. 1.

[49] Dai, P.-S. E. *Catal. Today* **1995**, *26*, 3.

[50] Notari, B. *Adv. Catal.* **1996**, *41*, 253.

[51] Szostak, R. *Molecular Sieves: Principles of Synthesis and Identification*, 2nd Ed.; Blackie Academic & Professional: London, 1998.

[52] Davis, B. H.; Keogh, R. A.; Srinivasan, R. *Catal. Today* **1994**, *20*, 219.

[53] Song, X.; Sayari, A. *Catal. Rev. Sci.-Eng.* **1996**, *38*, 329.

Chapter 2. Mesoporous Phosphated Zirconia

2.1 Introduction

Much research had been devoted to the preparation of mesoporous zirconium oxide through supramolecular templating. Synthetic approaches have been based upon the concepts of electrostatic [1-4], hydrogen-bonding [5] and covalent-bond interactions [6-8]. More often than not, the resultant products were layered materials [9], making impossible the removal of the surfactant without collapse of the zirconium oxide framework. It can be produced through a surfactant-mediated "scaffolding" route but the mesopores (~30 Å) were non-uniform and poorly ordered [10]. Mesoporous zirconia can also be prepared through chemical precipitation and through supercritical drying of zirconia gels, but the pores are larger and not ordered (~100 Å) [11]. An inherent drawback of these materials lies in the facile sinterability and concomitant loss of surface area at elevated temperatures (>400 °C). The major thermodynamic driving force is the crystalline transformation of these zirconia materials to dense, low surface area monoclinic and metastable tetragonal phases [12]. The thermal stability of zirconia is improved with the introduction of surface dopants, such as phosphates [13] and sulfates [14]. Such modified zirconia exhibits higher acid strength and activity for acid-catalyzed reactions. Pure, unmodified zirconium oxide contains weak acid sites that can only catalyze dehydation and cis-trans isomerization [15]. It also has basic sites, which contribute to high activity in reactions requiring acid-base bifunctional catalysts [16,17]. However, pure zirconia cannot catalyze more acid-demanding reactions, such as paraffin cracking. In comparison, phosphated zirconia [13] is mildly acidic, and sulfated zirconia is strongly acidic, and even superacidic [14].

Ciesla *et al.* [18] and Liu *et al.* [19] independently reported the synthesis of phosphated zirconia through supramolecular templating. Their similar methods involved the preparation of a mesostructured zirconia/surfactant intermediate, which collapses upon calcination. This intermediate contains sulfates that sit between the zirconia walls and the surfactant head groups. Ion-exchanging these sulfates with phosphate anions leads to a thermally stable, porous phosphated zirconia material. Our initial studies found this material very sensitive to synthesis conditions, resulting in poor reproducibility and widely varying activity for acid-catalyzed reactions.

In this Chapter, we examined the preparation of mesoporous phosphated zirconia (Zr-TMS) through supramolecular templating based on covalent interactions [20,21]. We extended this covalent bonding approach to other anionic and non-ionic surfactants in the preparation of mesostructured zirconia. We also found that short-chained molecules too small to be regarded as true surfactants can be used as supramolecular templating agents via this synthetic approach.

2.2 Experimental Methods

2.2.1 Chemicals

Anionic and non-ionic amphiphilic compounds were used in the synthesis of mesostructured zirconium oxide. Here, the term "amphiphile" refers to surface-active compounds containing, within the same molecule, a hydrophilic head group and a hydrophobic hydrocarbon tail group of any carbon chain length; amphiphiles are generally considered surfactants when the tail group contains 8 carbons or more [22]. Carboxylate amphiphiles ($C_nH_{2n+1}COO^-$, n/2 = ½,1-9) were obtained from Aldrich Chemical (Milwaukee, WI) and were used without further purification. Dodecylsulfate surfactant ($C_nH_{2n+1}SO_4^-$, n = 12) and alkylsulfonate surfactants ($C_nH_{2n+1}SO_3^-$, n = 6,16) were obtained in sodium salt form from Aldrich. Primary amine amphiphiles ($C_nH_{2n+1}NH_2$, n = 4,6,12) were purchased from Aldrich. Phosphate compounds ($C_nH_{2n+1}PO_4^{2-}$, n = 4,8,12,16) were either synthesized [23] or obtained from Lancaster Synthesis (Windham, NH) and Johnson Matthey Alfa Aesar (Ward Hill, MA). Swelling agents (cyclohexane and toluene) and chelating agents (acetylacetone) were purchased from Aldrich. The n-propoxide form of zirconium alkoxide was used in this study, and it was introduced in a n-propanol solution (74 wt% zirconium (tetrakis)n-propoxide). Zirconium ethoxide (99+%) and isopropoxide (99+%) were also used in some experiments. The alkoxides were commercially available from Aldrich and Strem Chemicals (Newburyport, MA) and were used without further purification.

2.2.2 Synthesis

In the covalent bonding approach, the synthesis of mesostructured zirconium oxide began with the addition of a molar equivalent (unless otherwise stated) of amphiphilic compound to the zirconium n-propoxide solution. Zirconium n-propoxide is hygroscopic and

can precipitate out of solution prematurely if care is not taken to minimize its exposure to air. The mixture was quickly stirred at room temperature until the amphiphile dissolved completely. It could be heated briefly to help solubilize undissolved surfactants. Swelling agents, if any, were added at this point. Precipitation began almost immediately after deionized water was added to the solution, and the resulting mixture was stirred for 1 hr under ambient conditions. The mixture was then left to stand overnight, before aging at 80 °C for 4 days. After the aging step, the precipitate was filtered and washed with deionized water three times. The white to yellowish-white powder was finally air-dried overnight under a hood.

When alkylphosphate amphiphiles were used, precipitation occurred without the water addition step due to the loss of solubility of oligomerized zirconium precursor. The resulting mixture was vigorously stirred until a moist, cream-colored intermediate was obtained. Water was then added, and the mixture was stirred for 0.5 hr and left under static conditions overnight before aging at elevated temperatures.

To reduce the reactivity of the zirconium precursor in certain experiments, one molar equivalent of acetylacetone was added slowly to zirconium n-propoxide, producing zirconium acetylacetonate (tris)n-propoxide [24]. Heat was generated by the reaction and the resulting solution was orange-colored. Amphiphilic compounds were then added to this zirconium chelate as 5 wt% aqueous solutions. These steps comprise the modified sol-gel method, as reported in the synthesis of Ti-TMS1 [6].

2.2.3 Surfactant Template Removal

Unless otherwise noted, the as-synthesized material was calcined at 400 °C under flowing nitrogen for 3 hr and then under air for another 3 hr (ramp = 2 °C/min). In differential thermal analysis (DTA) experiments, calcination under air is exothermic due to the combustion of organics; calcination under nitrogen is an endothermic process as the organics undergo pyrolysis. Calcination was also carried out at higher temperatures. Depending on the amphiphiles used in the synthesis, alternative techniques in template removal included washing the powders with acidic and basic solutions (1.0-3.3 M solutions) and Soxhlet extraction in toluene.

2.2.4 Characterization

Powder X-ray diffraction (XRD) data were recorded on a Siemens D5000 θ-θ diffractometer using nickel-filtered CuK_α radiation with wavelength λ = 1.5406 Å. Diffraction patterns were collected under ambient conditions for 2θ = 1.6° to 20.0° with a resolution of 0.04°.

Transmission electron micrographs (TEM) were taken on a JEOL 2000FX transmission electron microscope equipped with a lanthanum hexaboride (LaB_6) gun operating at an accelerating voltage of 200 kV and with an objective aperture of 50 μm. Samples for TEM studies were ground and supported on a carbon-coated copper grid.

Nitrogen adsorption isotherms were obtained at 77 K on a Micromeritics ASAP 2010 Gas Sorption and Porosimetry System. Samples were normally prepared for measurement by degassing at 150 °C under vacuum until a final pressure of 1×10^{-3} Torr was reached. BET surface areas were determined over a relative pressure range of 0.05 to 0.20 [25]. Mesopore size distributions were calculated from the adsorption branch of the isotherms using the BJH (Barrett-Joyner-Halenda) method [26].

Non-simultaneous thermogravimetric analysis (TGA) and differential thermal analysis (DTA) were performed on a Perkin-Elmer Series 7 Thermal Analysis System. A ramp rate of 2 °C/min was used. Purified nitrogen, oxygen, and air were employed as the purge gases.

Fourier-transform infrared (FTIR) spectroscopy was performed on a Bio-Rad FTS-60A/896 spectrometer. An MTEC Model 200 photoacoustic (PA) cell allowed non-destructive characterization of the powder samples. PA-FTIR spectra were collected at a scan speed of 5 kHz for wavenumbers of 400 to 4000 cm^{-1} with a resolution of 4 cm^{-1}. Samples were purged under a stream of helium (99.999+%).

Elemental analysis through inductively-coupled plasma atomic emission spectroscopy (ICP-AES) was performed by Huffman Laboratories (Golden, CO). Solid-state ^{31}P magic angle spinning nuclear magnetic resonance (MAS NMR) spectra were collected at 109.55 MHz for ^{31}P resonance and at 270.62 MHz for proton decoupling by Spectral Data Services, Inc. (Champaign, IL). An 85% H_3PO_4 solution was used as the external reference.

2.2.5 Catalytic Testing

Catalytic testing of Zr-TMS was done in a single-pass, downflow quartz tube reactor. The catalyst bed consisted of 50 mg of powder placed between quartz wool, on top of a porous quartz frit. Prior to reaction, the catalyst was activated under air at a temperature 50 °C above the reaction temperature for 1 h. After cooling, a feed stream of 13.4% 1-butene in helium was passed over the catalyst at a flow rate of 20 sccm. The reactor effluent was analyzed with a Hewlett-Packard 5890 gas chromatograph (GC) equipped with a flame induction detector and a HP-PLOT/Al_2O_3/KCl-deactivated capillary column (ID = 0.32 mm; length = 50 m). Product selectivities were measured at steady state. The reaction pressure was 1 atm.

2.3 Results and Discussion

The synthesis of mesostructured zirconium oxide was examined with anionic and non-ionic amphiphilic compounds [21]. Anionic amphiphiles contain multiple reactive oxygen atoms in the head group (*e.g.* phosphate, carboxylate, sulfate, and sulfonate), while the nucleophilic head groups of the non-ionic amphiphiles (*e.g.* amine) are capable of attacking the highly electrophilic zirconium atom in the alkoxide [27]. Summarized in Table 2.1 are the *d*-spacing values of zirconia mesostructures prepared with the various amphiphiles. Figure 2.1 shows the typical XRD patterns for which surfactant-containing mesostructured zirconia materials termed Zr-TMS were found possible, as prepared through the covalent-bond route.

Table 2.1. Measured d_{100}-spacings (Å) of Zr-TMS mesostructures prepared with amphiphiles of various head groups and chain lengths.

Carbon Number	Head Group				
n	$-PO_4^{2-}$	$-COO^-$	$-SO_4^-$	$-SO_3^-$	$-NH_2$
1		14.6			
2		15.4			
4	16.6	17.4			
6		20.4		17.0	
8	24.2	23.1			
10		26.2			
12	31.0	26.7	38.3		34.5
14		29.2			
16	38.4	31.3		35.0	
18		33.1			

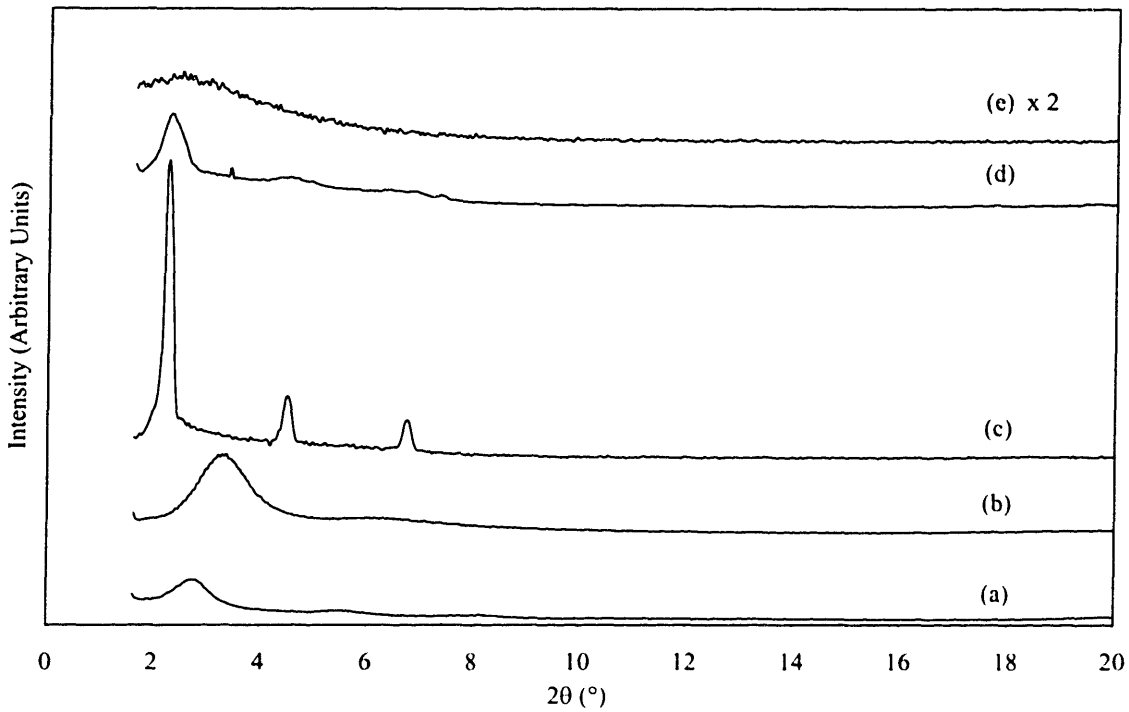

Figure 2.1. Typical XRD patterns of covalently-bonded zirconia-surfactant Zr-TMS mesostructures prepared with (a) $C_{12}H_{25}PO_4^{2-}$, (b) $C_{12}H_{25}COO^-$, (c) $C_{12}H_{25}SO_4^-$, (d) $C_{16}H_{33}SO_3^-$, and (e) $C_{12}H_{25}NH_2$ amphiphiles as the templating agents.

2.3.1 Anionic Amphiphiles: Phosphate Head Group

Alkylphosphates are expected to be highly reactive with zirconium alkoxides. There are three nucleophilic oxygens in the head group capable of attacking multiple zirconium alkoxide molecules. Indeed, phosphates (and phosphonates) are known to form layered crystalline materials with zirconium and other metal(IV) cations [28]. Dodecylphosphate was combined with one molar equivalent of zirconium n-propoxide, creating an intermediate prior to the addition of deionized water, giving a molar composition of 1.0 Zr : 1.0 surfactant : 250.0 H_2O. Deionized water was used instead of an acidic aqueous solution (pH = 1.2, HCl), as modified from our original procedure [20]. Aging at 80 °C for 96 hr yielded a mesostructured material (Figure 2.2(a)), and the XRD pattern could be indexed to a lamellar phase (d_{100} = 31.0 Å), although the broadness of the peaks did not preclude the existence of a hexagonal phase.

A lamellar-phase XRD pattern might also be exhibited by a material with tightly packed but randomly oriented pore channels [29]. Indeed, TEM studies have shown that as-synthesized Zr-TMS contained both lamellar (Figure 2.3(a)) and poorly ordered hexagonal

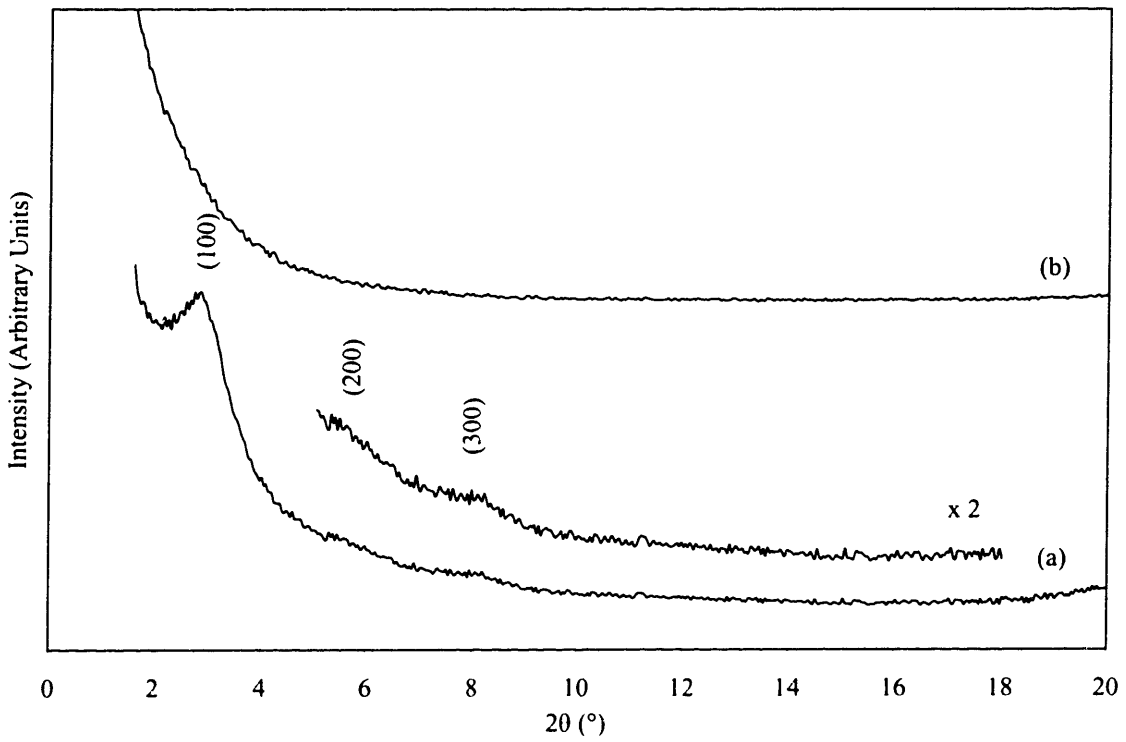

Figure 2.2. XRD patterns of Zr-TMS synthesized with $C_{12}H_{25}PO_4^{2-}$ via ligand-assisted templating route: (a) before and (b) after calcination at 400 °C in N_2, then in air.

(Figure 2.3(b)) phases. Upon calcination, an X-ray amorphous material was obtained (Figure 2.2(b)), but the resulting mesoporous material was found to have a very high BET surface area (356 m^2/g) and a BJH pore size distribution of 20-40 Å, centered at *ca.* 25 Å (see Figure 2.6(c) for the nitrogen adsorption isotherm). The aging conditions were found optimal for producing high surface area, mesoporous materials. The modified sol-gel route led to zirconia mesostructures with lower surface areas and was not examined further.

The effect of the surfactant to zirconium n-propoxide molar ratio was studied. Vartuli *et al.* [30] reported that the following different phases of M41S materials could be obtained by varying the surfactant/silicon molar ratio: 2-dimensional hexagonal *P6m* MCM-41 (<1:1), cubic *Ia3d* MCM-48 (1:1), and lamellar MCM-50 (1.2:1–1.8:1). At ratios approaching 2:1, a silicon-surfactant molecular compound was formed, instead of a condensed mesostructure. Antonelli *et al.* [7b] showed different phases of Nb-TMS materials could also be obtained by adjusting the surfactant/niobium ratio: hexagonal *P6m* Nb-TMS1 (<0.75:1), 3-dimensional hexagonal $P6_3/mmc$ Nb-TMS2 (1.25:1), and layered Nb-TMS4 (2:1).

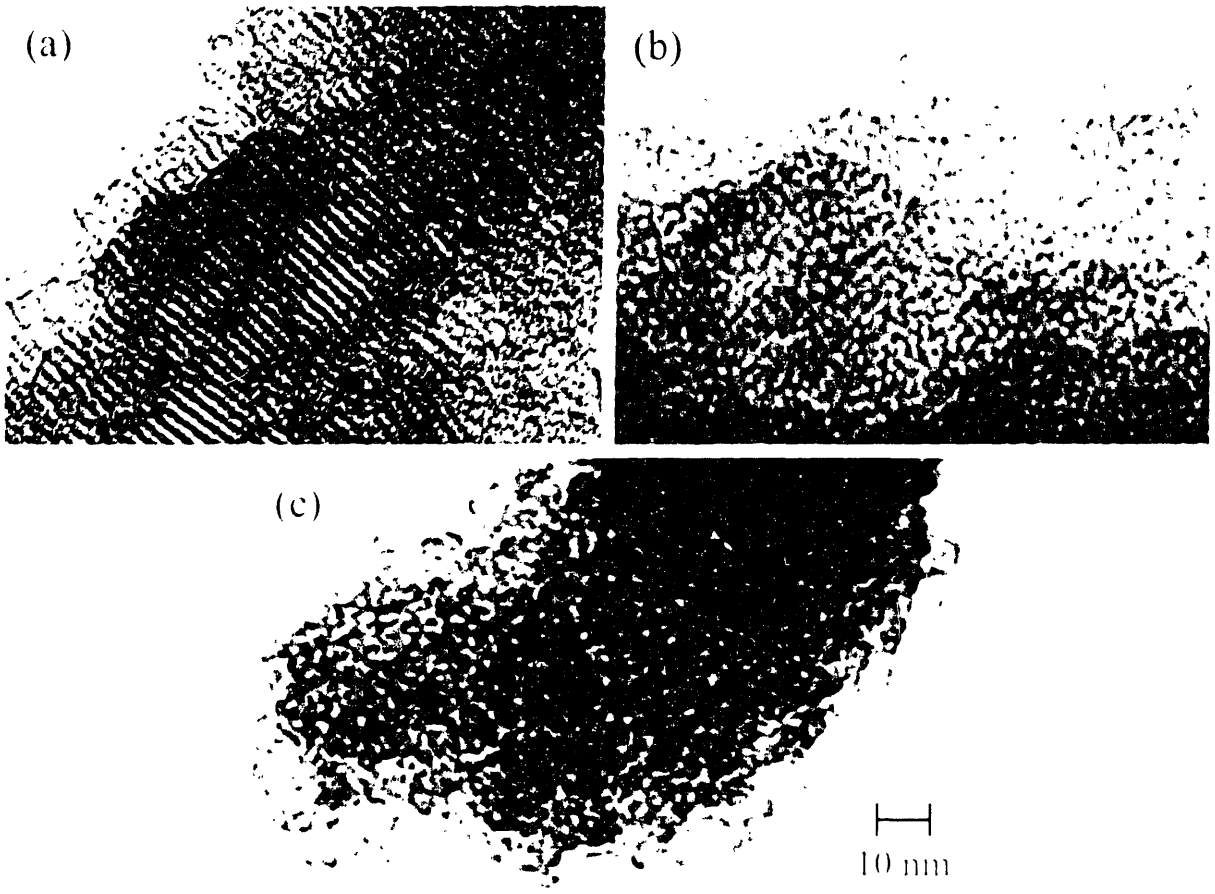

Figure 2.3. TEM images of (a,b) as-synthesized and (c) 400 °C-calcined Zr-TMS prepared with $C_{12}H_{25}PO_4^{2-}$. All three micrograph images have the same magnification.

No distinct mesostructure phase dependence on surfactant-to-metal ratio was found in the zirconia system with dodecylphosphate surfactants, however. Figure 2.4 shows the XRD patterns of materials prepared with increasing surfactant:zirconium molar ratios of 0.17:1 to 2:1. At ratios ≤ 0.5:1, the low-angle diffraction peaks were not found in the XRD patterns. The characteristic d_{100} peak appeared at a ratio of 0.75:1, and the higher-order peaks became more noticeable at ratios ≥ 1:1. The d_{100} values were calculated to be *ca.* 31 Å and did not shift appreciably (< 1 Å) with changing surfactant:metal ratios in the range of 0.75:1 to 2:1. Transitions between mesostructured phases, or "mesophases," might depend strongly on the framework's ability to restructure [3]. Recently, it was shown that MCM-48 can be prepared by aging freshly precipitated MCM-41 at 150 °C for several hours [31]. Ethanol evolved from the hydrolysis of the tetraethylorthosilicate precursor was found necessary for the

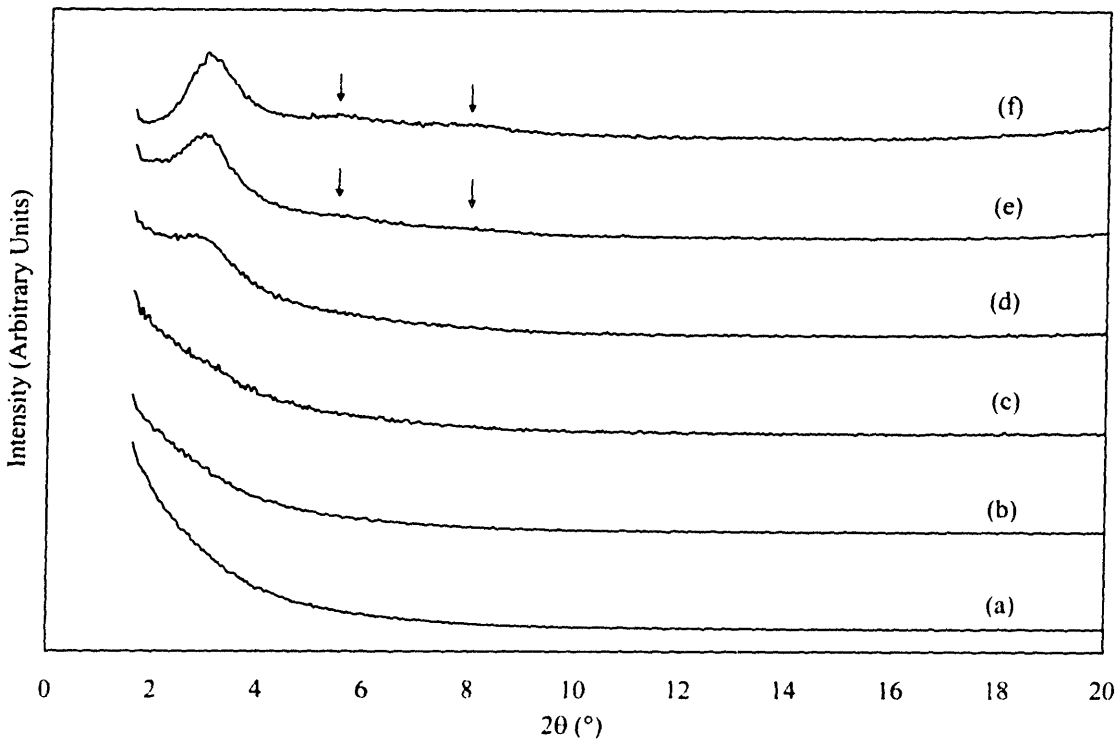

Figure 2.4. XRD patterns of Zr-TMS prepared with $C_{12}H_{25}PO_4^{2-}$:Zr n-propoxide molar ratios of (a) 0.17:1, (b) 0.25:1, (c) 0.50:1, (d) 0.75:1, (e) 1:1, and (f) 2:1. Arrows indicate higher order peaks.

transformation of MCM-41 to MCM-48. In the case of Zr-TMS, n-propanol was present as the solvent for the zirconium n-propoxide and as the hydrolysis product of zirconium n-propoxide, but no similar phase transition was observed. This lack of mesophase transformation in Zr-TMS could be due to the existence of multiple bonds between the phosphate head group and the zirconium atom, locking in a preferred mesostructure.

Control of *d*-spacings was achieved through the use of different alkylphosphate chain lengths. The shifting of the main (100) peak towards lower 2θ angles with increasing tail group length could be observed in the XRD patterns of the as-synthesized Zr-TMS materials (Figure 2.5). Since only the surfactants (which have chain lengths of $n \geq 8$) have typically been used in supramolecular templating, it was interesting to note that an amphiphile as short as 4 carbons could be successfully used as a supramolecular templating agent, as evidenced by the XRD pattern of Zr-TMS prepared with $C_4H_9PO_4^{2-}$ (Figure 2.5(a) and Table 2.1). The covalent-bond approach used here and by Sun and Ying [32] enabled the use of very short organic amphiphilic molecules as supramolecular templating agents. In contrast, through the

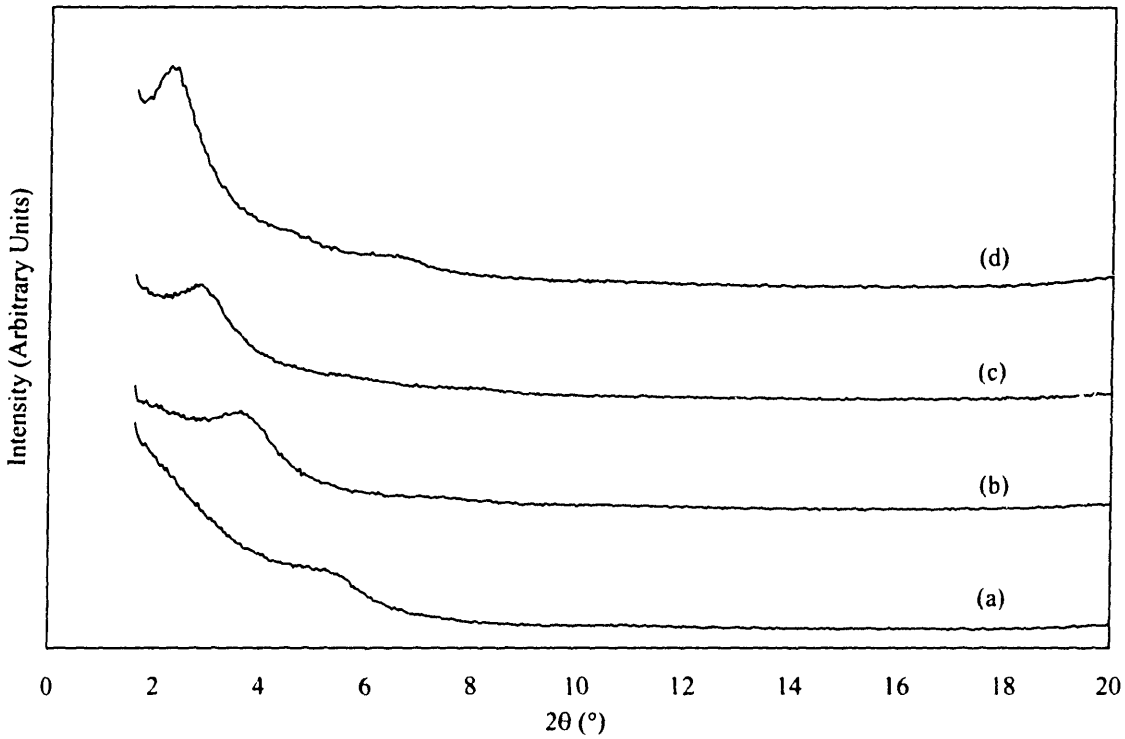

Figure 2.5. XRD patterns of Zr-TMS prepared with $C_nH_{2n+1}PO_4^{2-}$, with carbon number (n) of (a) 4, (b) 8, (c) 12, and (d) 16.

electrostatic approach, the shortest molecule that led to mesostructure formation contained 8 carbons in its hydrocarbon tail [33]. To show that the tail group of the alkylphosphate was necessary for mesostructure formation to occur, orthophosphoric acid (which can be considered an "amphiphile with n = 0") was used in place of alkylphosphates; the resulting material was X-ray amorphous. The addition of solvents for pore swelling had little effect on the d-spacings of the mesostructures, another effect of the presence of alcohol in the reaction medium.

Calcination of the series of Zr-TMS materials led to highly porous, X-ray amorphous materials with BET surface areas exceeding 200 m^2/g; the values are listed in Table 2.2 along with d_{100}-spacings (of the pre-calcined mesostructures), pore volumes and average pore sizes. The calcined samples prepared with $C_{12}H_{25}PO_4^{2-}$ and $C_{16}H_{33}PO_4^{2-}$ were mesoporous and gave nitrogen adsorption-desorption isotherms (Figures 2.6(c) and (d)) that are Type IV with an H2 hysteresis loop; the shape of the isotherms suggested an ink bottle-type pore structure, rather than a cylindrical pore morphology like that of MCM-41. The Type I isotherms of Zr-TMS

prepared with $C_4H_9PO_4^{2-}$ and $C_8H_{17}PO_4^{2-}$ indicated microporosity (Figures 2.6(a) and (b)). The average pore sizes were estimated from the electron micrographs of the materials. The pore size distributions of Zr-TMS materials are broader than that of MCM-41, but the effect of supramolecular templating is clearly manifested in the systematic variation of average pore size, pore volume and surface area with respect to amphiphile chain length. Removal of the amphiphilic templates was not successful through chemical extraction, indicating that the amphiphile-zirconium interaction is stronger than those typified in hydrogen-bonding and electrostatic interactions.

Table 2.2. Physical properties of Zr-TMS prepared with alkylphosphates of different chain lengths.

n	d_{100} (Å)[a]	Surface Area (m^2/g)	Avg. Pore Size (Å)	Pore Volume (cm^3/g)
4	16.6	233	~15	0.208
8	24.2	313	~19	0.227
12	31.0	356	25	0.268
16	38.4	361	26	0.326

[a]As-synthesized samples

Transmission electron microscopy confirmed that the calcined materials were highly porous. Figure 2.3(c) showed that calcined Zr-TMS prepared with $C_{12}H_{25}PO_4^{2}$ possessed pore sizes ranging from *ca.* 21 Å to *ca.* 32 Å in diameter. On the whole, the pores seemed to be packed together with no visible long-range order, consistent with the absence of low-angle XRD peaks. Zr-TMS was unusual for a surfactant-mediated mesoporous material because it did not exhibit the typical diffraction peaks after surfactant removal and yet it contained very high surface areas and mesoporosity. Its sponge-like pore morphology was reminiscent of zirconia aerogels [11] but its average pore size was substantially smaller, reflecting the micellar dimensions of the amphiphilic templates used in its preparation. As-synthesized Zr-TMS mesostructures contained a mixture of layered and disordered regions and, after calcination, only disordered, porous regions were noted.

Calcination temperature and purge atmosphere have an important effect on the structure of Zr-TMS materials. Calcination of Zr-TMS prepared with $C_{12}H_{25}PO_4^{2-}$ at 400 °C under air yielded a light beige material with a surface area of *ca.* 300 m^2/g, but calcination under nitrogen gave a black material of greater than 400 m^2/g. The carbonaceous deposit in the latter amounted to *ca.* 0.4 wt% and could be removed at 400 °C under air for another 3 hr

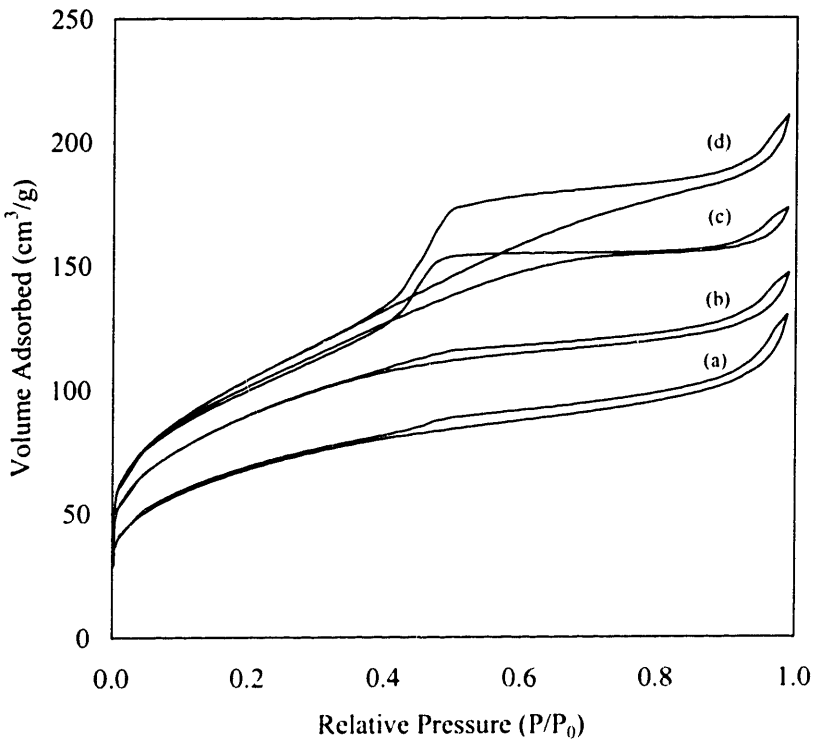

Figure 2.6. Nitrogen adsorption-desorption isotherms of calcined Zr-TMS prepared with $C_nH_{2n+1}PO_4^{2-}$, with carbon number (n) of (a) 4, (b) 8, (c) 12, and (d) 16.

to give a material with a surface area of 356 m^2/g. Careful calcination at 400 °C under vacuum led to even higher surface areas (560 m^2/g) as reported earlier [20]. Higher calcination temperatures led to reduced surface areas; for example, the BET surface area was found to decrease to 300 m^2/g after calcination at 500 °C under N_2. The surface areas obtained after calcination at 600 °C and 800 °C under air were 103 m^2/g and 24 m^2/g, respectively. Zr-TMS remained amorphous after calcination at temperatures below 600 °C. Diffraction peaks corresponding to the tetragonal phase of zirconium oxide were noted at 600 °C; typical temperatures for zirconia crystallization to the tetragonal phase are between 400 °C and 500 °C.

Figure 2.7 showed PA-FTIR spectra of the as-synthesized and calcined Zr-TMS prepared with $C_{12}H_{25}PO_4^{2-}$, which were representative of Zr-TMS produced with alkylphosphates. The hydrocarbon deformation and stretching modes (~1400-1500 cm^{-1}, ~2800-3000 cm^{-1}) could be seen in Figure 2.7(a); these bands disappeared after calcination (Figure 2.7(b)), indicating the loss of the hydrocarbon tail group of the alkylphosphate. The

intense band at *ca.* 1075 cm^{-1}, assigned to phosphate stretching [34], was present in both PA-FTIR spectra (with a minor peak shift to 1050 cm^{-1} after calcination), indicating the retention of phosphate anions in the calcined material. The phosphate head groups were presumed to cover the inner surfaces of the zirconium oxide framework, which would be favorable in terms of enhanced acid strength and catalytic activity for hydrocarbon conversion [13,28b]. The broadening of the phosphate band after calcination also suggested that the chemical environment of the phosphates was different upon calcination. Relative to the phosphate band, the increased intensity of the features below 800 cm^{-1} upon calcination might be a result of further condensation of the zirconium oxide framework. The peak at *ca.* 1620 cm^{-1} (deformation mode of water) in both spectra indicated the presence of surface adsorbed water, contributing to the broad O-H stretching band above 3100 cm^{-1}.

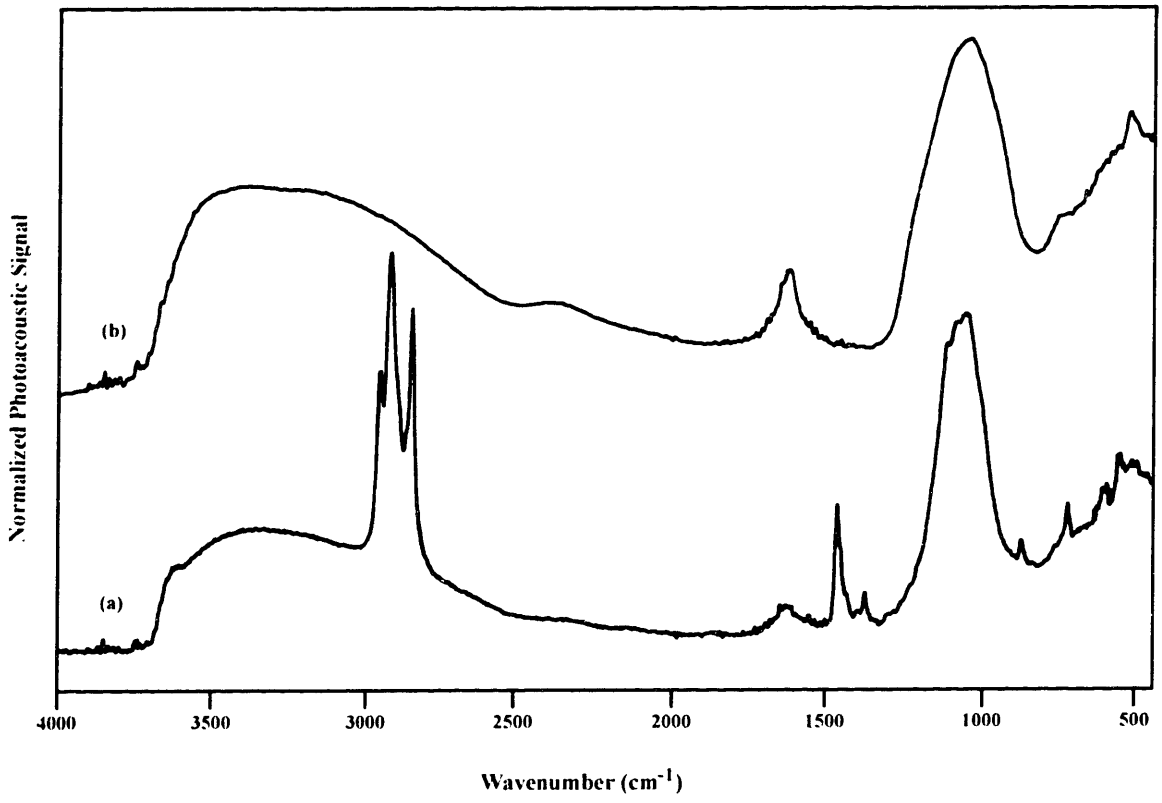

Figure 2.7. PA-FTIR spectra of (a) as-synthesized and (b) calcined Zr-TMS prepared with $C_{12}H_{25}PO_4^{2-}$. The latter was calcined at 400 °C under nitrogen for 3 hr and then under air for 3 hr.

A thermogravimetric profile (under air) for Zr-TMS prepared with $C_{12}H_{25}PO_4^{2-}$ was shown in Figure 2.8. The 2.8% weight loss below 100 °C could be associated with the removal of physisorbed water. A second weight loss of 40.7% occurred between 100 °C and 400 °C, resulting possibly from the combustion of the hydrocarbon tail group of the amphiphilic templating agent. Another 4.6 wt% was lost by 500 °C, which could be attributed to the loss of chemically bound water as the phosphated zirconia framework underwent further condensation and sintering. A total loss of *ca.* 48 wt% was reached by 500 °C. Based on the assumption that only the tail group of the alkylphosphate was removed during calcination between 100 °C and 400 °C, a surfactant:zirconium molar ratio of *ca.* 1.2:1 was calculated. This ratio was close to the 1.3:1 value derived from elemental analysis of calcined Zr-TMS (32.1 wt% Zr and 13.7 wt% P), and was slightly in excess of the 1:1 ratio used in the synthesis mixture. Similar values from elemental analysis were obtained for Zr-TMS materials synthesized with other alkylphosphates.

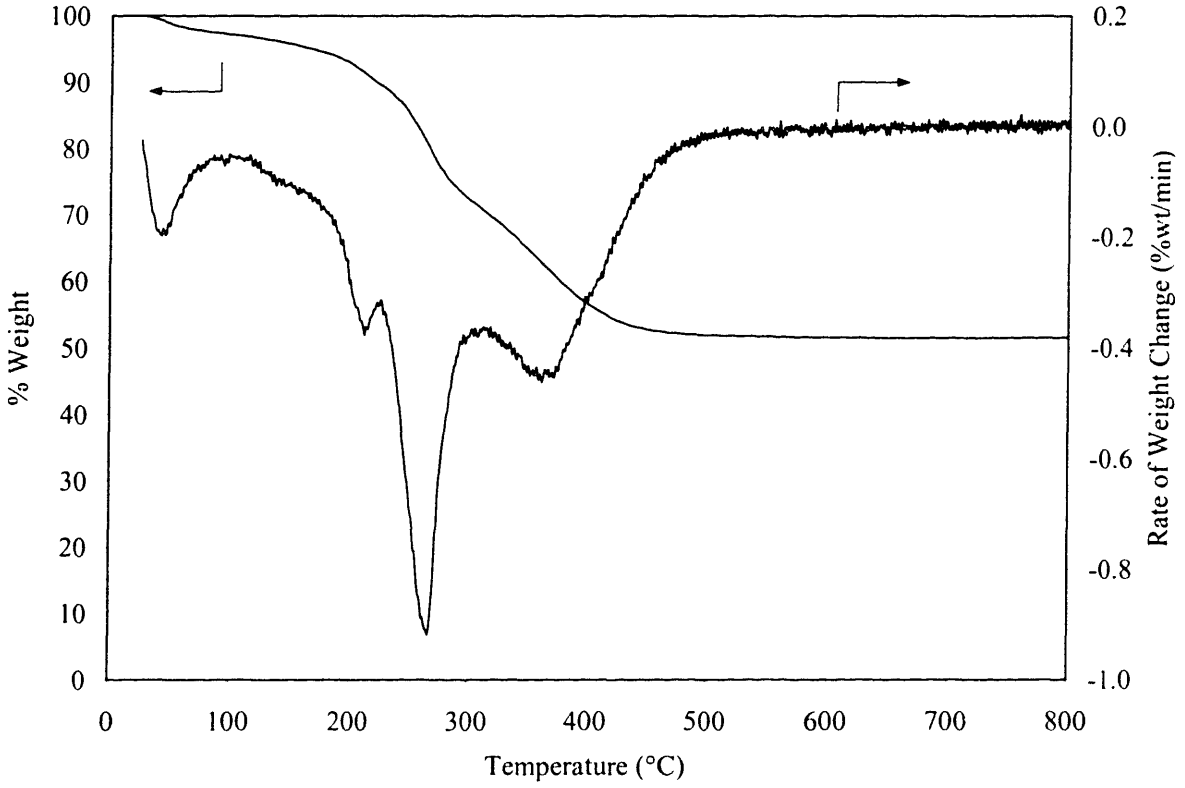

Figure 2.8. TGA profile and rate of weight change of Zr-TMS prepared with $C_{12}H_{25}PO_4^{2-}$ taken under air.

2.3.2 Carboxylate Head Group

The carboxylate head group has two oxygen atoms that can react with the zirconium alkoxide. Not only can the carboxylate functionality form a single bond with the metal, but it can chelate to or bridge between multiple zirconium alkoxide molecules à la unidentate and bidentate ligands, respectively [35], which would be advantageous for mesostructure formation.

Carboxylate amphiphiles of varying tail group lengths were combined with zirconium n-propoxide to prepare mesostructured zirconium oxide. The effect of chain length on mesostructure formation was readily noted in the XRD patterns of the Zr-TMS materials synthesized with $C_nH_{2n+1}COO^-$ (Figure 2.9).

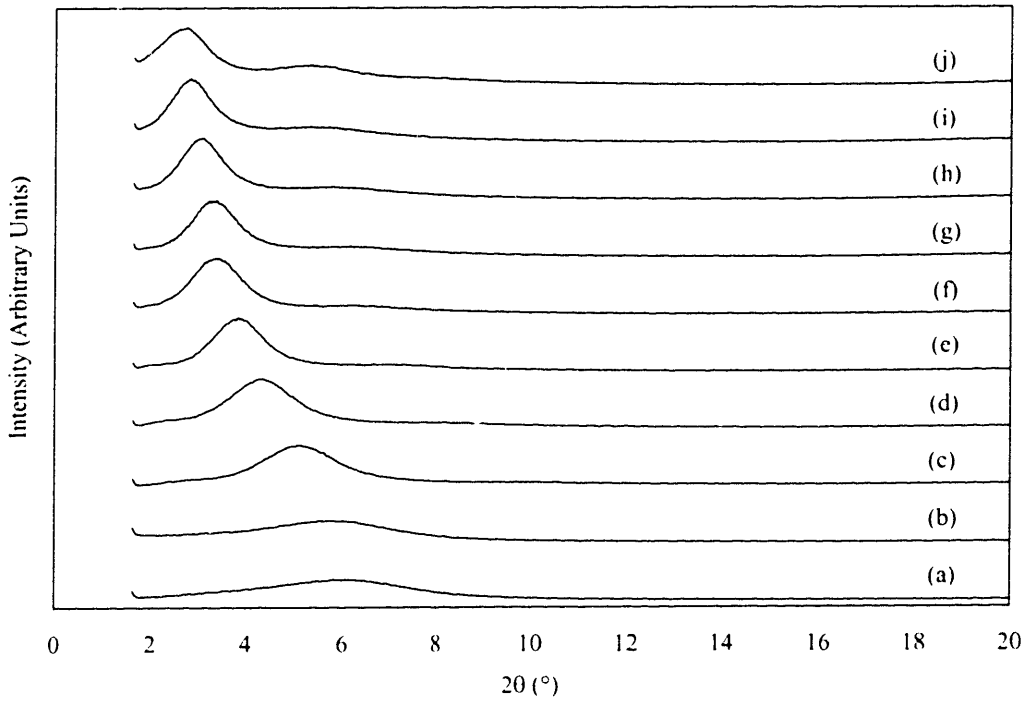

Figure 2.9. XRD patterns of Zr-TMS prepared with $C_nH_{2n+1}COO^-$, with carbon number (n) of (a) 1, (b) 2, (c) 4, (d) 6, (e) 8, (f) 10, (g) 12, (h) 14, (i) 16, and (j) 18.

A systematic shift in the main diffraction peak towards lower 2θ angles was observed, indicating an increase in the d_{100}-spacing with increasing length of the amphiphile tail group (Table 2.1). Secondary diffraction peaks could be seen more distinctly in the materials prepared with longer-chain amphiphiles. The *d*-spacings of these peaks suggested that these

materials might be lamellar in mesostructure, but TEM work only illustrated the presence of large regions of highly-packed amphiphile-occluded pores. Carboxylate amphiphiles shorter than 8 carbons were not considered as surfactants, but they were found to template mesostructured materials with a distinct (100) peak (Figures 2.9(a)-(d)), as in the case of short-chain phosphate amphiphiles. The formation of mesostructures with amphiphiles of less than 8 carbons suggests that the head group-inorganic interaction is strong enough to overcome the thermodynamically unfavored micellization of the short-chained amphiphiles. Recovery of an open, mesoporous zirconium oxide framework through carboxylate template removal by calcination or by chemical extraction proved unsuccessful. The materials calcined at 400 °C under air were X-ray amorphous and non-porous, with surface areas less than 30 m^2/g.

2.3.3 Sulfate and Sulfonate Head Groups

Mesostructured zirconium oxide was also prepared from sulfate and sulfonate amphiphiles. Unlike the cases with alkylphosphates and alkylcarboxylates, the direct combination of the sulfur-containing amphiphile and zirconium n-propoxide did not lead to Zr-TMS mesostructures. The head groups may be too strongly associated with the sodium counterions to interact properly with zirconium n-propoxide when dissolved in alcoholic solution.

In a different approach, the amphiphilic compounds were added to an aqueous solution of zirconium acetylacetonate (tris)n-propoxide via the modified sol-gel method. The resulting Zr-TMS mesostructures (Table 2.1) have lamellar diffraction patterns (Figures 2.1(c) and (d)) and collapsed upon calcination.

2.3.4 Non-Ionic Amphiphiles: Amine Head Group

Attempts to prepare mesostructured zirconium oxide with the amine amphiphiles were not successful. Both direct-addition and modified sol-gel routes led to materials that appeared X-ray amorphous. The interaction between alkylamines and zirconium n-propoxide seemed to be non-existent within the context of the covalent-bond approach. However, investigation with other types of zirconium alkoxide precursors led to the conclusion that mesostructured zirconium oxide was possible with amine surfactants in the absence of free alcohol.

Dodecylamine was warmed until its melting point was reached (28 °C) and zirconium isopropoxide, a solid, was dissolved in it. The resulting solution was heated to 80 °C for 5 minutes while stirring and then cooled to room temperature before water was added. Aging the mixture at 80 °C for 4 days gave a material with the XRD pattern shown in Figure 2.1(e). With a small broad peak centered around $2\theta = 2.6°$ (d_{100} = 34.5 Å, Table 2.1), this material had a mesostructure that was less well-defined than the Zr-TMS materials prepared with anionic amphiphiles. Zirconium ethoxide led to a similar mesostructure as the former, with d_{100} = 34.6 Å; no steric effect associated with the alkoxy ligands was observed. The main difference among the three zirconium alkoxides was the large amount of n-propanol present in the zirconium n-propoxide precursor. Free alcohol might compete with alkylamines for the coordination sites on the zirconium center and prevent amine ligation if in excess.

2.3.5 Proposed Method of Mesostructure Formation

As the interaction between the metal precursor and the amphiphile head group is critical towards mesostructure formation, we devised the covalent-bond approach to exploit the strong interaction between the anionic amphiphiles and zirconium n-propoxide. Evidence of covalent bonding can be found by examining dodecylphosphate in the synthesis of Zr-TMS. The changes in the chemical environment of the phosphorus in the phosphate head group were followed conveniently via ^{31}P MAS NMR (Figure 2.10).

The dihydrogen phosphate surfactant exhibited a slight chemical shift of -0.06 ppm (from phosphoric acid), indicating that the tail group had a negligible effect on the phosphate bonding environment (Figure 2.10(a)); the alkylphosphate head group -O(O)P(OH)$_2$ was very similar to phosphoric acid H-O(O)P(OH)$_2$. The phosphate surfactant in the as-synthesized Zr-TMS mesostructure displayed a dramatically different NMR spectrum (Figure 2.10(b)). All the surfactant molecules in Zr-TMS interacted through the head group in some manner, as the original peak at -0.06 ppm disappeared and several new peaks emerged in the NMR spectrum. Compared with literature values for phosphorus chemical shifts of crystalline metal(IV) phosphate materials [36,37], the new peaks might be attributed to two different types of covalent bonding environments with which the phosphate was involved (Table 2.3).

Roughly half of the phosphate head groups were bound through 3 oxygens (2 hydroxo and 1 oxo; -20.8 ppm), and the other half were bound through 2 oxygens (1 hydroxo and 1

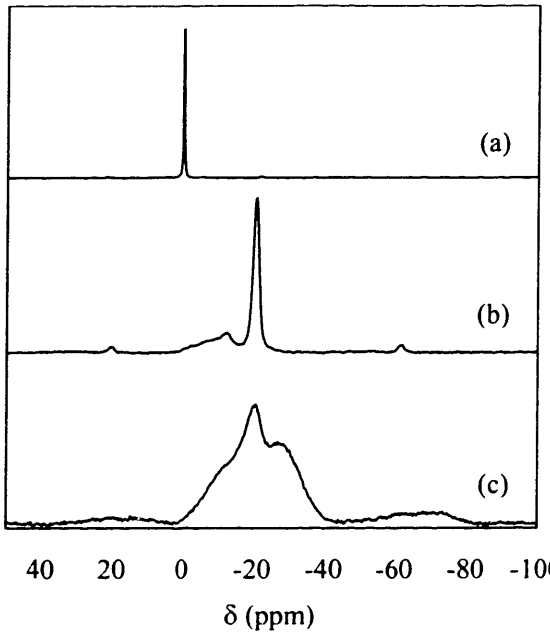

Figure 2.10. ^{31}P MAS NMR spectra of (a) unreacted $C_{12}H_{25}PO_4^{2-}$ surfactant; and (b) as-synthesized and (c) 400 °C-calcined Zr-TMS prepared with $C_{12}H_{25}PO_4^{2-}$.

oxo; -12.4 and -13.3 ppm), as estimated from the deconvoluted peak areas. The broad peak width around -12.4 ppm suggested a wide distribution of alkylphosphate bonding environments involving bonding through 2 oxygens. The phosphate head group appeared to have bridged across zirconium cations (through 2 or 3 oxygens), similar to the case of α-zirconium phosphate [28b]. This study showed that the phosphate amphiphile (and the other anionic amphiphiles) could be envisioned as a covalently-bound ligand to zirconium n-propoxide in the mesostructure (Figure 2.11(a)).

Table 2.3. ^{31}P NMR peak shifts (ppm) of pre-calcined and mesoporous Zr-TMS materials.

	X = H	Alkylphosphate (X = $C_{12}H_{23}$)	Pre-calcined Zr-TMS	Mesoporous Zr-TMS
XH_2PO_4	0	-0.06	–	–
$XHPO_4$	-10.6 [36]	–	{ -12.4 (broad) -13.3 }	-12.4
XPO_4	-19.3 [38]	–	-20.8	-20.4
PO_4	-32.5 [36]	–	–	-28.6

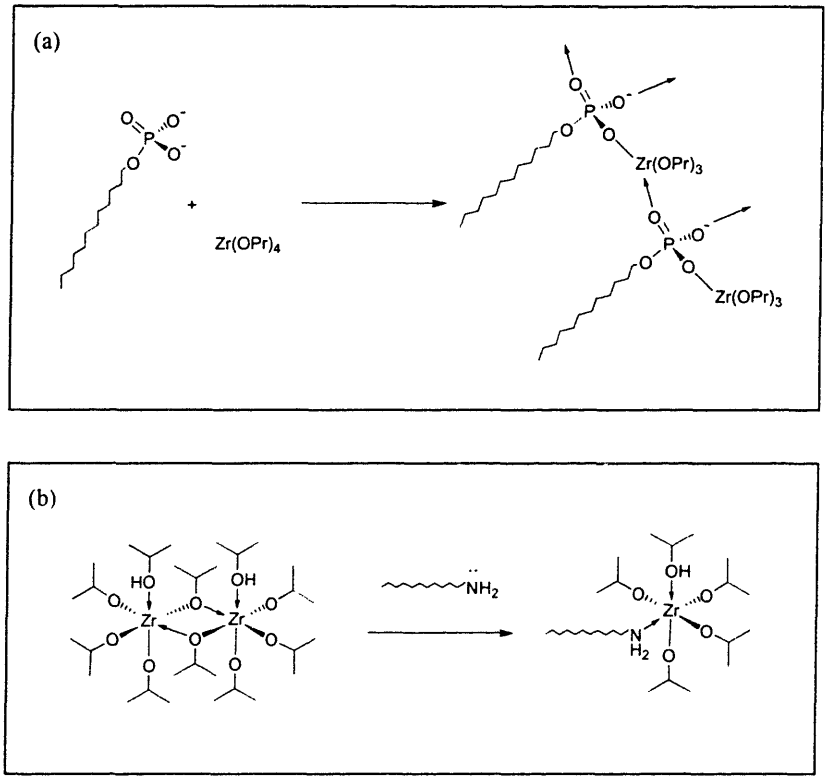

Figure 2.11. Representative schematic drawings of (a) the anionic amphiphile-zirconium n-propoxide interaction, and (b) the non-ionic amphiphile-zirconium isopropoxide interaction. The phosphate head group in (a) could be substituted by carboxylate (less 1 oxygen), sulfate and sulfonate head groups. Zirconium isopropoxide is shown in dimeric form in (b).

The method of formation via covalent bonding interactions could be generalized as a schematic in Figure 2.12 for an anionic amphiphile and zirconium n-propoxide. The addition of amphiphile to the zirconium precursor produces oligomers (which might or might not be soluble in n-propanol) but, because there is no water in the system to drive the micellization process, the oligomers do not self-assemble. Once water is added, hydrolysis and self-assembly processes occur. The supramolecular aggregates could be of more than one form, such as cylindrical rods and layers; these aggregates combine via condensation at the inorganic-surfactant interface. Aging at an elevated temperature promotes further hydrolysis and condensation of the inorganic framework. If the amphiphile contains the phosphate head group, then calcination of the resultant Zr-TMS yields mesoporous (or microporous) phosphated zirconia.

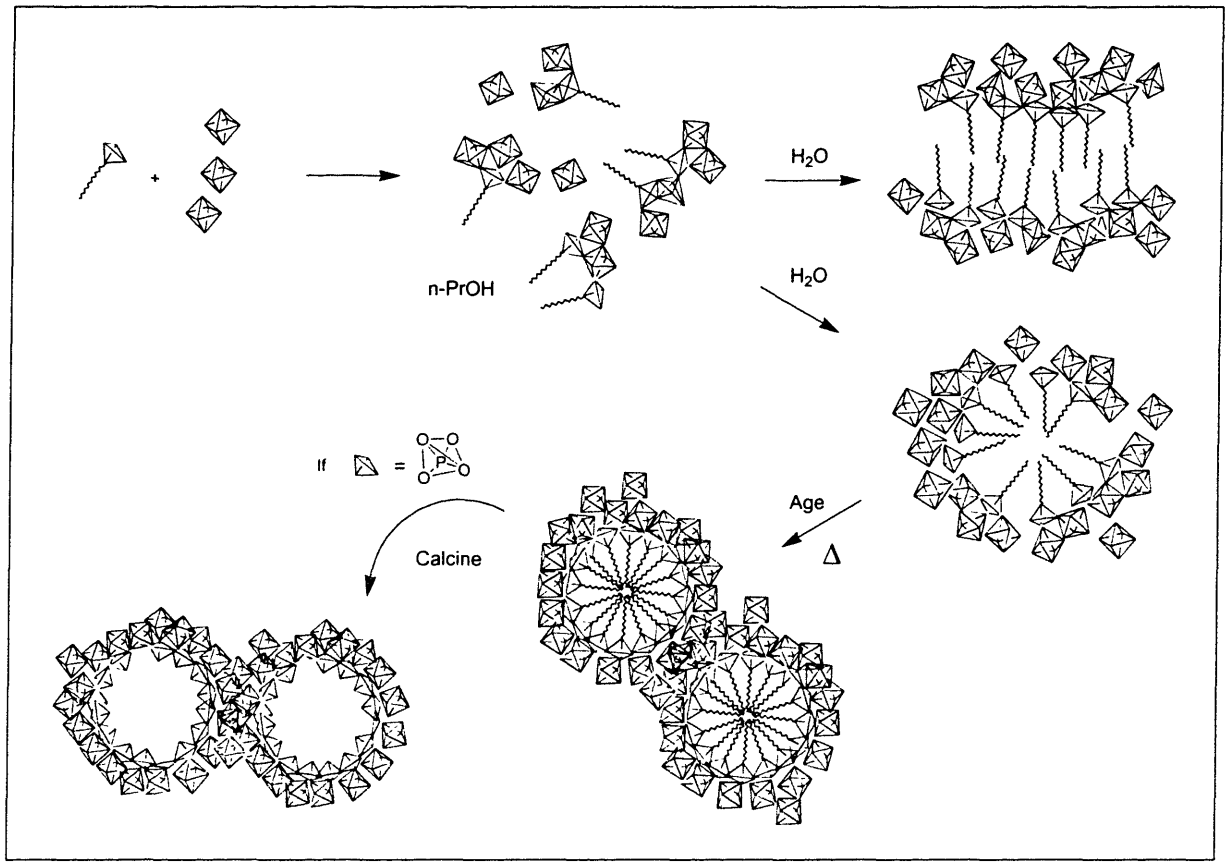

Figure 2.12. Proposed scheme for Zr-TMS formation with anionic amphiphiles and zirconium n-propoxide. The illustrated shapes for the zirconium n-propoxide and amphiphile were not drawn to scale.

Non-ionic amine surfactants were known to serve as templates for a number of mesoporous materials. Unlike the formation of silicate HMS materials with amine surfactants, which relied on hydrogen-bonding interactions [5a,c], the formation of mesoporous niobium oxide and tantalum oxide TMS1 materials was based upon a strong covalent interaction between the amine surfactant head group and the metal alkoxide precursor [7,8]. The "ligand-assisted templating" (LAT) route first developed for the Nb-TMS1 and Ta-TMS1 materials, which was used as the preparative approach for the case involving the direct addition of amines in this study, was found to give zirconia mesostructures only when the amount of alcohol in the synthesis mixture was minimized (Figure 2.11(b)); excess alcohol was found to disrupt mesostructure formation. This contrasted the preparation of silicate HMS, which required the addition of excess ethanol to the synthesis mixture of alkylamine, tetraethoxysilane, and water [5a,c].

2.3.6 Stability of Zr-TMS Mesostructures

The removal of the organic templates from mesostructured zirconia did not necessarily lead to mesoporous materials. Only Zr-TMS materials prepared with alkylphosphates produced highly porous materials upon calcination. The retention of the phosphate head groups as "molecular braces" fixed along the pore walls appeared to be necessary for the stability of an open porous zirconia framework, as in other surfactant-templated phosphated zirconia [18,19]. Mesostructures prepared with other head groups would collapse during amphiphile removal, leading to essentially non-porous materials.

The state of the phosphate head groups in Zr-TMS was very different after calcination (Figure 2.10(c), Table 2.3). The amount of phosphates that remained in the 2- and 3-oxygen phosphate bonding environments (-12.4 ppm and -20.4 ppm, respectively) dropped from 50%:50% to 40%:20%, and the remaining 40% appeared in a 4-oxygen phosphate bonding environment (-28.6 ppm). With the loss of the tail group, the phosphate head group would be able to accommodate another bond to zirconium. The -28.6 ppm peak might represent phosphates within the collapsed layered regions after calcination, suggesting that ~40% of the Zr-TMS material was layered and unstable to surfactant removal. The broadening of the NMR peaks indicated that the phosphate bonding environments became more anisotropic after calcination, *i.e.* there was greater variance in the bonding angles of the phosphate anions, consistent with the broadening of the phosphate PA-FTIR band (Figure 2.7(b)). The formation of bonds between phosphate head groups was unlikely due to the absence of NMR peaks at ≤-32 ppm [38].

2.3.7 Catalytic Activity of Zr-TMS

The isomerization of 1-butene is a very useful probe reaction for acid catalysts. The product distributions can be used to ascertain the strength of catalyst acidity [39,40]. The double-bond isomerization of 1-butene leads to cis- and trans-2-butenes, indicating the presence of acid sites with moderate strength. It can also be catalyzed by basic materials and metals [41]. The skeletal isomerization of 1-butene to isobutene indicates strong acidity [42]. This particular reaction is of industrial significance as isobutene is a valuable reactant to methyl tert-butyl ether (MTBE) and to a number of polymers [40].

Zr-TMS (synthesized with dodecylphosphate) was found active for the isomerization of 1-butene to 2-butenes (Figure 2.13). No other products were detected. Complete conversion of 1-butene was not possible because of the thermodynamic equilibrium established with the isomer products. The equilibrium conversion amounts of the three isomers were calculated from their standard free energies of formation [43]. These calculated values were plotted as a function of temperature, shown as dotted curves in Figure 2.13. The measured isomer amounts over Zr-TMS approached equilibrium values at temperatures of 250 °C and 350 °C, but not at 150 °C. The isomerization of 1-butene was kinetically limited at the reaction temperature of 150 °C.

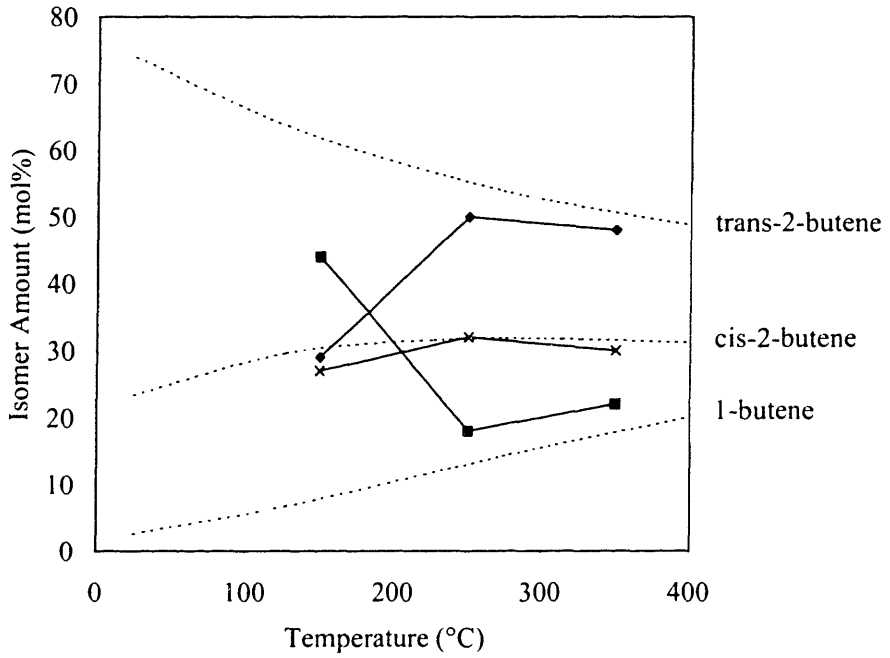

Figure 2.13. 1-butene double-bond isomerization results for Zr-TMS calcined at 400 °C. Legend: 1-butene (■), cis-2-butene (×), and trans-2-butene (◆).

2.4 Summary

We have developed the supramolecular templating chemistry for mesoporous zirconia by examining various synthesis parameters, the effect of different surfactants, and the mechanism of formation. Mesostructured zirconia Zr-TMS could be prepared by reacting anionic or non-ionic amphiphiles with the zirconium alkoxide prior to the addition of water. Phosphate, carboxylate, sulfate, and sulfonate head groups have reactive oxygen atoms that

strongly interact with the transition metal, forming the basis for the covalent-bond approach. The critical issue of strength of the amphiphile-inorganic covalent interaction was illustrated by the templating capability of amphiphilic molecules with shorter chain lengths than those typical of surfactant molecules. The systematic variation in XRD peak position to changes in amphiphile chain length reflected the supramolecular nature of the templating mechanism and its applicability to amphiphiles regardless of chain length. Microporous phosphated zirconia materials were obtained with very short phosphate amphiphiles. The covalency of the anionic amphiphile-zirconium interaction was further demonstrated and a method of mesostructure formation was proposed, based on ^{31}P MAS NMR studies of Zr-TMS prepared with dodecylphosphate. The moderate acidity of mesoporous phosphated zirconia was demonstrated for 1-butene double-bond isomerization.

2.5 References

[1] Kresge, C. T.; Leonowicz, M. E.; Roth, W. J.; Vartuli, J. C.; Beck, J. S. *Nature* **1992**, *359*, 710.

[2] Beck, J. S.; Vartuli, J. C.; Roth, W. J.; Leonowicz, M. E.; Kresge, C. T.; Schmitt, K. D.; Chu, C. T.-W.; Olsen, D. H.; Sheppard, E. W.; McCullen, S. B.; Higgins, J. B.; Schlenker, J. L. *J. Am. Chem. Soc.* **1992**, *114*, 10834.

[3] Huo, Q.; Margolese, D. I.; Ciesla, U.; Demuth, D. G.; Feng, P.; Gier, T. E.; Sieger, P.; Firouzi, A.; Chmelka, B. F.; Schüth, F.; Stucky, G. D. *Chem. Mater.* **1994**, *6*, 1176.

[4] Huo, Q.; Margolese, D. I.; Ciesla, U.; Feng, P.; Gier, T. E.; Sieger, P.; Leon, R.; Petroff, P. M.; Schüth, F.; Stucky, G. D. *Nature* **1994**, *368*, 317.

[5] (a) Tanev, P. T.; Pinnavaia, T. J. *Science* **1995**, *267*, 865. (b) Bagshaw, S. A.; Prouzet, E.; Pinnavaia, T. J. *Science* **1995**, *269*, 1242. (c) Tanev, P. T.; Pinnavaia, T. J. *Chem. Mater.* **1996**, *8*, 2068.

[6] Antonelli, D. M.; Ying, J. Y. *Angew. Chem. Int. Ed. Engl.* **1995**, *34*, 2014.

[7] (a) Antonelli, D. M.; Ying, J. Y. *Angew. Chem. Int. Ed. Engl.* **1996**, *35*, 426. (b) Antonelli, D. M.; Nakahira, A.; Ying, J. Y. *Inorg. Chem.* **1996**, *35*, 3126.

[8] Antonelli, D. M.; Ying, J. Y. *Chem. Mater.* **1996**, *8*, 874.

[9] For example, (a) Weidenhof, V.; Gropper, F.; Müller, U.; Marosi, L.; Cox, G.; Houbertz, R; Hartmann, U. *J. Mater. Res.* **1997**, *12*, 1634. (b) Huang, Y.; Sachtler, W.

M. H. *Chem. Commun.* **1997**, 1181. (c) Kim, A.; Bruinsma, P.; Chen, Y.; Wang, L.-Q.; Liu, J. *Chem. Commun.* **1997**, 161.

[10] For example, (a) Hudson, M. J.; Knowles, J. A. *J. Mater. Chem.* **1996**, *6*, 89. (b) Pacheco, G.; Zhao, E.; Garcia, A.; Sklyarov, A.; Fripiat, J. J. *Chem. Commun.* **1997**, 491.

[11] Ward, D. A.; Ko, E. I. *Chem. Mater.* **1993**, *5*, 956.

[12] Subbarao, E. C. In *Science and Technology of Zirconia*; Subbarao, E. C., Ed.; American Ceramic Society: Columbus, OH, 1981; p. 1.

[13] Boyse, R. A.; Ko, E. I. *Catal. Lett.* **1996**, *38*, 225.

[14] (a) Jin, T.; Yamaguchi, T.; Tanabe, K. *J. Phys. Chem.* **1986**, *90*, 4794. (b) Davis, B. H.; Keogh, R. A.; Srinivasan, R. *Catal. Today* **1994**, *20*, 219. (c) Song, X.; Sayari, A. *Catal. Rev.-Sci. Eng.* **1996**, *38*, 329.

[15] Yamaguchi, T. *Catal. Today* **1994**, *20*, 199.

[16] Nakano, Y.; Iizuka, T.; Hattori, H.; Tanabe, K. *J. Catal.* **1979**, *57*, 1.

[17] Tanabe, K.; Yamaguchi, T. *Catal. Today* **1994**, *20*, 185.

[18] Ciesla, U.; Schacht, S.; Stucky, G. D.; Unger, K. K.; Schüth, F. *Angew. Chem. Int. Ed. Engl.* **1996**, *35*, 541.

[19] Liu, P.; Reddy, J. S.; Adnot, A.; Sayari, A. *Mater. Res. Soc. Symp. Proc.* **1996**, *431*, 101.

[20] Wong, M. S.; Antonelli, D. M.; Ying, J. Y. *Nanostr. Mater.* **1997**, *9*, 165.

[21] Wong, M. S.; Ying, J. Y. *Chem. Mater.* **1998**, *10*, 2067.

[22] Moroi, Y. *Micelles: Theoretical and Applied Aspects*; Plenum Press: New York, 1992.

[23] Nelson, A. K.; Toy, A. D. F. *Inorg. Chem.* **1963**, *21*, 775.

[24] Debsikdar, J. C. *J. Non-Cryst. Solids* **1986**, *86*, 231.

[25] Gregg, S. K.; Sing, K. S. W. *Adsorption, Surface Area and Porosity*, 2nd Ed.; Academic Press: London, 1982.

[26] Barrett, E. P.; Joyner, L. G.; Halenda, P. P. *J. Am. Chem. Soc.* **1951**, *73*, 373.

[27] Livage, J.; Henry, M.; Sanchez, C. *Prog. Solid St. Chem.* **1988**, *18*, 259.

[28] (a) Maya, L. *Inorg. Nucl. Chem. Lett.* **1979**, *15*, 207. (b) Clearfield, A. *Comments Inorg. Chem.* **1990**, *10*, 89.

[29] Ryoo, R.; Kim, J. M.; Ko, C. H.: Shin, C. H. *J. Phys. Chem.* **1996**, *100*, 17718.

[30] Vartuli, J. C.; Schmitt, K. D.; Kresge, C. T.; Roth, W. J.; Leonowicz, M. E.; McCullen, S. B.; Hellring, S. D.; Beck, J. S.; Schlenker, J. L.; Olsen, D. H.; Sheppard, E. W. *Chem. Mater.* **1994**, *6*, 2317.

[31] Gallis, K. W.; Landry, C. C. *Chem. Mater.* **1997**, *9*, 2035.

[32] Sun, T.; Ying, J. Y. *Nature* **1997**, *389*, 704.

[33] Beck, J. S.; Vartuli, J. C.; Kennedy, G. J.; Kresge, C. T.; Roth, W. J.; Schramm, S. E. *Chem. Mater.* **1994**, *6*, 1816.

[34] Busca, G.; Lorenzelli, V.; Galli, P.; La Ginestra, A.; Patrono, P. *J. Chem. Soc., Faraday Trans. 1* **1987**, *83*, 853.

[35] Mehrotra, R. C.; Bohra, R. *Metal Carboxylates*; Academic Press: London, 1983.

[36] Bortun, A. I.; Bortun, L.; Clearfield, A.; Villa-García, M. A.; García, J. R.; Rodríguez, J. *J. Mater. Res.* **1996**, *11*, 2490.

[37] Segawa, K.; Nakajima, Y.; Nakata, S.; Asoaka, S.; Takahashi, H. *J. Catal.* **1986**, *101*, 81.

[38] Mudrakovskii, I. L.; Shmachkova, V. P.; Kotsarenko, N. S.; Mastikhin, V. M. *J. Phys. Chem. Solids* **1986**, *47*, 335.

[39] Aguayo, A. T.; Arandes, J. M.; Olazar, M.; Bilbao, J. *Ind. Eng. Chem. Res.* **1990**, *29*, 1172.

[40] Butler, A. C.; Nicolaides, C. P. *Catal. Today* **1993**, *18*, 443.

[41] Baird, M. J.; Lunsford, J. H. *J. Catal.* **1972**, *26*, 440.

[42] Damon, J.-P.; Delmon, B.; Bonnier, J.-M. *J. Chem. Soc., Faraday Trans. 1* **1977**, *1*, 73.

[43] Hougen, O. A. *Chemical Process Principles*, 2nd Ed.; Wiley and Sons: New York, 1954.

Chapter 3. Mesoporous Zirconia-Silica

3.1 Introduction

While pure mesoporous silica MCM-41 contains unique structural features, it is a catalytically inactive material, like amorphous silica gel. There has been great activity in developing supramolecular-templated mesoporous silicates for heterogeneous catalysis [1-3], and the general method used to achieve this goal has been the chemical modification of the silicate pore walls. Successful examples have been illustrated by the incorporation of a second metal cation into the silicate framework [4,5]; the surface addition of metal films [6], metal cations [7], metal oxo species [8], or metal oxide clusters [9]; and the surface anchoring of organometallic complexes [10].

From a composition standpoint, mixed metal oxides have been investigated for a variety of catalytic reactions because of their enhanced acidity relative to pure metal oxides [11]. Of these materials, those composed of zirconia and silica have been found among the most strongly acidic [12]. The surface acidity comes from the difference in valence or coordination states of adjacent metal cations [11], and is affected by the relative metal amounts [13], the atomic homogeneity of the mixed oxide [14], and the presence of surface anions [15]. These zirconia-silicates tend to be amorphous and have low surface areas. Silicates in the form of zeolites that contain small amounts of framework Zr have generated interest as oxidation catalysts because of the importance of Ti-doped zeolites (e.g. TS-1) for commercial oxidation reactions and the similar chemistry shared by Zr and Ti [16,17]. Zirconia-silicate materials with a well-defined pore structure, controllable pore sizes and high surface areas would be advantageous for acid and oxidation catalysis.

The preparation of MCM-41 silicates doped with a variety of metal cations has been reported by numerous researchers [4,6]. The doping procedure is straightforward, in which the precursor of the desired metal is added to the silicate/surfactant/water/base synthesis mixture. The metal cations are generally thought to be distributed homogeneously throughout the silicate framework, with the total amount of incorporated metal cations low (~2-4 wt%) [3]. Higher loadings are desirable for increased catalytic activity, but are difficult to achieve in doped mesoporous silicates. The highly basic solution (pH $\geq$ 10) required for MCM-41 synthesis appears to limit the incorporation of secondary metal cation dopants. Under such condition, the dopant metal can separate into a second phase because of incompatible

condensation and precipitation rates. Also, high levels of doping can weaken mesostructure, resulting in structural collapse after surfactant removal [6]. Careful manipulation of the templating chemistry involved is thus required.

The preparation of Zr-doped mesoporous silicates at high [18] and neutral [19] pH's has been studied by other researchers, although these materials lost long-range pore ordering with increasing Zr amounts. Nonetheless, such materials were shown to possess acidic [18,20] and oxidative properties [19]. A low-pH route to mesoporous silicates was developed by Stucky and co-workers [21], and the small amount of work done on doped silicates via this approach had found doping levels of 1 wt% [22].

In this Chapter, we investigated the preparation of mesoporous Zr-doped silicates under highly acidic conditions (pH < 0). Understanding of the synthesis chemistry allowed the derivation of mesoporous silicates with as much as ~20 wt% Zr, while maintaining the long-range pore ordering and high surface areas. The effect of Zr doping on mesostructure was examined and the nature of Zr in the framework was elucidated. The catalytic activity of these nanoporous materials was demonstrated for acid-catalyzed and oxidation reactions.

3.2 Experimental Methods

3.2.1 Synthesis

A solution of zirconium sulfate tetrahydrate was prepared by dissolving a desired amount of the salt ($Zr(SO_4)_2 \cdot 4H_2O$, 99.99+%, Strem) in 15 ml of deionized water. This was combined with a solution containing cetyltrimethylammonium bromide (CTAB, 99+%, Alfa Aesar) and hydrochloric acid (37%, Mallinckrodt). Tetraethylorthosilicate (TEOS, 98%, Aldrich) was immediately added to the mixture. The molar ratio of this precursor mixture was 10 TEOS : x $Zr(SO_4)_2$: 1.3 CTAB : y HCl : 1690 H_2O. Samples prepared with y = 54 (at a calculated pH of -0.25) were labeled ZrSi1-x, and samples prepared with y = 5.4 (at a higher pH of 0.75) were labeled ZrSi2-x (Table 3.1). A special sample of ZrSi2-x was prepared also, where x = 0.2. Zirconyl chloride octahydrate ($ZrOCl_2 \cdot 8H_2O$, 98%, Aldrich) was used as an alternative Zr precursor, resulting in a sample labeled ZrSi1-3C. These samples were collectively named ZrSi. The mixture was stirred for 2 hr and then aged at room temperature for two days. The resulting white powder was filtered and washed 3 times with water, and left to air-dry overnight. For surfactant removal, the mesostructured ZrSi samples were

calcined at 540 °C for 3 hr under flowing air, with a ramp rate of ~3 °C/min. A pure mesoporous silicate labeled ZrSi1-0 was prepared without addition of any Zr precursors. The preparation of ZrSi2-0 required an aging time of 2 weeks in order for precipitation to occur.

Table 3.1. Synthesis conditions and elemental analysis results of ZrSi materials.

Sample	Precursor Zr/Si Molar Ratio	Precursor HCl/Si Molar Ratio	Calculated pH[d]	Measured Zr Content (wt%)[e]	Expected Zr Content (wt%)[e]
ZrSi1-0	0.0	5.4	-0.25	0.0	0.0
ZrSi1-1	0.1	5.4	-0.25	2.0	12.6
ZrSi1-3	0.3	5.4	-0.25	2.8	28.2
ZrSi1-10	1.0	5.4	-0.25	4.4	49.8
ZrSi2-0[a]	0.0	0.54	0.75	0.0	0.0
ZrSi2-0.2	0.02	0.54	0.75	3.9[f]	2.9
ZrSi2-1	0.1	0.54	0.75	10.7	12.6
ZrSi2-3	0.3	0.54	0.75	16.2	28.2
ZrSi2-10	1.0	0.54	0.75	19.6	49.8
ZrSi1-3C[b]	0.3	5.4	-0.25	4.5	28.2
ZrSBA-15[b,c]	1.0	5.7	-0.3	4.8	49.8

[a]Non-mesostructured
[b]Zr precursor: $ZrOCl_2 \cdot 8H_2O$
[c]Templating surfactant: P123 triblock copolymer
[d]Based on HCl concentration
[e]Zr content after surfactant removal
[f]Zr content measured via EDS

ZrSi with larger mesopores was prepared by using a much larger surfactant than CTAB [23]. An acidic solution of the surfactant P123 ((ethylene oxide)$_{20}$(propylene oxide)$_{70}$(ethylene oxide)$_{20}$, FW = 5880, BASF) was combined with a 30 wt% solution of zirconyl chloride octahydrate. After TEOS was added to this solution, the synthesis mixture was stirred at room temperature for 1.5 hr and at 35 °C for 1 day. Then the mixture was left to sit at 80 °C for 2 days before product recovery and calcination at 540 °C. The molar ratio of the precursor mixture was 10 TEOS : 10 $ZrOCl_2$: 0.17 P123 : 57 HCl : 1600 H_2O. This sample was termed ZrSBA-15.

3.2.2 Characterization

Powder X-ray diffraction (XRD) data were recorded on a Siemens D5000 diffractometer using nickel-filtered CuK_α radiation with wavelength λ = 1.5406 Å.

Diffraction patterns were collected under ambient conditions in the range of $2\theta = 1.5°$ to 40.0° with a resolution of 0.04°. Analysis of ZrSBA-15 was carried out through small-angle X-ray scattering (SAXS) on a Siemens small-angle diffractometer with a Siemens HI-STAR area detector, operating at 40 kV and 30 mA ($\lambda = 1.5406$ Å).

Nitrogen adsorption isotherms were obtained at 77 K on a Micromeritics ASAP 2010 Gas Sorption and Porosimetry System. Samples were normally prepared for measurement by degassing at 150 °C under vacuum until a final pressure of 1×10^{-3} Torr was reached. BET surface areas were determined over a relative pressure range of 0.05 to 0.20 [24]. Pore size distributions were calculated using the HK (Horváth-Kawazoe) method [25].

Transmission electron micrographs (TEM) were taken on a JEOL 2000FX transmission electron microscope equipped with a lanthanum hexaboride (LaB_6) gun operating at an accelerating voltage of 200 kV and with an objective aperture of 50 μm. Samples for TEM studies were ground and sprinkled onto a carbon-coated copper grid.

Fourier-transform infrared (FTIR) spectroscopy was performed on a Bio-Rad FTS-60A/896 spectrometer. An MTEC Model 200 photoacoustic (PA) cell allowed non-destructive characterization of the powder samples [26]. PA-FTIR spectra were collected at a scan speed of 5 kHz for wavenumbers of 400 to 4000 cm^{-1} with a resolution of 4 cm^{-1}. Samples were purged under a stream of helium (99.999+%).

Diffuse reflectance UV-Vis spectra were collected on a Cary 5E UV-Vis-NIR spectrophotometer equipped with a Varian diffuse reflectance integrating sphere accessory. Halon was used as a background, and ZrO_2 (99+%, 100% monoclinic phase, Strem) was used as a reference sample. The Kubelka-Munk formalism $F(R_\infty)=(1-R_\infty)^2/(2R_\infty)$ was used, where R_∞ is the reflectance at infinite thickness [27]. The optical absorption edge energy for allowed electron transitions, or band gap energy E_g, was determined by finding the x-intercept of the straight line in the low energy rise of a plot of $[F(R_\infty)\times h\nu]^2$ against $h\nu$, where $h\nu$ is the incident photon energy.

Thermogravimetric analysis (TGA) was performed on a Perkin-Elmer Series 7 Thermal Analysis System. A ramp rate of 5 °C/min was used. Purified nitrogen (99.999+%) was employed as the purge gas.

Bulk elemental analysis through inductively-coupled plasma atomic emission spectroscopy (ICP-AES) was performed by QTI (Whitehouse, NJ). Solid-state ^{29}Si cross-

polarization magic angle spinning nuclear magnetic resonance (CP/MAS-NMR) spectra were collected at a frequency of 53 MHz and a CP contact time of 2 ms by Spectral Data Services, Inc. (Champaign, IL). Samples were spun at 4.0 kHz. Tetramethylsilane was used as the external reference. Surface composition analysis was carried out via X-ray photoelectron spectroscopy on a Surface Science ESCA spectrometer (Model SSX-100) using AlK_{α} radiation.

3.2.3 Catalytic Testing

ZrSi was studied for the gas-phase acid-catalyzed isomerization of 1-butene. 20 mg of ZrSi powder was placed in the middle of a single-pass, downflow quartz reactor. After activating under air at 500 °C for 1 hr and cooled to 350 °C, the catalyst was contacted with a stream of 12% 1-butene in He at 350 °C and 1 atm. The 1-butene feed gas was 99.2+% pure (BOC), with mostly n-butane and isobutane as the impurities. The weight-hourly space velocity (WHSV) was 15 hr^{-1}. Comparison of product distributions over ZrSi2-10 and commercial sulfated zirconia (calcined at 600 °C, MEI) was studied with 50 mg catalyst using a feed of 10.6% 1-butene in He (WHSV of 5.3 hr^{-1}). The effluent was analyzed with a gas-sampling valve-enabled HP 6890 Series Plus GC with a flame induction detector (FID) and a HP-PLOT/Al_2O_3/KCl-deactivated capillary column (ID = 0.32 mm; length = 50 m). The reaction pressure was 1 atm.

The liquid-phase epoxidation of cis-cyclooctene was tested as the oxidation reaction with ZrSi. A Teflon septum-sealed 25-ml flask was charged with 4 ml of dichloromethane (Mallinckrodt), 7.7 mmol of cis-cyclooctene (Lancaster), 0.5 mmol of tert-butyl hydroperoxide (TBHP, 5 M in decane, Aldrich), with 100 µl of chlorobenzene (Sigma-Aldrich) as the internal standard. An amount of catalyst was added such that the total Zr charged was 24 µmol. 50 mg of pure mesoporous silica ZrSi1-0 was used. The flask was placed in a 40 °C silicone oil bath and the reaction mixture was magnetically stirred. Samples were analyzed with a HP 5890 Series II GC equipped with an FID and a HP-1 capillary column (ID = 0.25 mm; length = 30 m). Turnover frequency (TOF) was calculated based on the reaction rate of TBHP, the limiting reagent.

3.3 Results and Discussion

3.3.1 Control of Zirconium Doping in ZrSi Materials

The incorporation of zirconium in the framework of mesoporous silica depended on the amounts of Zr precursor and HCl added to the synthesis mixture, as summarized in Table 3.1. Under highly acidic conditions (pH = -0.25), small amounts of Zr were incorporated into mesoporous silica (2.0-4.4 wt% Zr). The loadings were similar to those achieved through the other synthesis routes [18,19]. The Zr content in these ZrSi1 powders was far lower than that expected for 100% product recovery, indicating that much of the $Zr(SO_4)_2$ precursor in the synthesis mixtures was not incorporated into the silica-surfactant mesostructure.

The Zr contents in the ZrSi2 materials prepared at pH = 0.75 were much higher and closer to the expected doping values (Table 3.1). Reducing the HCl amount by ten times led to a five-fold increase in Zr content, whereas increasing the Zr precursor amount by ten times only doubled the Zr content. Combining these two effects increased the Zr content by 10 times, yielding a silicate material containing 19.6 wt% Zr. Such a high dopant loading in nanoporous silicates has not been reported previously. Clearly, a higher pH has a greater impact on Zr incorporation than a higher Zr precursor amount. The nature of Zr salts is known to be sensitive to solution pH [28]. The $Zr(SO_4)_2$ precursor exists as a polymeric species in solution and, under extremely low pH's, it can exist as monomeric species [29]. Thus, the $Zr(SO_4)_2$ species that enters the templated mesostructure at the two different synthesis pH's may be significantly different. It is noted that, during synthesis, there was no measurable change in pH of the HCl/CTAB solution upon addition of the Zr salt.

The ZrSi2-0.2 sample had a measured Zr content that was higher than the theoretical amount (Table 3.1). This may be attributed to incomplete incorporation of all the Si precursor into the material, resulting in the increase in relative Zr amount. If no $Zr(SO_4)_2$ was used instead of using an amount x = 0.2, two weeks was required for precipitation of a pure silicate material ZrSi2-0, indicating slow condensation kinetics of TEOS under ZrSi2 synthesis conditions. It is noted that this material had no XRD peaks characteristic of a supramolecular-templated mesostructure (Table 3.1).

Calcined ZrSi materials consisting of >4 wt% Zr were found to contain trace amounts of sulfur, presumably in the form of surface sulfates remaining from the $Zr(SO_4)_2$ precursor (Table 3.2). The coverage of ZrSi materials with sulfates is very low, compared to sulfated

zirconia (SZ), a solid acid material known for its very strong acidity [30]. Surface sulfates can generate strong acid sites on zirconia-silica composites [15].

Table 3.2. Sulfur content of selected ZrSi materials.

Sample	Measured Zr Content (wt%)	Measured S Content (wt%)	S/Zr Molar Ratio	Calculated Sulfate Surface Density (SO_4^{2-}/nm^2)
ZrSi1-0	0.0	0.00	0	0
ZrSi1-1	2.0	<0.10[a]	<0.01	<0.01
ZrSi1-10	4.4	0.14	0.09	0.03
ZrSi2-1	10.7	0.52	0.14	0.13
ZrSi2-10	19.6	1.33	0.19	0.57
SZ[b]	74.0[c]	1.61	0.06	3.22

[a]Below detection limit
[b]Sulfated zirconia (calcined at 600 °C; SA = 94 m^2/g)
[c]Calculated Zr amount in ZrO_2

ZrSi could be prepared without the sulfates by using $ZrOCl_2$ instead of $Zr(SO_4)_2$. At a precursor Zr/Si ratio of 0.3, a higher Zr loading resulted from $ZrOCl_2$ (4.5 wt%) than from $Zr(SO_4)_2$ (2.8 wt%); a higher precursor Zr/Si ratio of 1.0 using $Zr(SO_4)_2$ was required for a comparable amount of Zr to be incorporated (4.4 wt%).

3.3.2 Effect of Zirconium Doping on Mesostructure

ZrSi1 materials were able to accommodate the larger Zr cation (r_{Zr} = 0.86 Å vs. r_{Si} = 0.40 Å [31]) with little change to its long-range ordering before or after calcination (Figures 3.1 and 3.2). The hexagonal phase was ascertained by determining the *d*-spacings of the observed XRD peaks and verifying the relation $d_{hk0} = d_{100}/(h^2+hk+k^2)^{1/2}$, where d_{100} is the *d*-spacing value of the main XRD peak. When doped with ≥2.8 wt% Zr, the silicate framework of ZrSi1 contracted slightly more after calcination (Table 3.3). This can be attributed to the octahedrally-coordinated Zr cation's capacity to form more metal-oxygen bonds than tetrahedrally-coordinated Si, increasing the degree of condensation. TEM studies confirmed the long-range, hexagonal pore packing of ZrSi1 (Figure 3.3(a)-(c)). Pore sizes as determined from TEM images are about 25±5 Å. The error arises from the high dependence of observed pore size on sample thickness and imaging focus [32]. The doped ZrSi1 materials has pores of 22 Å by HK analysis, which were slightly smaller than those in undoped silicate (25 Å) (Table 3.3).

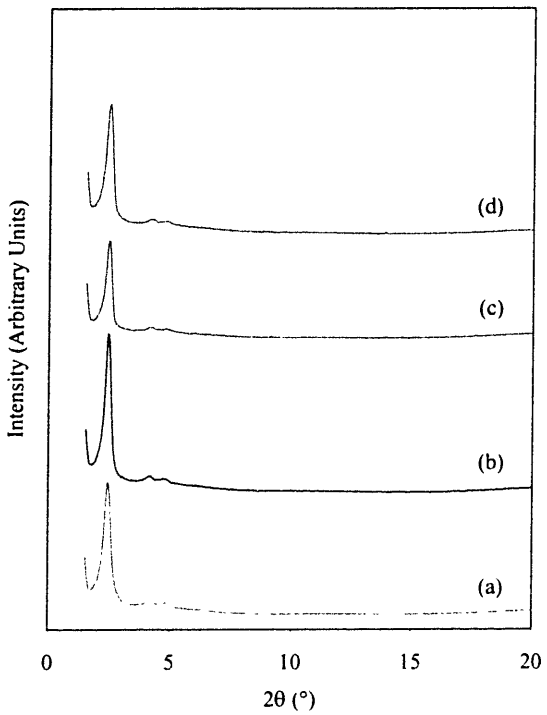

Figure 3.1. XRD patterns of as-synthesized (a) ZrSi1-0, (b) ZrSi1-1, (c) ZrSi1-3, and (d) ZrSi1-10.

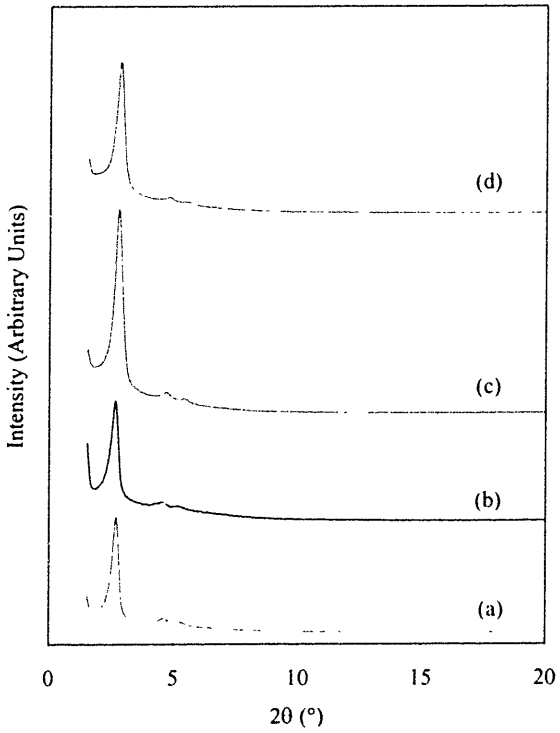

Figure 3.2. XRD patterns of (a) ZrSi1-0, (b) ZrSi1-1, (c) ZrSi1-3, and (d) ZrSi1-10, after calcination at 540 °C.

Table 3.3. Physical properties of ZrSi materials.

Sample	As-synthesized: XRD d_{100} (Å)	Calcined: XRD d_{100} (Å)	Framework Contraction (Å)[a]	Contraction (%)[b]	BET SA (m^2/g)	HK Pore Size (Å)	Pore Wall Thickness (Å)[c]	Pore Volume (cm^3/g)
ZrSi1-0	36.5	33.2	3.8	9	1250	25	13	0.70
ZrSi1-1	36.4	33.2	3.7	9	1193	22	16	0.68
ZrSi1-3	36.4	32.2	4.8	12	1003	22	15	0.53
ZrSi1-10	36.1	31.6	5.2	12	1066	22	14	0.54
ZrSi2-0.2	41.4	37.5	4.5	9	1332	28	15	0.82
ZrSi2-1	38.4	28.4	11.5	26	744	16	17	0.33
ZrSi2-3	38.4	26.4	13.9	31	473	16	14	0.24
ZrSi2-10	37.4	25.8	13.4	31	436	16	14	0.23
ZrSi1-3C	35.6	31.7	4.5	11	1150	21	16	0.63
ZrSBA-15	116[d]	111[d]	5.8	4	942	80	48	1.26

[a]Contraction = a_0(as-synthesized) – a_0(calcined), where a_0 is the center-to-center repeat distance ($2d_{100}/\sqrt{3}$)
[b]Percent change in a_0 after calcination at 540 °C
[c]Wall thickness = a_0(calcined) – (HK pore size)
[d]Determined through SAXS

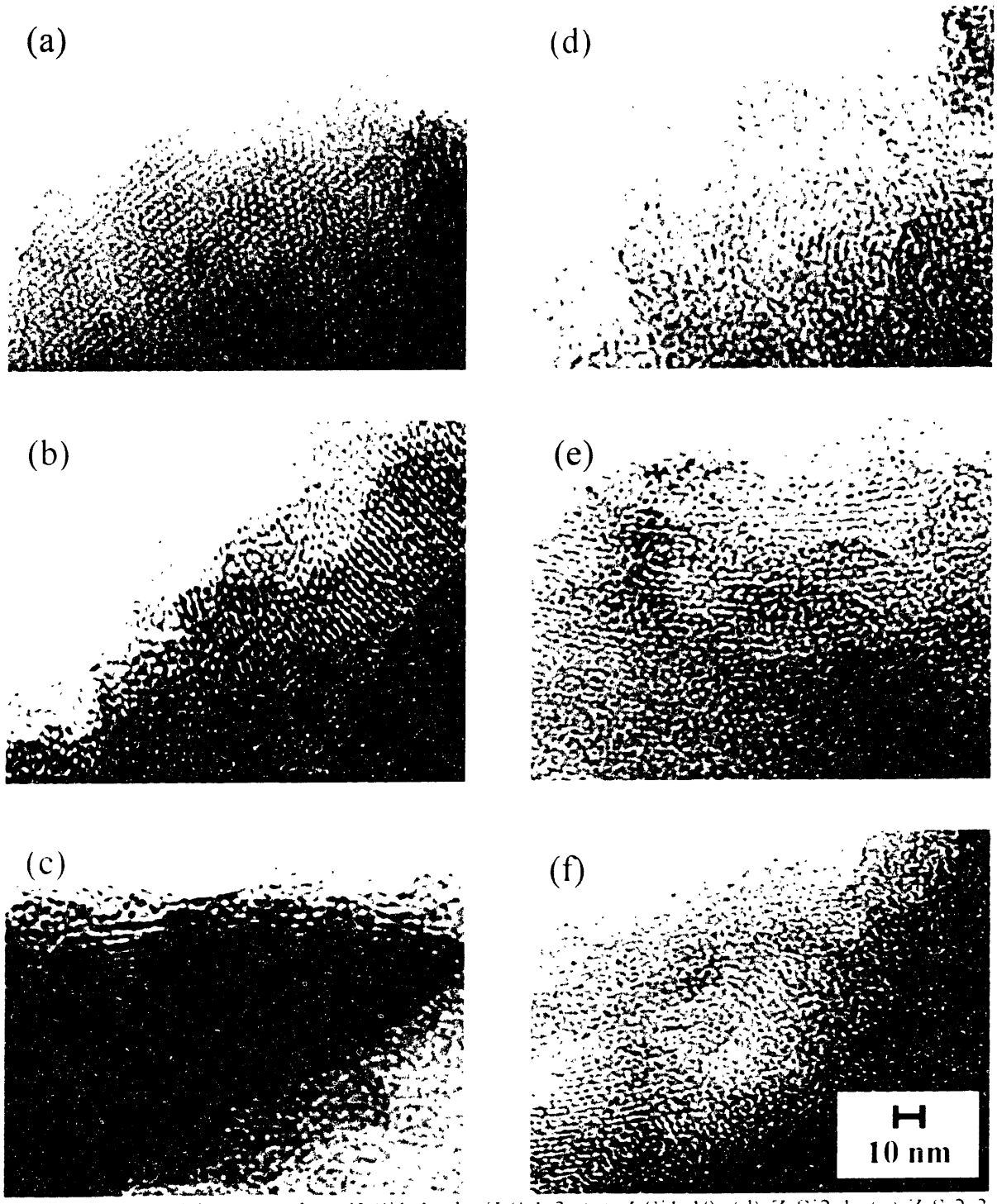

Figure 3.3. TEM images of (a) ZrSi1-1, (b) ZrSi1-3, (c) ZrSi1-10, (d) ZrSi2-1, (e) ZrSi2-3, and (f) ZrSi2-10, after calcination at 540 °C.

The ZrSi1 materials exhibited Type IV nitrogen adsorption isotherms, representative of mesoporous materials (Figure 3.4). These materials did not exhibit hysteresis in their nitrogen adsorption(-desorption) isotherms. Distinguished by nonoverlapping adsorption and

desorption branches, hysteresis is usually observed in mesoporous materials, due to capillary condensation in the open-ended pore channels [24]. While there is no clear explanation still, a critical diameter of ~40 Å exists below which hysteresis in nitrogen adsorption and desorption disappears [33,34].

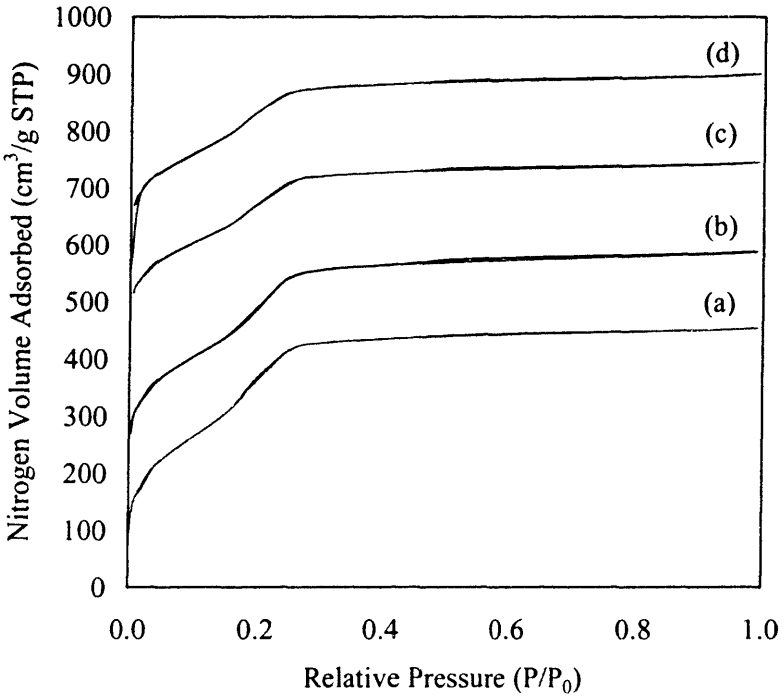

Figure 3.4. Nitrogen adsorption isotherms of (a) ZrSi1-0, (b) ZrSi1-1, (c) ZrSi1-3, and (d) ZrSi1-10, after calcination at 540 °C. Isotherms were offset for clarity.

ZrSi2 materials prepared at pH = 0.75 were structurally different from ZrSi1 materials prepared at pH = -0.25. The as-synthesized ZrSi2 materials prepared at pH = 0.75 were also hexagonal phase (Figure 3.5). The d_{100}-spacings were slightly larger than those of as-synthesized ZrSi1 materials (Table 3.3), which could be due to the much higher amounts of Zr incorporated. However, the as-synthesized ZrSi2 materials had similar d_{100}-spacings (Table 3.3) in spite of the great differences in Zr content within the ZrSi2 series of materials (Table 3.1). Considering that a ZrSi2 material prepared with very little Zr content (ZrSi2-0.2) also had a large d_{100}-spacing, the larger d_{100}-spacings of as-synthesized ZrSi2 materials relative to as-synthesized ZrSi1 materials was therefore attributed to some effect of synthesis pH.

After calcination, the materials contracted more than twice that of ZrSi1 (26-31% vs. 9-12%), resulting in smaller pore sizes (Figure 3.6 and Table 3.3). The calcined ZrSi2

materials were microporous rather than mesoporous, as represented by the Type I nitrogen adsorption isotherms (Figure 3.7). Type I isotherms are typically observed with microporous zeolitic materials [24]. Formation of microporous materials through the contraction of the framework is highly unusual; a microporous phosphated zirconia material was prepared in such a manner [35]. The supramolecular templating of microporous materials typically requires very short amphiphilic molecules [36,37]. TEM studies showed that the ZrSi2 structure was made up of small regions of hexagonally-ordered micropores (Figure 3.3(d)-(f)). Some loss in long-range ordering after calcination is reflected in the disappearance of the higher-order XRD peaks (Figure 3.6). The small rise detected in the isotherms near a relative pressure of 0.99 is indicative of interparticle porosity [24].

After calcination, the special sample of ZrSi2-0.2 exhibited nitrogen adsorption results similar to those of ZrSi1 materials (Table 3.3). ZrSi2-0.2 did not contract as much as ZrSi2 materials, suggesting that a high Zr content was responsible for the significant framework contraction.

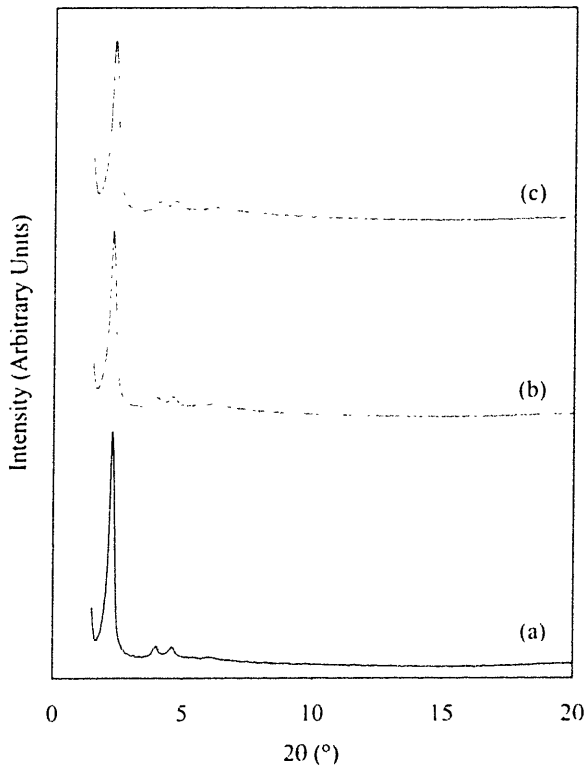

Figure 3.5. XRD patterns of as-synthesized (a) ZrSi2-1, (b) ZrSi2-3, and (c) ZrSi2-10.

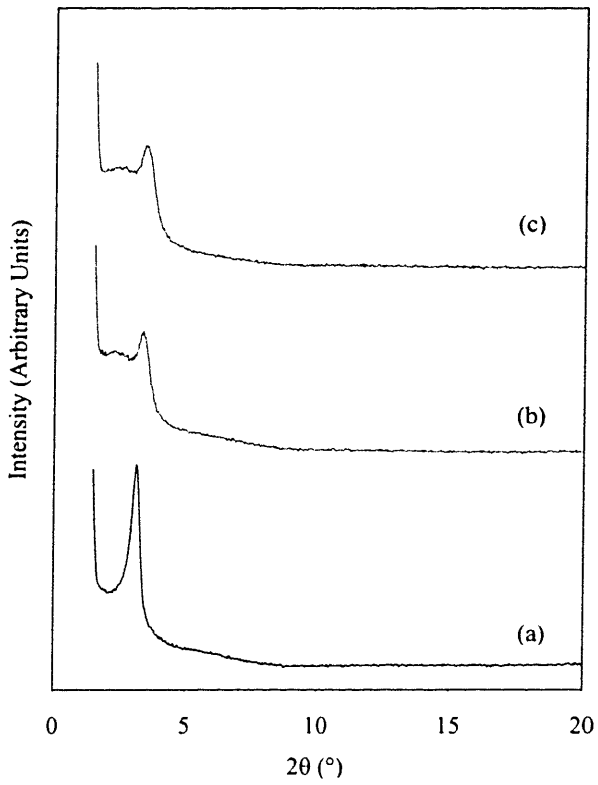

Figure 3.6. XRD patterns of (a) ZrSi2-1, (b) ZrSi2-3, and (c) ZrSi2-10, after calcination at 540 °C.

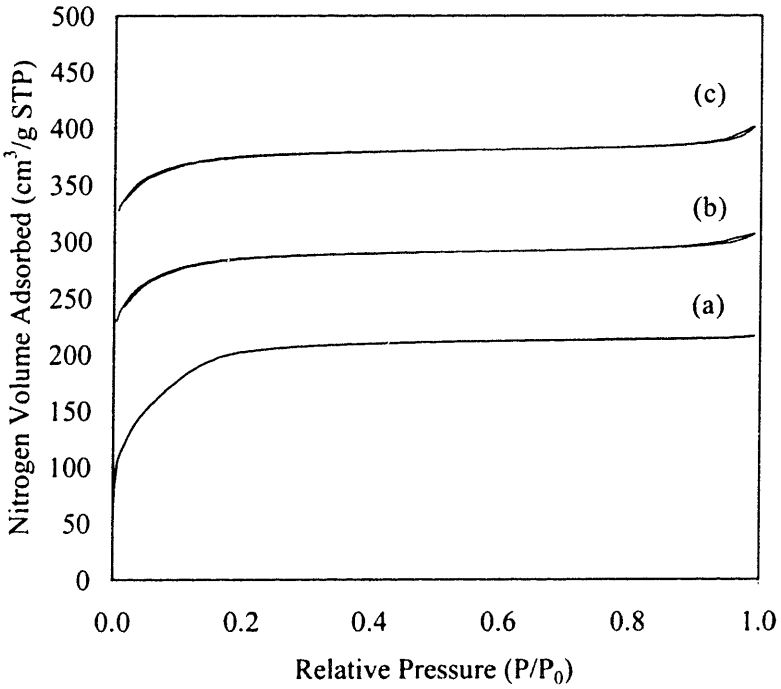

Figure 3.7. Nitrogen adsorption isotherms of (a) ZrSi2-1, (b) ZrSi2-3, and (c) ZrSi2-10, after calcination at 540 °C. Isotherms were offset for clarity.

The lower BET surface areas and pore volumes of ZrSi2 compared to ZrSi1 resulted from the more contracted framework, smaller pore sizes, and higher Zr loading (Table 3.3). Clearly, the Zr-doped silicates have lower surface area and pore volume values compared to undoped mesoporous silica (ZrSi1-0), especially for the ZrSi2 materials doped with >10 wt% Zr. A loading of 2.0 wt% Zr has negligible effect on the surface area and pore volume of the mesoporous framework, and may represent an upper bound to metal doping without structural change to mesoporous silicates. The weight difference between the Zr and Si cations (91.22 g/mol vs. 28.09 g/mol) partially accounted for the decrease in surface areas and pore volumes (Table 3.4). The values were renormalized in terms of total moles of metal cations (Zr + Si) and were found closer to the values of undoped silica. Differences in framework density might also contribute to the decrease in surface area and pore volume with Zr loading, considering that ZrO_2 (3.3 g/cm^3 for amorphous phase, 5.6 g/cm^3 for monoclinic phase) is more dense than SiO_2 (2.2 g/cm^3 for amorphous phase). Given that wall thicknesses of the ZrSi materials did not vary substantially (Table 3.3), the framework would become more dense with increasing Zr loading.

Table 3.4. Surface areas and pore volumes of ZrSi materials normalized in terms of total moles of (Zr + Si) cations.

Sample	Measured Zr Content (wt%)	Surface Area ($\times 10^{-3}$ m^2/mol metal)	Pore Volume (cm^3/mol metal)
ZrSi1-0	0.0	75	42
ZrSi1-1	2.0	73	41
ZrSi1-3	2.8	61	32
ZrSi1-10	4.4	66	33
ZrSi2-1	10.7	48	21
ZrSi2-3	16.2	32	16
ZrSi2-10	19.6	30	16

3.3.3 Nature of Zirconium in the Framework

Several techniques were used to provide insight into the nature of Zr in the silicate framework. The PA-FTIR spectrum of ZrSi1-0 (Figure 3.8(a)) showed the phonon band structure of pure SiO_2: 460 cm^{-1} (O-Si-O bending), 620 cm^{-1} (Si-O-Si deformation), 815 cm^{-1} (symmetric Si-O-Si stretching), 980 cm^{-1} (Si-OH stretching), 1000-1240 cm^{-1} (antisymmetric Si-O-Si stretching), 1625 cm^{-1} (molecular H_2O bending), and 1860 cm^{-1} (SiO_2 overtone) [38]. Subtle changes in the PA-FTIR spectra were observed with increasing Zr dopant amount

(Figure 3.8). The Si-OH stretching peak at 980 cm^{-1} broadened, suggesting interaction between the surface silanol groups with neighboring Zr cations. This effect of Zr has been previously observed in metal-doped zeolites in general [16]. A shoulder peak developed between 880 and 980 cm^{-1}, which is attributed to the Si-O stretching in Si-O-Zr heterolinkages [39]. No separate zirconia phase was found in the ZrSi materials which would exhibit a broad infrared band at ~520 cm^{-1} for the tetragonal phase [40].

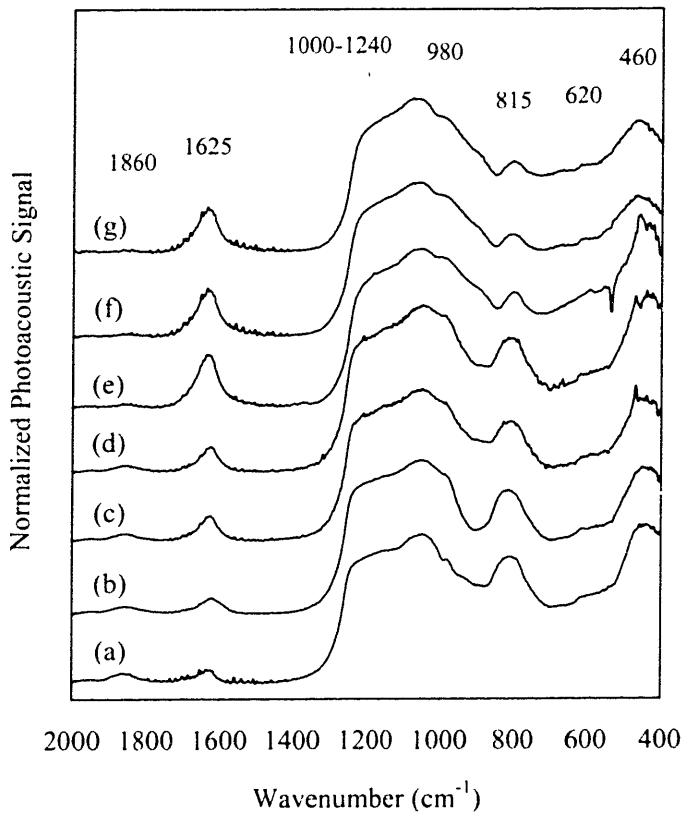

Figure 3.8. PA-FTIR spectra (low-wavenumber region) of (a) ZrSi1-0, (b) ZrSi1-1, (c) ZrSi1-3, (d) ZrSi1-10, (e) ZrSi2-1, (f) ZrSi2-3, and (g) ZrSi2-10, after calcination at 540 °C.

The hydroxyl groups can be detected in the ZrSi materials (Figure 3.9). A peak at 3745 cm^{-1} can be observed in the spectrum of undoped mesoporous silica, indicating the presence of isolated silanol (Si-OH) groups. These groups are associated with Q^2 and Q^3 Si cations as geminal and single silanols, respectively [41]. The notation Q^n denotes the bonding environment of the central Si in $(OSi)_n$–Si–$(OH)_{4-n}$, where n = 0-4. The broad absorption band in Figure 3.9 corresponds to silanols hydrogen bonding with neighboring silanol groups (~3530 cm^{-1}) and to adsorbed water hydrogen bonding with silanol groups (3700-3000 cm^{-1}).

Three types of silanol groups involved in such hydrogen bonding were reported to exist in pure silicate MCM-41 [42]. The position and intensity of the isolated and hydrogen-bonded silanol peaks remained essentially unchanged in the ZrSi1 materials, indicating little effect of Zr doping. ZrSi2 materials showed a much less intense 3745 cm^{-1} peak, indicating a smaller population of isolated silanol groups. Conversely, the broad 3700-3000 cm^{-1} band of ZrSi2 was more intense from the greater amount of hydrogen-bonded silanol and adsorbed water, which was further evidenced by the 1625 cm^{-1} molecular water bending mode in Figure 3.8.

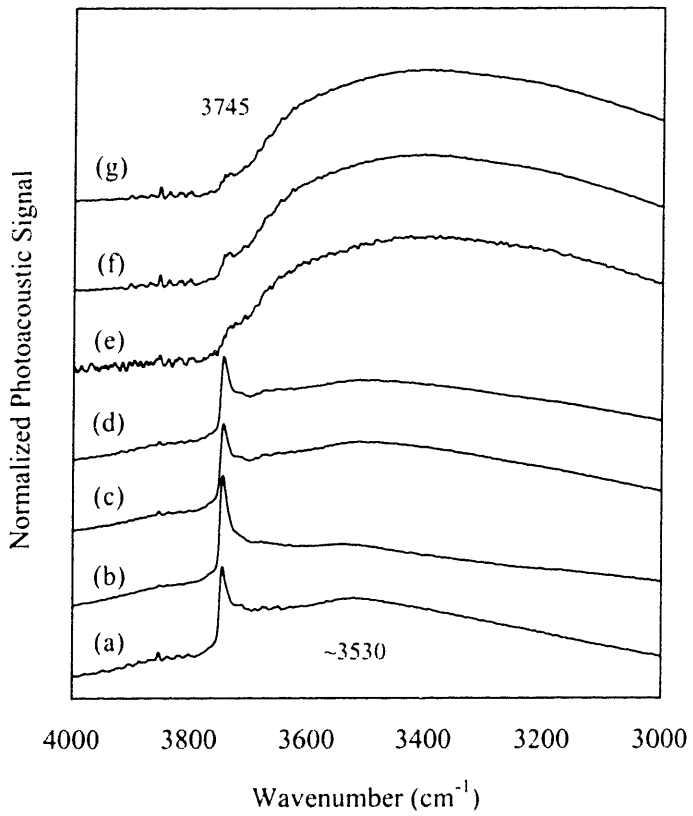

Figure 3.9. PA-FTIR spectra (high-wavenumber region) of (a) ZrSi1-0, (b) ZrSi1-1, (c) ZrSi1-3, (d) ZrSi1-10, (e) ZrSi2-1, (f) ZrSi2-3, and (g) ZrSi2-10, after calcination at 540 °C.

UV-Vis spectroscopy provided insights into the local environment of zirconium cations within the silicate matrix of representative ZrSi samples [19,43]. The UV-Vis spectra of ZrSi1-10 and ZrSi2-10 (Figures 3.10(b)-(c)) did not resemble that of pure zirconia (Figure 3.10(d)), further corroborating the nonexistence of a separate zirconia phase in the ZrSi materials. The single absorption band in the UV-Vis spectra of ZrSi1-10 and ZrSi2-10 represents an O→Zr ligand-to-metal charge transfer (LMCT) transition, which is not found in

pure silicate MCM-41 (ZrSi1-0) [44]. This band blue-shifted to lower wavelengths compared to pure zirconia, which corresponds to larger band gap energies for Zr-doped silicates than for zirconia (Table 3.5) [27]. The blue-shifting also indicates the lack of bulk zirconia in ZrSi materials and suggests the presence of isolated zirconium cations [16,45]. ZrSi2-10 has a smaller E_g than ZrSi1-10, which suggests some connectivity among the greater amount of Zr cations.

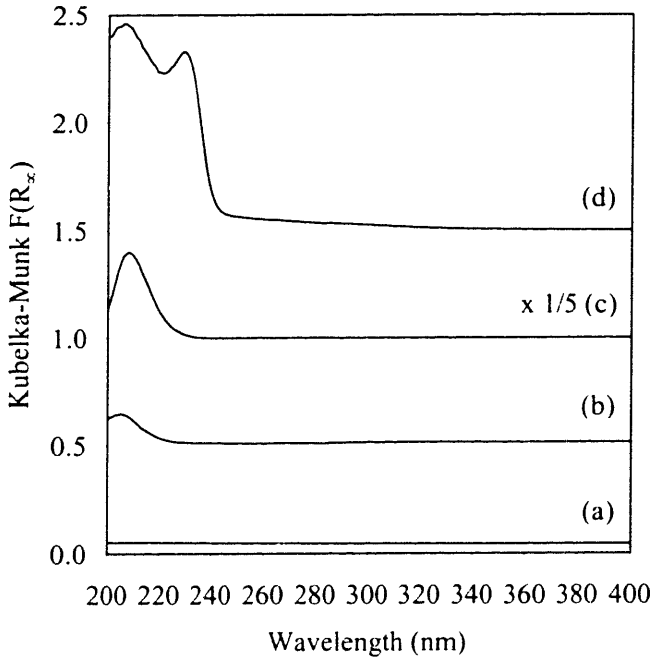

Figure 3.10. UV-Vis spectra of (a) ZrSi1-0, (b) ZrSi1-10, (c) ZrSi2-10, after calcination at 540 °C; and (d) ZrO_2. Spectra were offset for clarity.

Table 3.5. UV-Vis maxima and band gap energies of representative ZrSi materials.

Sample	Zr Content (wt%)	Band Maximum (nm)	E_g (eV) (±0.05)
ZrSi1-0	0	N/A	N/A
ZrSi1-10	4.4	205	5.75
ZrSi2-10	19.6	208	5.65
ZrO_2	74.0	206, 229	5.20

^{29}Si CP/MAS-NMR was performed on representative samples of ZrSi to examine qualitatively how Zr perturbed the local bonding environment of surface Si. The ^{1}H-^{29}Si CP technique intensifies the NMR signal of Si atoms near protons, and so it is useful in studying the Si atoms located at or below the pore wall surface [46,47]. ZrSi1-0, ZrSi1-10, and ZrSi2-

10 were found to contain three types of Si: Q^2 (-90 ppm), Q^3 (-99 ppm), and Q^4 (-109 ppm) (Figure 3.11). It is assumed that the Q^2 and Q^3 Si are exposed directly at the surface, as silanol groups are unlikely to reside within the thin pore walls (as internal Q^3 Si) without diminishing structural integrity. The Q^4 Si atoms can lie within the framework or at the surface [48]. The amount of Si bonded to Zr, e.g. $(OSi)_2$–Si–$(OZr)_2$ and $(OSi)_3$–Si–OZr, could not be determined through ^{29}Si CP/MAS-NMR, and would be difficult to measure quantitatively with ^{29}Si MAS-NMR because of overlapping resonance peaks with Q^2 and Q^3 Si sites, respectively [49,50]. ^{29}Si MAS-NMR would be useful, though, in quantifying the relative amounts of Q^2, Q^3, and Q^4 sites.

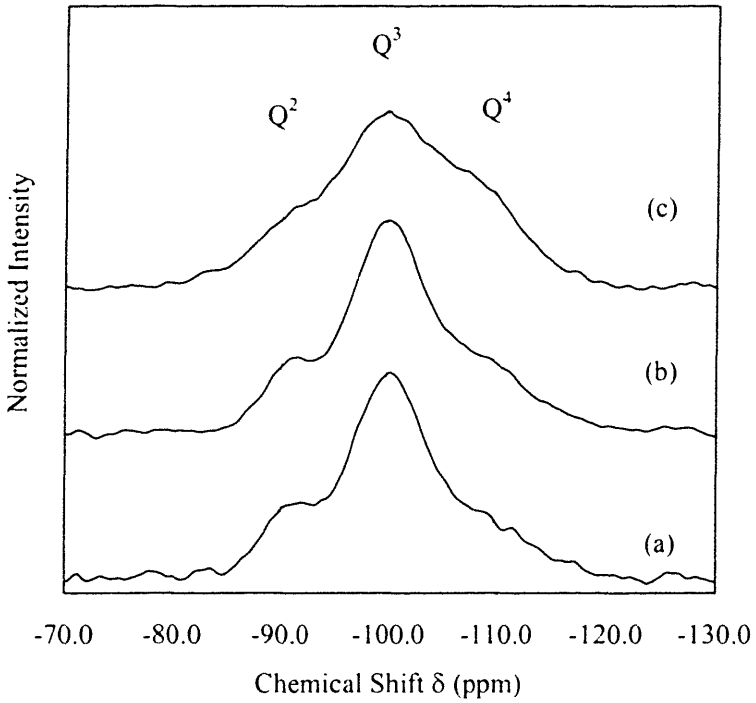

Figure 3.11. ^{29}Si CP/MAS NMR spectra of (a) ZrSi1-0, (b) ZrSi1-10, (c) ZrSi2-10, after calcination at 540 °C

The similarity between the Si site ratios of ZrSi1-0 and ZrSi1-10 shows that the incorporation of 4.4 wt% Zr did alter significantly the population of surface Si species of the pure silicate framework (Table 3.6). On the other hand, ZrSi2-10 differs greatly from either ZrSi1-0 or ZrSi1-10. The loss in Q^3 Si sites in ZrSi2-10 was consistent with the decrease in the PA-FTIR isolated silanol peak at 3745 cm^{-1} (Figure 3.9). A greater percentage of Q^4 Si atoms was detected in ZrSi2-10. PA-FTIR data (Figure 3.9) indicated an increase in the

hydrogen bonding band, which can be attributed to hydroxyl groups associated with surface Zr cations; this suggests that the Q^4 atoms in ZrSi2-10 lie at the surface sites. The differences in the chemical environment of surface Si in ZrSi2-10 compared to pure silicate ZrSi1-0 or ZrSi1-10 may be ascribed to the more contracted, condensed framework of ZrSi2-10.

Table 3.6. Relative ^{29}Si CP/MAS NMR spectra peak areas and chemical shifts of representative ZrSi materials.

Sample	Zr Content (wt%)	$\%Q^2$ Si Sites	$\%Q^3$ Si Sites	$\%Q^4$ Si Sites
ZrSi1-0	0.0	16.5	58.2	25.3
ZrSi1-10	4.4	15.1	60.8	24.1
ZrSi2-10	19.6	16.3	44.0	39.7

3.3.4 Surfactant-Framework Interactions in ZrSi

The strength of interactions between the surfactant and the framework, as a function of Zr doping, was studied through TGA under inert atmosphere. The weight loss of the undoped silicate ZrSi1-0 was found to occur in two stages (Figure 3.12(a)). The broad peak at 260 °C denotes the loss of CTAB through pyrolysis and the peak at 410 °C is attributed to loss of carbonaceous deposits. With increasing Zr dopant amounts, the peak at 260 °C decreased and a new peak at ~350 °C grew and shifted to higher temperatures (Figures 3.12(b)-(g)). Two populations of surfactant molecules with different bonding strengths were observed as a function of Zr loading. The more strongly-bound CTAB surfactants, represented by the peak at the higher temperature of ~350 °C, could be associated with Zr cations; and the less strongly-bound surfactants, represented by the peak at 260 °C, could be associated with Si cations. The implication is that the Zr precursor interacted with the surfactant during synthesis. Analogous surfactant-framework interactions were found in Al-doped mesoporous silicates, whereby amine surfactants were bonded strongly to Al cations [51].

A third peak emerged at 520 °C in ZrSi2 materials with Zr amounts of ≥10.7 wt%, representing the loss of water of condensation from the severe contraction of the framework (Figures 3.12(e)-(g)). Total weight loss by 600 °C was *ca.* 56% for these ZrSi2 materials, compared to *ca.* 47% for pure silicate ZrSi1-0 and ZrSi1 materials.

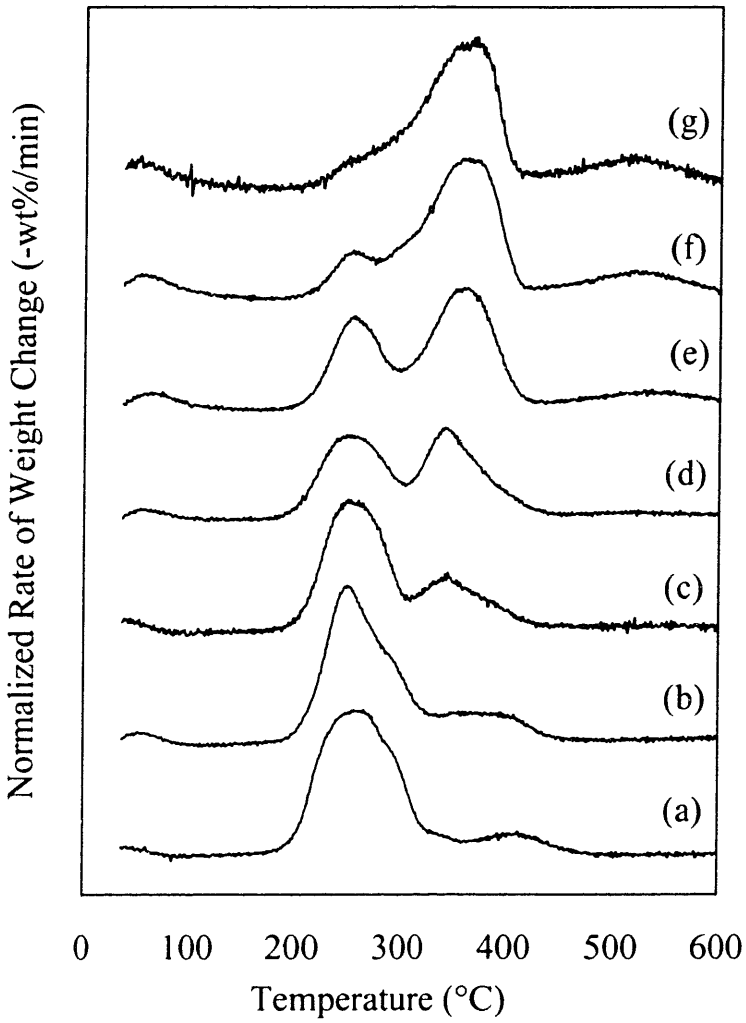

Figure 3.12. Derivative of weight loss TGA profiles (under nitrogen) of as-synthesized (a) ZrSi1-0, (b) ZrSi1-1, (c) ZrSi1-3, (d) ZrSi1-10, (e) ZrSi2-1, (f) ZrSi2-3, and (g) ZrSi2-10. Profiles were offset for clarity.

3.3.5 Synthesis Mechanism

In the formation of pure mesoporous silica under low-pH conditions ($S^+X^-I^+$ pathway), it has been postulated that the anion X^- from the acid (or from the surfactant) mediates the electrostatic interplay between the positively-charged head group of CTAB (S^+) and the positively-charged Si precursor (I^+) hydrolyzed from TEOS [21]. This synthesis route contrasts the S^+I^- (high pH) [4] and S^0I^0 (neutral pH) pathways [52]. In the case of ZrSi1-0, the Cl anion from the HCl is in excess of Br^- (from CTAB) by ~40 times and is the mediating anion. Supramolecular-templated silicates prepared in a similar fashion were found to contain 2 wt% Cl, hinting at the active role Cl^- plays in the synthesis [53]. Through our Zr doping

studies we have found that the synthesis of ZrSi materials supports the $S^+X^-I^+$ electrostatic interactions model. Our synthesis procedures involve the addition of $Zr(SO_4)_2$ (or $ZrOCl_2$) to the synthesis mixture as the I^+, leading to the incorporation of Zr into the silicate framework. However, this model does not explain the unusual ability to incorporate the high loadings of Zr (>4 wt%) observed in ZrSi materials.

The quantity of Zr incorporated depended greatly on synthesis pH (Table 3.1), suggesting a pronounced sensitivity of Zr doping to the solution chemistry of Zr cations. It is known that Zr cations can exist in various solubilized forms depending on the Zr counteranion and pH [28,29]. As mentioned earlier, $Zr(SO_4)_2$ exists as a polymerized species in solution, with the SO_4 acting to complex multiple Zr cations [29]. This cationic polymeric species is concluded to be directly involved in the charge interaction with CTAB, as sulfur was detected in the ZrSi materials prepared with $Zr(SO_4)_2$.

At the lower synthesis pH of -0.25, the HCl/CTAB solution remained clear upon introduction of the $Zr(SO_4)_2$ solution. No precipitation was observed before TEOS addition. At the higher pH of 0.75, the solution became cloudy 2 hr after combining with $Zr(SO_4)_2$. These experiments show that $Zr(SO_4)_2$ can interact directly with the templating surfactant, as suggested by the TGA studies. The highly favorable interaction between $Zr(SO_4)_2$ and CTAB explains why the materials prepared at pH = 0.75 (ZrSi2) contain much more Zr than those prepared at pH = -0.25 (ZrSi1).

In our synthesis of ZrSi2 materials, TEOS was immediately added after $Zr(SO_4)_2$ introduction to the HCl/CTAB solution. If TEOS was added 2 hr after the introduction of $Zr(SO_4)_2$, a thermally-unstable, hexagonally-ordered precipitate would result. When TEOS was withheld from the synthesis mixture, a hexagonally-ordered precipitate would be produced after 2 days of aging, but its mesostructure would collapse upon surfactant removal. These experiments indicate that SiO_2 provides the thermal stability lacking in a pure ZrO_2 framework, and that the TEOS precursor must be added before the precipitation of $Zr(SO_4)_2$/CTAB mesostructure. Further, the low synthesis pH of -0.25 inhibits the formation of this $Zr(SO_4)_2$/CTAB precipitate. This mesostructured material is similar to those studied by Ciesla *et al.*, who also found that these materials lacked thermal stability [35].

The preferential location of the Zr cation at the surface, as implied by direct interaction of $Zr(SO_4)_2$ and CTAB, and by the presence of strongly bound CTAB, was

substantiated by XPS results (Table 3.7). The Zr surface content of representative ZrSi materials was found greater than their respective bulk Zr composition.

Table 3.7. Bulk and surface concentrations of representative ZrSi materials.

Sample	Bulk Zr Content (wt%)	Surface Zr Content (wt%)
ZrSi1-10	4.4	12.6
ZrSi2-10	19.6	25.5
ZrSi1-3C	4.5	9.4
ZrSBA-15	4.8	10.7

$ZrOCl_2$ precursor was found a more effective dopant than $Zr(SO_4)_2$ in the preparation of ZrSi1 materials at pH = -0.25 (Table 3.1). This may be due to tetrameric molecular species $[Zr_4(OH)_8(H_2O)_{16}]^{8+}$ in solution arising from dissolved $ZrOCl_2$ [28,29]. In an analogous fashion as $Zr(SO_4)_2$ polymeric species, this tetrameric species is able to interact with CTAB, as suggested by the excess Zr on the surface determined by XPS (Table 3.7). The higher synthesis pH of 0.75 did not lead to precipitation when $ZrOCl_2$ was added to a HCl/CTAB solution, unlike the case of $Zr(SO_4)_2$, indicating less favorable interactions between the $ZrOCl_2$ precursor and CTAB. In fact, even after the addition of TEOS, no product was formed from this final solution of HCl/CTAB/$ZrOCl_2$/TEOS (pH = 0.75). Clearly, the sulfate plays a crucial role in the doping of mesostructured silica with Zr.

Synthesis mixtures at pH = -0.25 and 0.75 differ not only in the amount of available protons but also in the amount of Cl anions. The ion concentration, which can be characterized by ionic strength I (= $\frac{1}{2}\Sigma cz^2$, where c is concentration and z is valence charge), is different at the two different pH synthesis conditions (1.77 M at pH = -0.25 vs. 0.18 M at pH = 0.75), and would impact the electrostatic interactions necessary for ZrSi formation. The effect of ion concentration was tested by adding an amount of KCl to the above synthesis solution of HCl/CTAB/$ZrOCl_2$/TEOS (pH = 0.75) such that the total number of Cl anions was the same as that found in the synthesis mixture at pH = -0.25. A non-mesostructured precipitate resulted after two days of aging, indicating a high ion concentration could induce precipitation, but a sufficient amount of protons was required for supramolecular templating to take place.

3.3.6 Gas-Phase 1-Butene Isomerization

1-Butene isomerization is a useful acid-catalyzed reaction to probe the strength of acid sites [54]. Whereas the double-bond isomerization of 1-butene to cis-2-butene and trans-2-butene occurs over acid sites of moderate strength, skeletal isomerization to isobutene is catalyzed over strong acid sites in a separate reaction pathway (Figure 3.13).

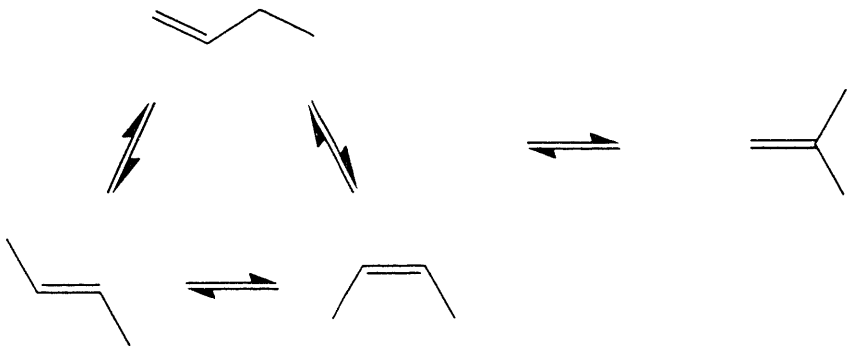

Figure 3.13. Reaction scheme of 1-butene isomerization.

1-Butene isomerization was used to examine the effect of Zr loading on the acidity of ZrSi materials. Initial activities of the ZrSi materials were studied because deactivation from coke formation occurred time-on-stream. The total conversion and skeletal isomerization of 1-butene increased with Zr amount doped (Figure 3.14). This activity profile with increasing Zr doping levels is commonly observed in mixed metal oxides and is attributed to increased heterolinkages between Zr and Si cations [13-15,55]. An optimum number of Zr-O-Si linkages leads to volcano-like behavior in catalytic activity and acidity found with zirconia-silica and other binary mixed metal oxides [13]. No such maximum in skeletal isomerization activity was observed with the ZrSi materials over the range of composition achieved.

In addition, there is some enhancing effect of SO_4^{2-} on the observed isomerization activity, as observed by other researchers with sulfated zirconia-silica materials [15]. As shown in Figure 3.14, the initial isomerization activity of ZrSi1-3C sample (containing 4.5 wt% Zr with no sulfates) was found to be 50% that of ZrSi1-10, which contains 4.4 wt% Zr and 0.14 wt% S (Table 3.2). ZrSi1-3C has a slightly greater surface area than ZrSi1-10 by <8% (Table 3.3). The presence of sulfates at a low surface density of 0.03 SO_4^{2-}/nm^2 was sufficient to increase the catalytic activity of ZrSi. While sulfates are known to create active

sites on zirconia, the actual nature of the acid site remains elusive, especially with sulfated zirconia-silica systems [15,30]. It is generally accepted, however, that the sulfates generate acid sites of the Brønsted type, which are active for acid catalysis. Brønsted acid sites are hydroxyl groups, but only a fraction of the hydroxyl groups present would contribute to Brønsted acidity [56]. For an order-of-magnitude comparison, the surface density of hydroxyl groups for pure MCM-41 was reported to be 2.5-3.0 SiOH/nm^2 [47], compared to the average value of 4.6 SiOH/nm^2 for amorphous silica [57].

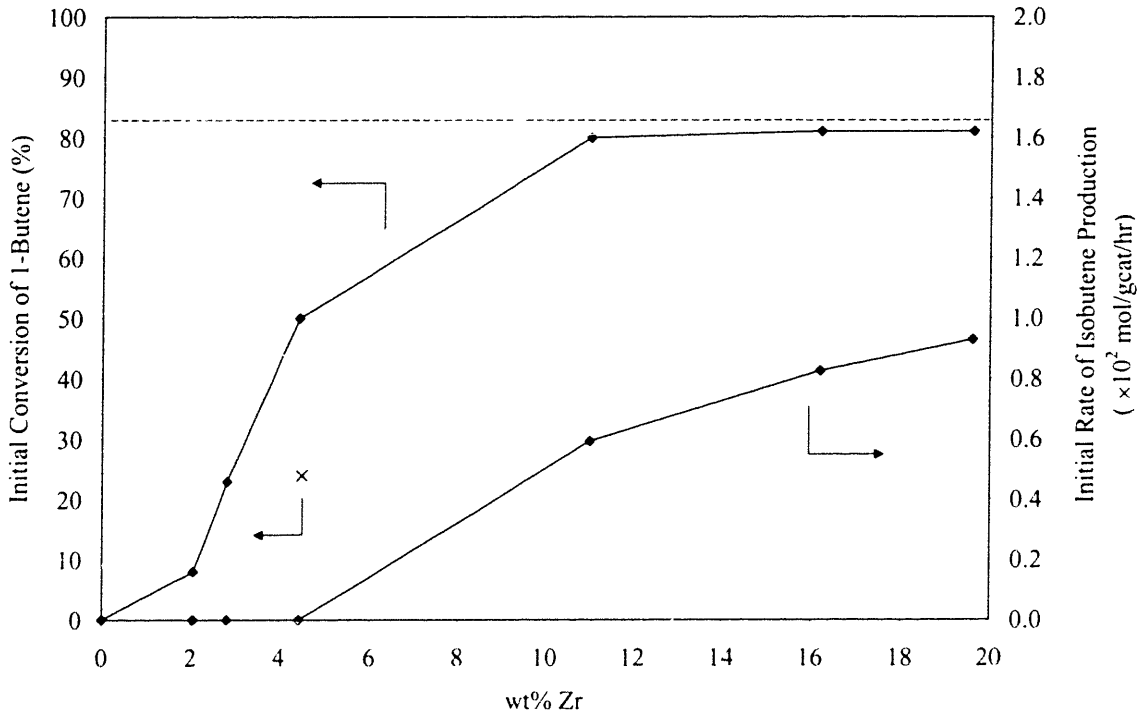

Figure 3.14. Initial conversion of 1-butene and initial rate of isobutene production at 350 °C as a function of Zr content in ZrSi materials prepared with $Zr(SO_4)_2$ (◆) and with $ZrOCl_2$ (×). The dotted line indicates the thermodynamic conversion of 1-butene at 350 °C (82%).

Conversion of 1-butene approached an asymptotic value of 82% with increasing Zr loadings in ZrSi. The gas-phase products are cis- and trans-2-butene isomers in equilibrium amounts, and trace amounts of isobutene, propene, pentenes, and butanes (3% selectivity from 1-butene). Under the reaction conditions used, the double-bond isomerization is a much more facile reaction than skeletal isomerization and side-reactions [58]. With the low conversion to isobutene and side-products, it is reasonable to calculate the equilibrium conversion of 82%

based on double-bond isomerization products. Higher conversion of 1-butene cannot occur through double-bond isomerization, but may be achieved by increasing reaction rates to other products.

The gas-phase products formed over ZrSi doped with <5 wt% Zr were cis- and trans-2-butenes exclusively, indicating the existence of medium-strength acid sites. The more heavily-doped ZrSi materials catalyzed the formation of 2-butenes and also isobutene (Figure 3.14). The formation of isobutene has been studied extensively over a variety of catalysts, such as zeolites [59], halogenated aluminas [60], and tungsten oxide-based materials [61] because of the commercial importance of isobutene [58]. Zeolites have been proposed to catalyze skeletal isomerization via a monomolecular mechanism, i.e. a linear butene molecule rearranges into isobutene through a methylcyclopropyl carbenium ion [59]. Non-zeolitic materials have been found to catalyze a bimolecular mechanism, i.e. two butenes dimerize into an octene, which isomerizes before cracking to give isobutene [58]. Over both zeolitic and non-zeolitic catalysts, byproduct formation goes through a bimolecular pathway.

The ZrSi catalysts likely involves a bimolecular mechanism for several reasons. The monomolecular reaction pathway appears to occur only in the highly constrained micropores of zeolites e.g. ferrierite (a zeolite with pore sizes of 4.2 Å × 5.4 Å), which are smaller than the micropores of ZrSi2 materials. Further, the propene and pentene byproducts (roughly same molar amounts) detected over ZrSi result from a bimolecular reaction, in which the octene intermediate cracks at a different carbon site to give the disproportionation products. Small amounts of n-butane and isobutane were also found, resulting from hydrogen-transfer reactions.

Both ZrSi2-10 and SZ were found very active for the conversion of 1-butene but a closer examination of the product distribution revealed differences in catalytic activity (Table 3.8). Both catalysts was active for isobutene production, with ZrSi2-10 showing a higher selectivity than SZ. Isobutene selectivity was based on total linear butenes available (1-butene + 2-butenes), as 2-butenes can also undergo skeletal isomerization to isobutene. The isobutene yield was higher over SZ than over ZrSi2-10 because the latter coked much more, resulting in a loss of gas-phase products. After 42 min on stream, isobutene yield and selectivity reduced to similar values over both catalysts. One of the most effective catalysts for 1-butene skeletal isomerization is ferrierite, a ten-member ring zeolite patented by Shell

[59]. Under approximately similar reaction conditions (350 °C, 1.4 atm and a WSHV of 2.0 hr^{-1}), ferrierite was reported to have a steady-state isobutene selectivity of 81% [59b], significantly better than the non-zeolitic ZrSi2-10 and SZ catalysts.

Table 3.8. Conversion of 1-butene over ZrSi2-10 and SZ.[a]

	ZrSi2-10		SZ	
Zr Content (wt%)	19.6		74	
S Content (wt%)	1.33		1.61	
Surface Area (m^2/g)	436		94	
Pore Size (Å)	16		25	
Product Distribution (vol%)	Initial	42 min TOS	Initial	42 min TOS
Methane	0.003	0	0	0
Ethane	0.002	0	0.001	0
Ethylene	0.002	0	0.004	0
Propane	0.008	0	0.003	0
Propene	0.424	0.063	0.378	0.057
n-Butane	0.094	0.001	0.040	0.009
Isobutane	0.360	0.009	0.171	0.007
1-Butene	0.980	2.767	1.780	2.408
trans-2-Butene	1.767	4.077	3.398	4.402
cis-2-Butene	1.286	3.282	2.470	3.267
Isobutene	0.749	0.361	1.190	0.382
Pentenes	~0.26	~0.06	~0.33	~0.05
Total 1-Butene Conversion (%)	91	74	83	77
Selectivity to Isobutene (%)[b]	15.7	3.4	13.5	3.6
Loss to Coke Formation (%)[c]	46.6	<1.0	11.1	<1.0

[a]Reaction conditions: 350 °C, 1 atm, WHSV = 5.3 hr^{-1}
[b]Defined as isobutene/(total butenes detected)
[c]Calculated as (initial 1-butene) – (total products detected)

Gas-phase products besides butenes were detected, signifying that side-reactions take place in parallel. Propene and pentenes would be produced in equal amounts from the disproportionation of butenes. In this case, an excess of propene was detected, which might have come from the cracking of butenes or butanes. Small amounts of methane and ethylene, likely cracking products, were also detected. The presence of saturated hydrocarbon products indicates hydrogen-transfer reactions also occurred, i.e. hydrogenation of alkenes to alkanes. These reactions are known to be catalyzed by strong acid sites, which must be present on ZrSi2-10 and SZ. The products of these undesired reaction pathways became insignificant after 42 min, indicating the acid sites for these pathways deactivated. As a result, overall

conversion of 1-butene dropped to similar levels. Also, coke formation (calculated by mass balance on hydrocarbons in feed and in effluent) became negligible. Coke formation was confirmed visually, as the initially white catalysts turned black after reaction. It is concluded that the acid sites active for the unselective conversion of 1-butene deactivated from coke formation, but the acid sites for double-bond and skeletal isomerizations were still operative.

3.3.7 Liquid-Phase cis-Cyclooctene Epoxidation

ZrSi materials were tested for liquid-phase oxidation activity with the epoxidation of cis-cyclooctene using an organic source of oxygen, tert-butylhydroxyperoxide (TBHP). The cyclooctene oxide is the sole product. The epoxide is resistant to acid-catalyzed isomerization and ring-opening reactions, making the reaction simple and convenient to follow (Figure 3.15) [62]. Epoxidation reactions lead to products important as precursors to polymers and fine chemicals.

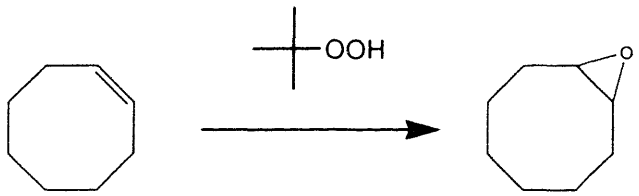

Figure 3.15. Reaction scheme of cis-cyclooctene epoxidation.

The extent of reaction was tracked by following the loss of TBHP as it reduced to t-butanol. The homolytic decomposition of TBHP was found to be negligible. Pure silicate ZrSi1-0 was catalytically inert, while the Zr-doped mesoporous silicates were active, indicating the requirement of Zr sites for epoxidation to occur (Figure 3.16). Both ZrSi1-10 and ZrSi1-3C catalyzed the epoxidation reaction (Figures 3.16(b)-(c)), but ZrSi1-3C was three times more active than ZrSi1-10 (Table 3.9). These two doped silicates have similar Zr content, surface area and pore size, suggesting that SO_4^{2-} is responsible for the disparity in activity. For doped zeolites used as redox catalysts, an important requirement is the presence of coordinatively unsaturated metal cations as strong Lewis acid sites (and as weak redox sites so that the undesired decomposition of the oxidizing agent is not promoted) [63]. While ZrSi1-10 and ZrSi1-3C possess surface-exposed Zr sites, some of the Zr cations in ZrSi1-10

are inferred to be coordinated with surface sulfate groups. These sulfates reduce the amount of active Zr sites available for epoxidation catalysis, as substantiated by the difference in epoxidation rates between ZrSi1-10 and ZrSi1-3C.

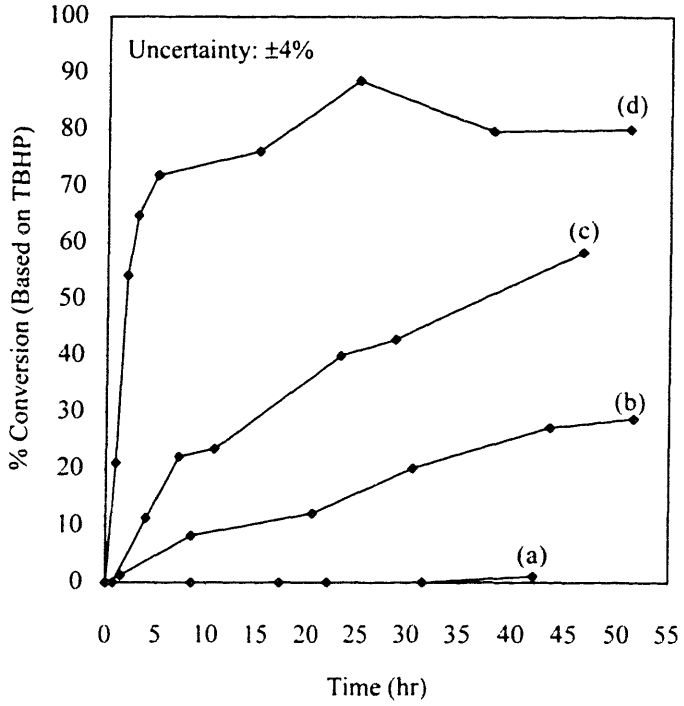

Figure 3.16. Conversion-time profiles of cis-cyclooctene epoxidation with TBHP at 40 °C, using (a) ZrSi1-0, (b) ZrSi1-10, (c) ZrSi1-3C, and (d) ZrSBA-15.

Table 3.9. Properties and cis-cyclooctene epoxidation activity of mesoporous Zr-doped silicates.[a]

Sample	Zr Content (wt%)	S Content (wt%)	BET SA (m^2/g)	Pore Size (Å)	TOF (hr^{-1})
ZrSi1-0	0.0	0	1250	25	0.00
ZrSi1-10	4.4	0.14	1066	22	0.21
ZrSi1-3C	4.5	0	1150	21	0.65
ZrSBA-15	4.8	0	942	80	5.77

[a]Reaction conditions: T = 40 °C, 4 ml CH_2Cl_2, 7.7 mmol cis-cyclooctene, 0.5 mmol TBHP, 100 µl chlorobenzene, 24 µmol Zr^{4+}.

The effect of pore size on epoxidation was examined. An ultralarge-pore analogue of ZrSi was prepared in the form of Zr-doped SBA-15 (Figure 3.17). Its pore size was 80 Å, about 4 times larger than that of ZrSi1-3C (Table 3.9). The overall conversion (Figure 3-

16(d)) and TOF (Table 3.9) over this ultralarge-pore material were significantly greater than ZrSi1-10 and ZrSi1-3C, which have similar Zr contents.

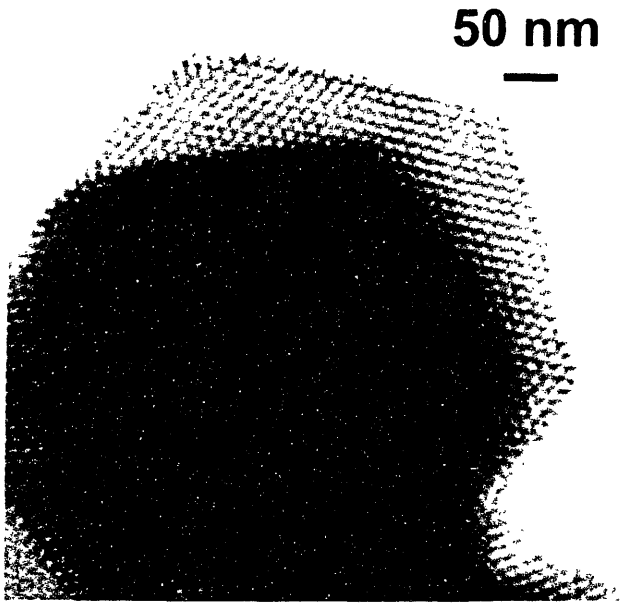

Figure 3.17. TEM image of ZrSBA-15, after calcination at 540 °C.

The enhancement in reaction activity may be explained in terms of pore size and its effect on the diffusion of reactants. Diffusion in liquids are characterized by diffusion coefficient values on the order of 10^{-5} cm^2/s, compared to bulk gas-phase diffusivities of 10^{-1} cm^2/s [64]. Gas-phase diffusion in a porous matrix becomes affected by pore sizes below 100 nm, where Knudsen diffusion occurs. When the pore size approaches the mean free path of gas molecules, as in the case of Knudsen diffusion, the kinetic theory of gases teaches the equation

$$D_K = 9700R\sqrt{\frac{T}{M}},$$

where D_K is Knudsen diffusivity (cm^2/s), R is pore radius (cm), T is absolute temperature, and M is molecular weight [65]. While there is no equivalent relation for liquid diffusion in fine pores, a similar effect of pore size on diffusion would be expected. Diffusive transport of TBHP (5.1 Å) and cis-cyclooctene (5.3 Å) through the pore channels would be more hindered in 21-Å pores than in 80-Å pores, resulting in a lower effective diffusivity D_{eff}. At high

Thiele moduli, the effectiveness factor is roughly proportional to D_{eff}, and thus the overall epoxidation reaction rate would be lowered.

ZrSBA-15 has a smaller surface area than ZrSi1-3C and could be expected to reduce rate of epoxidation. Its ~9 times greater TOF for epoxidation catalysis indicates that accessibility to the active sites significantly facilitated this reaction. It is noted that other factors might also have an effect on the observed catalytic behavior, such as non-uniform particle size, bent pore channels, channels of varying lengths, and differences in surface Zr enrichment (Table 3.7).

3.4 Summary

Thermally stable, well-defined porous Zr-doped silicates containing up to 20 wt% Zr were successfully synthesized. The low-pH condition was critical towards achieving such high levels of Zr doping while maintaining the MCM-41-type mesostructure. The incorporation of Zr was found highly dependent on the synthesis pH and the nature of the Zr salt precursor. The resulting ZrSi mesoporous materials had very high surface areas, uniform pore sizes, and long-range ordering, as characterized by XRD, nitrogen sorption analysis, and TEM. Microporosity was achieved in ZrSi materials containing >10 wt% Zr. Zr cations were found highly dispersed throughout the silicate framework, according to PA-FTIR and UV-Vis spectroscopies, and no bulk zirconia phases were detected. The ZrSi materials showed high activity in the gas-phase isomerization of 1-butene, increasing with the Zr doping level and the surface sulfate content. They also exhibited activity for the liquid-phase cis-cyclooctene epoxidation, which was significantly bolstered by ultralarge pores.

3.5 References

[1] Sayari, A. *Chem. Mater.* **1996**, *8*, 1840.

[2] Corma, A. *Chem. Rev.* **1997**, *97*, 2373.

[3] Ying, J. Y.; Mehnert, C. P.; Wong, M. S. *Angew. Chem. Int. Ed.* **1999**, *38*, 56.

[4] (a) Kresge, C. T.; Leonowicz, M. E.; Roth, W. J.; Vartuli, J. C.; Beck, J. S. *Nature* **1992**, *359*, 710. (b) Beck, J. S.; Vartuli, J. C.; Roth, W. J.; Leonowicz, M. E.; Kresge, C. T.; Schmitt, K. D.; Chu, C. T.-W.; Olsen, D. H.; Sheppard, E. W.; McCullen, S. B.;

Higgins, J. B.; Schlenker, J. L. *J. Am. Chem. Soc.* **1992**, *114*, 10834. (c) Kresge, C. T.; Leonowicz, M. E.; Roth, W. J.; Vartuli, J. C. US Patent #5,098,684, 1992.

[5] For example, (a) Tanev, P. T.; Chibwe, M.; Pinnavaia, T. J. *Nature* **1994**, *368*, 321. (b) Rey, F.; Sankar, G.; Maschmeyer, T.; Thomas, J. M.; Bell, R. G.; Greaves, G. N. *Top. Catal.* **1996**, *3*, 121. (c) Tuel, A.; Gontier, S. *Chem. Mater.* **1996**, *8*, 114. (d) Zhang, L.; Ying, J. Y. *AIChE J.* **1997**, *43*, 2793.

[6] (a) Mehnert, C. P.; Ying, J. Y. *Chem. Commun.* **1997**, 2215. (b) Mehnert, C. P.; Weaver, D. W.; Ying, J. Y. *J. Am. Chem. Soc.* **1998**, *20*, 12289.

[7] Yonemitsu, M.; Tanaka, Y.; Iwamoto, M. *Chem. Mater.* **1997**, *9*, 2679.

[8] (a) Maschmeyer, T.; Rey, F.; Sankar, G.; Thomas, J. M. *Nature* **1995**, *378*, 159. (b) Burch, R.; Cruise, N. A.; Gleeson, D.; Tsang, S. C. *J. Mater. Chem.* **1998**, *8*, 227.

[9] (a) Aronson, B. J.; Blanford, C. F.; Stein, A. *Chem. Mater.* **1997**, *9*, 2842. (b) Blasco, T.; Corma, A.; Martínez, A.; Martínez-Escolano, P. *J. Catal.* **1998**, *177*, 306. (b) Mulukutla, R. S.; Asakura, K.; Namba, S.; Iwasawa, Y. *Chem. Commun.* **1998**, 1425.

[10] (a) Díaz, J. F.; Balkus, Jr., K. J.; Bedioui, F.; Kurshev, V.; Kevan, L. *Chem. Mater.* **1997**, *9*, 61. (b) Lim, M. H.; Blanford, C. F.; Stein, A. *Chem. Mater.* **1998**, *10*, 467. (c) Moller, K.; Bein, T. *Chem. Mater.* **1998**, *10*, 2950. (d) Zhang L., Sun T., Ying J. Y. *Chem. Commun.* **1999**, 1103.

[11] (a) Tanabe, K.; Sumiyoshi, T.; Shibata, K.; Kiyoura, T.; Kitagawa, J. *Bull. Chem. Soc. Jpn.* **1974**, *47*, 1064. (b) Tanabe, K.; Misono, M.; Ono, Y.; Hattori, H. *New Solid Acids and Bases: Their Catalytic Properties*; Kodansha: Tokyo, 1989. (c) Kung, H. H. *J. Solid St. Chem.* **1984**, *52*, 191.

[12] Shibata, K.; Kiyoura, T.; Kitagawa, J.; Sumiyoshi, T.; Tanabe, K. *Bull. Chem. Soc. Jpn.* **1973**, *46*, 2985.

[13] (a) Soled, S.; McVicker, G. B. *Catal. Today* **1992**, *14*, 189. (b) Bosman, H. J. M.; Kruissink, E. C.; van der Spoel, J.; van den Brink, F. *J. Catal.* **1994**, *148*, 660. (c) Contescu, C.; Popa, V. T.; Miller, J. B.; Ko, E. I.; Schwarz, J. A. *J. Catal.* **1995**, *157*, 244.

[14] (a) Miller, J. B.; Rankin, S. E.; Ko, E. I. *J. Catal.* **1994**, *148*, 673. (b) Miller, J. B.; Ko, E. I. *J. Catal.* **1996**, *159*, 58.

[15] (a) Sohn, J. R.; Jang, H. J. *J. Molec. Catal.* **1991**, *64*, 349. (b) Miller, J. B.; Ko, E. I. *Chem. Eng. J.* **1996**, *64*, 273. (c) Navío, J. A.; Colón, G.; Macías, M.; Campelo, J. M.; Romero, A. A.; Marinas, J. M. *J. Catal.* **1996**, *161*, 605.

[16] (a) Rocha, J.; Ferreira, P.; Lin, Z.; Agger, J. R.; Anderson, M. W. *Chem. Commun.* **1998**, 1269. (b) Jale, S. R.; Ojo, A.; Fitch, F. R. *Chem. Commun.* **1999**, 411. (c) Rakshe, B.; Ramaswamy, V.; Hegde, S. G.; Vetrivel, R.; Ramaswamy, A. V. *Catal. Lett.* **1997**, *45*, 41.

[17] (a) Notari, B. *Adv. Catal.* **1996**, *41*, 253. (b) Arends, I. W. C. E.; Sheldon, R. A.; Wallau, M.; Schuchardt, U. *Angew. Chem. Int. Ed. Engl.* **1997**, *36*, 1144.

[18] Jones, D. J.; Jiménez-Jiménez, J.; Jiménez-López, A.; Maireles-Torres, P.; Olivera-Pastor, P.; Rodriguez-Castellón, E.; Rozière, J. *Chem. Commun.* **1997**, 431.

[19] (a) Tuel, A.; Gontier, S.; Teissier, R. *Chem. Commun.* **1996**, 651. (b) Gontier, S.; Tuel, A. *Appl. Catal. A* **1996**,*143*, 125.

[20] Occelli, M. L.; Biz, S.; Auroux, A. *Appl. Catal. A: Gen.* **1999**, *183*, 231.

[21] (a) Huo, Q.; Margolese, D. I.; Ciesla, U.; Feng, P.; Gier, T. E.; Sieger, P.; Leon, R.; Petroff, P. M.; Schüth, F.; Stucky, G. D. *Nature* **1994**, *368*, 317. (b) Huo, Q.; Margolese, D. I.; Ciesla, U.; Demuth, D. G.; Feng, P.; Gier, T. E.; Sieger, P.; Firouzi, A.; Chmelka, B. F.; Schüth, F.; Stucky, G. D. *Chem. Mater.* **1994**, *6*, 1176.

[22] Zhang, W.; Wang, J., Tanev, P. T.; Pinnavaia, T. J. *Chem. Commun.* **1996**, 979.

[23] (a) Zhao, D.; Feng, J.; Huo, Q.; Melosh, N.; Fredrickson, G. H.; Chmelka, B. F.; Stucky. G. D. *Science* **1998**, *279*, 548. (b) Zhao, D.; Huo, Q.; Feng, J.; Chmelka, B. F.; Stucky, G. D. *J. Am. Chem. Soc.* **1998**, *120*, 6024.

[24] (a) Gregg, S. K.; Sing, K. S. W. *Adsorption, Surface Area and Porosity*, 2nd Ed.; Academic Press: London, 1982. (b) Webb, P. A.; Orr, C. *Analytical Methods in Fine Particle Technology*; Micromeritics Instrument Co.: Norcross, 1997.

[25] Horváth, G; Kawazoe, K. *J. Chem. Eng. Jpn.* **1983**, *16*, 470.

[26] McClelland, J. F.; Jones, R. W.; Luo, S.; Seaverson, L. M. in *Practical Sampling Techniques for Infrared Analysis*; Coleman, P. B., Ed.; CRC Press: Boca Raton, 1993, p. 107.

[27] Delgass, W. N.; Haller, G. L.; Kellerman, R.; Lunsford, J. H. *Spectroscopy in Heterogeneous Catalysis*; Academic Press: New York, 1979.

[28] Cotton, F. A.; Wilkinson, G. *Advanced Inorganic Chemistry: A Comprehensive Text*, 5th Ed.; John Wiley: New York, 1988.

[29] Clearfield, A.; Serrette, G. P. D.; Khazi-Syed, A. H. *Catal. Today* **1994**, *20*, 295.

[30] (a) Song, X.; Sayari, A. *Catal. Rev.-Sci. Eng.* **1996**, *38*, 329. (b) Cheung, T.-K.; Gates, B. C. *Chemtech*; September, 1997, 28.

[31] Shannon, R. D.; Prewitt, C. T. *Acta Cryst.* **1969**, *B25*, 925.

[32] (a) Chen, C.-Y.; Xiao, S.-Q.; Davis, M. E. *Micropor. Mater.* **1995**, *4*, 1. (b) Schacht, S.; Janicke, M.; Schüth, F. *Micropor. Mesopor. Mater.* **1998**, *22*, 485.

[33] Sonwane, C. G.; Bhatia, S. K.; Calos, N., *Ind. Eng. Chem. Res.* **1998**, *37*, 2271.

[34] Inoue, S.; Hanzawa, Y.; Kaneko, K. *Langmuir* **1998**, *14*, 3079.

[35] (a) Ciesla, U.; Schacht, S.; Stucky, G. D.; Unger, K. K.; Schüth, F. *Angew. Chem. Int. Ed. Engl.* **1996**, *35*, 541. (b) Ciesla, U.; Fröba, M.; Stucky, G.; Schüth, F. *Chem. Mater.* **1999**, 11, 227.

[36] Wong, M. S.; Ying, J. Y. *Chem. Mater.* **1998**, *10*, 2067.

[37] Sun, T.; Ying, J. Y. *Nature* **1997**, *389*, 704.

[38] Ying, J. Y.; Benziger, J. B.; Navrotsky, A. *J. Am. Ceram. Soc.* **1993**, *76*, 2571.

[39] Lee, S. W.; Condrate, Sr., R. A. *J. Mater. Sci.* **1988**, *23*, 2951.

[40] Debsikdar, J. C. *J. Non-Cryst. Solids* **1986**, *87*, 343.

[41] Burneau, A.; Gallas, J.-P., in *The Surface Properties of Silicas*; Legrand, A. P., Ed.; John Wiley and Sons: Chichester, 1998, p. 147.

[42] Chen, J.; Li, Q.; Xu, R.; Xiao, F. *Angew. Chem. Int. Ed. Engl.* **1995**, 34, 2694.

[43] Morey, M. S.; Stucky, G. D.; Schwarz, S.; Fröba, M. *J. Phys. Chem. B* **1999**, *103*, 2037.

[44] Schoonheydt, R. A. in *Characterization of Heterogeneous Catalysts*; Delannay, F., Ed.; Marcel Dekker: New York, 1984, p. 125.

[45] (a) Moon, S.-C.; Fujino, M.; Yamashita, H.; Anpo, M. *J. Phys. Chem. B* **1997**, *101*, 369. (b) Gao, X.; Fierro, J. L. G.; Wachs, I. E. *Langmuir* **1999**, *15*, 3169.

[46] Engelhardt, G.; Koller, H. in *Solid-State NMR II – Inorganic Matter*; Blumich, B., Ed.; Springer-Verlag: Berlin, 1994, p. 1.

[47] Zhao, X. S.; Lu, G. Q.; Whittaker, A. K.; Millar, G. J.; Zhu, H. Y. *J. Phys. Chem. B* **1997**, *101*, 6525.

[48] Steel, A.; Carr, S. W.; Anderson, M. W. *Chem. Mater.* **1995**, *7*, 1829.

[49] Terry, K. W.; Lugmair, C. G.; Tilley, T. D. *J. Am. Chem. Soc.* **1997**, *119*, 9745.

[50] Andrianainarivelo, M.; Corriu, R.; Leclercq, D.; Mutin, P. H.; Vioux, A. *J. Mater. Chem.* **1996**, *6*, 1665.

[51] Mokaya, R.; Jones, W. *Chem. Commun.* **1996**, 981.

[52] Tanev, P. T.; Pinnavaia, T. J. *Science* **1995**, *267*, 865.

[53] Schacht, S.; Huo, Q.; Voigt-Martin, I. G.; Stucky, G. D.; Schüth, F. *Science* **1996**, *273*, 768.

[54] Aguayo, A. T.; Arandes, J. M.; Olazar, M.; Bilbao, J. *Ind. Eng. Chem. Res.* **1990**, *29*, 1172.

[55] Liu, Z.; Tabora, J.; Davis, R. J. *J. Catal.* **1994**, *149*, 117.

[56] Mastikhin, V. M.; Nosov, A. V.; Terskikh, V. V.; Zamaraev, K. I.; Wachs, I. E. *J. Phys. Chem.* **1994**, *98*, 13621.

[57] Bergna, H. E., in *The Colloid Chemistry of Silica,* Advances in Chemistry Series, Vol. 234; Bergna, H. E., Ed.; American Chemical Society: Washington, DC, 1994, p. 1.

[58] (a) Butler, A. C.; Nicolaides; C. P. *Catal. Today* **1993**, *18*, 443. (b) Houzvicka, J.; Ponec, V. *Catal. Rev.-Sci. Eng.* **1997**, *39*, 319.

[59] (a) Xu, W.-Q.; Yin, Y.-G.; Suib, S. L.; O'Young, C.-L. *J. Catal.* **1994**, *150*, 34. (b) Woo, H. C.; Lee, K. H.; Lee, J. S. *Appl. Catal., A* **1996**, *134*, 147.

[60] Gayubo, A. G.; Llorens, F. J.; Cepeda, E. A. Bilbao, J. *Ind. Eng. Chem. Res.* **1997**, *36*, 5189.

[61] Gielgens, L. H.; van Kampen, M. G. H.; Broek, M. M.; van Hardeveld, R.; Ponec, V. *J. Catal.* **1995**, *154*, 201.

[62] Rudolph, J.; Reddy, K. L.; Chiang, J. P.; Sharpless, K. B. *J. Am. Chem. Soc.* **1997**, *119*, 6189.

[63] Sheldon, R. A.; Wallau, M.; Arends, I. W. C. E.; Schuchardt, U. *Acc. Chem. Res.* **1998**, *31*, 485.

[64] Satterfield, C. N., *Heterogeneous Catalysis in Industrial Practice*, 2nd Ed.; McGraw-Hill: New York, 1991.

[65] Satterfield, C. N., *Mass Transfer in Heterogeneous Catalysis*; Krieger Publishing: New York, 1981.

Chapter 4. Mesoporous Tungstated Zirconia

4.1 Introduction

Over the past few years, the compositional range of mesoporous materials has expanded from pure and doped silicates to pure non-silicate metal oxides and mixed metal oxides through various novel synthetic schemes. Mesoporous (and microporous) non-silicates can be derived via careful manipulation of supramolecular templating chemistry [1-7]. The difficulties in preparing mesoporous non-silicates have been attributed to (i) the propensity of the amorphous metal oxide walls to crystallize into denser phases, (ii) the prevalence of themally unstable lamellar phases, (iii) the insufficient wall thickness for self-support, and (iv) the incomplete condensation and strengthening of the metal oxide framework [1-8]. In comparison, mesoporous silica can maintain framework integrity to temperatures above 800 °C [9]. Pinnavaia and co-workers reported on a disordered form of mesoporous silica that was stable at 1000 °C, which they attributed to the highly crosslinked SiO_4 units in the pore walls [10].

Different approaches have been used to strengthen non-silicate pore walls. Stein *et al.* prepared surfactant-templated mesostructures in which the walls were composed of unconnected metatungstate anions ($H_2W_{12}O_{40}^{6-}$) [4]. To promote connectivity among the anions and to create a porous material, they replaced the metatungstate anions with niobotungstate anions and reacted the former with tetraethylorthosilicate to create Nb-O-Si linkages. In another case, mesoporous zirconia-based materials have been prepared by utilizing surface species such as phosphates and sulfates [5-6]. These species bind onto the oxide surface, strengthening the pore walls. A variation of supramolecular templating involving a "scaffolding" mechanism led to a pure mesoporous zirconia material [11]. A generalized supramolecular templating approach to mesoporous non-silicates was developed by Yang *et al.* [3]. A metal chloride was dissolved in an ethanol solution of a triblock copolymer surfactant, and allowed to hydrolyze and condense into a gel. The recovered gel was mesostructured, and could be calcined at 400 °C for surfactant removal to produce the mesoporous structure. Thermal stability of these non-silicates was attributed to the pore walls being thick and partially crystalline.

The use of inorganic colloids has been studied as an alternative method for deriving porous materials for catalyst supports. Ko and co-workers investigated the preparation of

porous zirconia using colloidal sols [12]. Murrell reviewed several metal oxide and mixed metal oxide systems prepared from sols, or colloidal oxides [13]. Elder *et al.* reported the preparation of a surfactant-templated mesoporous mixed metal oxide containing zirconia and nanocrystals of titania. They inferred that the titania crystallized from the salt precursor during the synthesis [14].

In this Chapter, we present a new method for creating thermally stable mesoporous non-silicate metal oxides using pre-formed inorganic colloid particles to form the framework walls. Triblock copolymer surfactants were used to template the zirconia colloid particles, and a tungstate salt was introduced to bind the colloid particles together. The colloid form of the inorganic provided excellent thermal stability for the framework. A colloid/surfactant templating mechanism of formation based on favorable charge and hydrogen-bonding interactions between the colloid particles, surfactant, and tungstate salt is hypothesized.

4.2 Experimental Methods

4.2.1 Synthesis

In a typical synthesis of mesoporous tungstated zirconia designated WZr-TMS14, 14.3 g of a surfactant solution of 5.7 wt% Pluronic® P123 (MW ~ 5750, BASF [15]) were used. P123 is a non-ionic poly(ethylene oxide)-poly(propylene oxide)-poly(ethylene oxide) triblock copolymer with the structural formula $EO_{20}PO_{70}EO_{20}$. 0.81 g of ammonium metatungstate ($(NH_4)_6H_2W_{12}O_{40}$ or "AWO", Strem) was then added to the aqueous surfactant solution. While the resulting clear solution was being stirred, 8.1 g of an acidic 20 wt% zirconium oxide colloid solution (Nyacol® Zr10/20, nominal particle size = 5-10 nm, pH = 0.5, PQ Corp.) were quickly added, and immediate precipitation resulted. The final weight ratio of the synthesis mixture was 1.0 ZrO_2 : 0.5 AWO : 0.5 P123 : 11.9 H_2O, and the final pH is ~0.5. After stirring for 2 hr, the mixture was left to age for 2 days at room temperature. A white precipitate was recovered through washing with water and centrifuging, followed by decanting the supernatant; this procedure was repeated for three times. The collected material was left to dry in air overnight, and then ground into a fine powder. The white powder was calcined under flowing air in a quartz tube to 600 °C with a ramp rate of 3.2 °C/min and soaked for 3 hr. The same ramp rate was used for calcination to other temperatures.

Other zirconium oxide precursors were used to form the framework: colloidal zirconium oxide with a nominal particle size of 50 nm (Nyacol Zr50/20, pH = 0.5, PQ Corp.), zirconyl nitrate (Aldrich, ~35 wt% $ZrO(NO_3)_2$ solution), zirconyl chloride octahydrate (Aldrich), and zirconium chloride (Strem). The zirconium salts were introduced as 0.02 M solutions.

Pluronic triblock copolymer surfactants (BASF) of different chain lengths were also used as templating agents: L121 ($EO_5PO_{70}EO_5$; MW ~ 4400), F127 ($EO_{106}PO_{70}EO_{106}$; MW ~ 12600), P84 ($EO_{20}PO_{39}EO_{20}$; MW ~ 4200), F87 ($EO_{63}PO_{39}EO_{63}$; MW ~ 7700), and P103 ($EO_{17}PO_{60}EO_{17}$; MW ~ 4950). Latex nanospheres were also used as a templating agent in the synthesis of WZr-TMS15. A 1-wt% polymer solution was prepared through the radical-initiated polymerization of methylmethacrylate/methyl acrylate (Aldrich) within F87 (BASF) surfactant micelles. The nanospheres were determined to be ~15 nm in diameter, according to dynamic light scattering. The same weight of templating agent was used for all syntheses in this study.

4.2.2 Characterization

Powder X-ray diffraction (XRD) data were collected on a Siemens D5000 θ-θ diffractometer (45 kV, 40 mA) using nickel-filtered CuK_α radiation with wavelength λ = 1.5406 Å. Diffraction patterns were obtained at ambient conditions for 2θ = 20.0° to 60.0° with a resolution of 0.04°.

Small-angle X-ray scattering (SAXS) patterns were collected on a Siemens small-angle diffractometer with a Siemens HI-STAR area detector, operating at 40 kV and 30 mA (λ = 1.5406 Å). Bragg spacing values were calculated from the peak maximum using Bragg's Law: $d = \lambda/(2\sin\theta)$.

In situ variable-temperature XRD (VT-XRD) data were obtained with a Rigaku diffractometer with a rotating Cu anode. The sample was secured onto a platinum grid and placed in a sealed high-temperature stage. The heating profile consisted of ramping at 10 °C/min to the desired temperature and soaking for 10 minutes before the measurement was taken isothermally.

Transmission electron micrographs (TEM) were taken on a JEOL 2000FX transmission electron microscope equipped with a lanthanum hexaboride (LaB_6) gun

operating at an accelerating voltage of 200 kV and with an objective aperture of 50 μm. Samples for TEM studies were ground, dispersed in isopropanol, and applied onto a carbon-coated copper grid (200 mesh). High-resolution TEM (HRTEM) images were obtained with a JEOL 2010 transmission electron microscope equipped with a LaB_6 gun, operating at 200 kV. WZr-TMS14 calcined at 600 °C was embedded in acrylic resin and ultramicrotomed into thin sections for analysis. A sample of colloidal zirconium oxide was prepared by diluting with water before drying onto the carbon-coated copper grid. Selected-area electron diffraction (SAED) patterns were collected using a selected-area aperture of 20 μm and at a camera length L of 100 cm. The d-spacings of the diffraction rings were measured using the relation $d = L/R\lambda$, where R is the radial distance measured and λ is the de Broglie wavelength of 0.02507 Å. Oxford Instruments Link ISIS Microanalysis System electron dispersive spectrometer (EDS) allowed determination of elemental composition. Bulk elemental analysis was performed by QTI (Whitehouse, NJ).

Nitrogen adsorption isotherms were obtained at 77 K on a Micromeritics ASAP 2010 Gas Sorption and Porosimetry System. Samples were degassed at 150 °C under vacuum for at least 6 hr until a final pressure of 1×10^{-3} Torr was reached. BET surface areas were determined over a P/P_0 range of 0.05-0.20. Mesopore size distributions were calculated from the adsorption branch of the isotherms using the BJH method.

Thermogravimetric analysis (TGA) and differential thermal analysis (DTA) were performed on a Perkin-Elmer Series 7 Thermal Analysis System. Platinum sample holders were used for both types of experiments. A ramp rate of 5 °C/min was used with purified air as the flowing purge gas (~60 sccm). Samples used for DTA studies were (i) colloidal zirconium oxide dried at 90 °C, (ii) hydrous zirconium oxide precipitated from a zirconyl chloride solution with ammonium hydroxide, and (iii) hydrous tungsten oxide precipitated from an ammonium metatungstate solution with ammonium hydroxide and calcined at 350 °C. All three samples were amorphous by XRD. α-Al_2O_3 was used as the reference sample for the DTA studies.

Diffuse reflectance infrared Fourier-transform (DRIFT) spectroscopy with pyridine adsorption was performed on a Bio-Rad FTS-60A/896 spectrometer using a Harrick DRS-1 Praying Mantis diffuse reflectance attachment. The heated sample cell was sealed from the atmosphere with a dome containing CdTe optical windows. Helium gas flow (99.999+%)

was introduced into the cell while the sample was pretreated to 500 °C, before contacting with pyridine-saturated helium gas at 150 °C. DRIFT spectra were collected at a scan speed of 5 kHz for wavenumbers of 400 to 4000 cm^{-1} with a resolution of 2 cm^{-1}.

Raman spectra were obtained with the 514.5-nm line of an Ar^{+} ion laser operating at 50 mW (Spectra Physics, Model 164). The samples were pressed into self-supporting wafers, and spectra were collected under ambient conditions. Used as standard samples were tungsten oxide prepared from the calcination of tungstic acid, and tetragonal zirconia prepared from the calcination of the 90 °C-dried zirconia colloid precursor at 450 °C. A second laser Raman spectrometer was used to collect spectra under *in situ* dehydrated conditions, i.e. flowing oxygen at 550 °C. Details of the Raman spectrometer set-up can be found elsewhere [16].

Diffuse reflectance ultraviolet-visible (UV-Vis) experiments were conducted on Varian Cary 5E UV-Vis-NIR spectrophotometer with an integration sphere diffuse reflectance attachment. Most powdered samples were secured onto a glass slide using Collodion (Fisher Scientific); Collodion was found to absorb below 250 nm, with no interference with the region of interest (350-500 nm). WZr-TMS14 calcined at 600 °C was pressed into a self-supporting pellet for analysis. A halon white (polytetrafluoroethylene) reflectance standard was used as the baseline. The Kubelka-Munk formalism $F(R_\infty)=(1-R_\infty)^2/(2R_\infty)$ was used, where R_∞ is the reflectance at infinite thickness [17]. The optical absorption edge energy for indirectly-allowed electronic transitions, or indirect band gap energy E_g, was determined by finding the x-intercept of the straight line in the low energy rise of a plot of $[F(R_\infty)\times h\nu]^{1/2}$ against $h\nu$, where $h\nu$ is the incident photon energy. Tungsten oxide is known to exhibit indirect electronic transitions, thus validating this particular form of the absorption edge energy relation [18].

Surface composition analysis was carried out with X-ray photoelectron spectroscopy (XPS) on a Surface Science ESCA spectrometer (Model SSX-100) equipped with a monochromatic AlK_α radiation source.

WZr-TMS14 was studied for the gas-phase acid-catalyzed isomerization of 1-butene. The reaction conditions were similar to those used in the ZrSi catalytic studies (Section 3.2.3), except that 50 mg of powder and a weight-hourly space velocity (WHSV) of 3 hr^{-1} were used. Also, a HP 5890 Series II gas chromatograph (GC) connected to Peak2 data acquisition

system was used. Commercial sulfated zirconia (MEI) calcined at 600 °C was employed as a reference catalyst.

4.3 Results

Zirconium oxide nanoparticles in the form of a colloid solution were used to prepare mesoporous tungstated zirconia, WZr-TMS14. The 20 wt% ZrO_2 colloid solution was transparent, giving no indication of particle coagulation; it was stabilized by the nitrate anions from the 10 wt% nitric acid in the solution. The zirconia colloid particles in Zr10/20 were nominally 5-10 nm in diameter, according to the commercial supplier. The roughly spherical particles were found to be 5 nm in size, in our HRTEM studies (Figure 4.1(a) and inset). They particles were crystalline, as illustrated by the lattice fringes in the HRTEM image and by the SAED pattern (Figure 4.1(b)). The rings in the SAED pattern were indexed to cubic zirconia (JCPDS #27-0997) (Table 4.1). The solid recovered from the evaporated zirconia

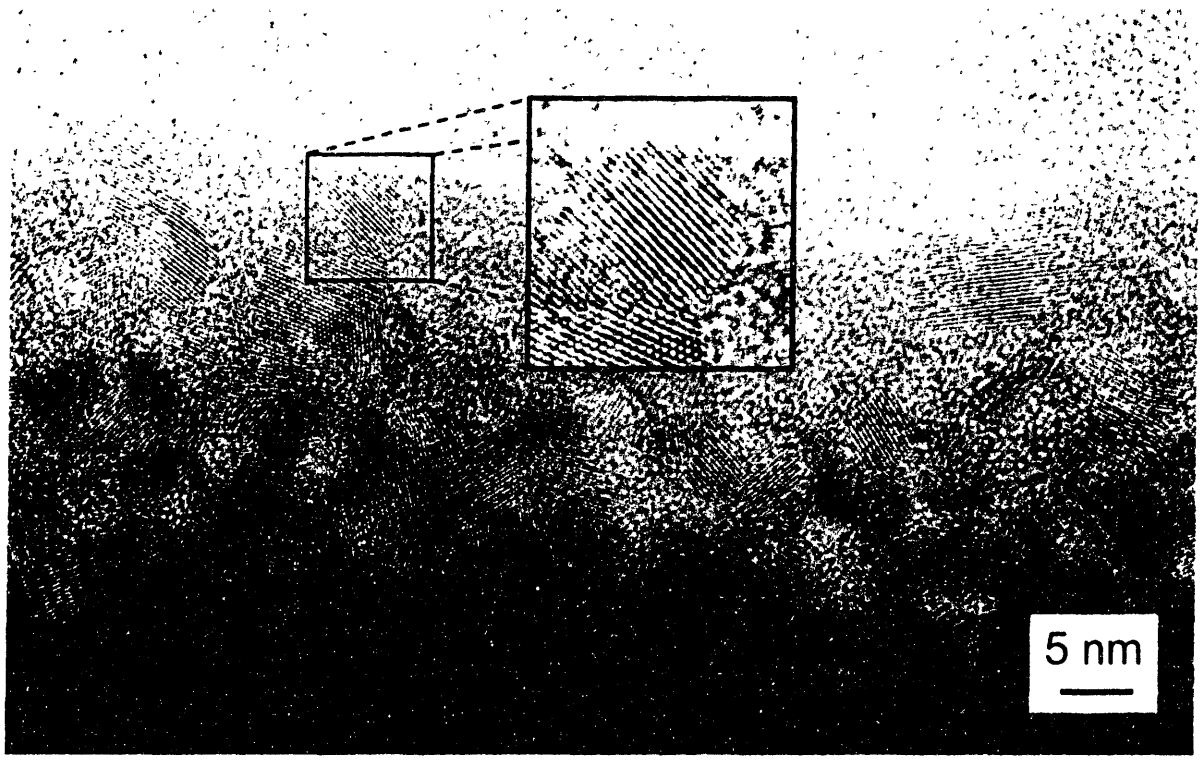

Figure 4.1. (a) High-resolution transmission electron microscopy (HRTEM) image of dried zirconia colloid particles. Inset shows an expanded image (2×) of a colloid particle.

colloid solution showed very broad bands in the XRD studies, possibly due to its ultrafine grain size (Figure 4.1(c)).

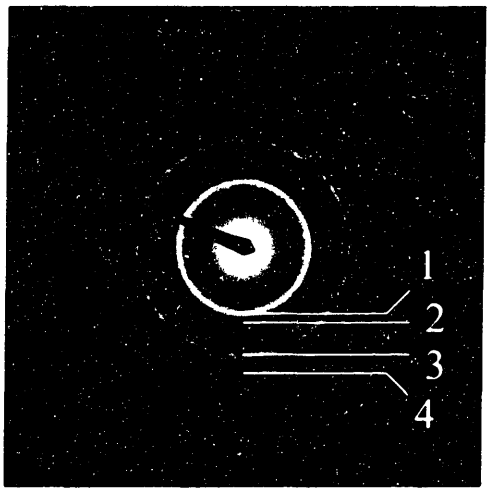

Figure 4.1. (b) SAED pattern of the dried zirconia colloid particles.

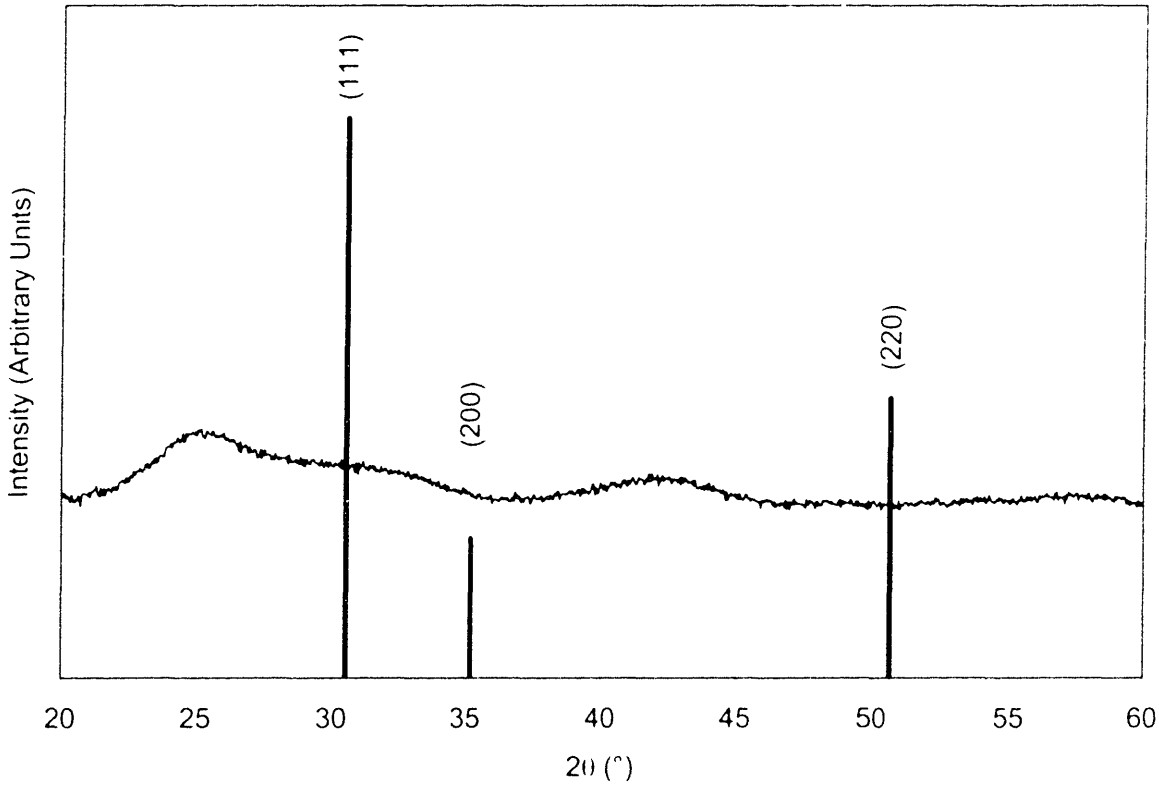

Figure 4.1. (c) XRD pattern of the dried zirconia colloid particles. Lines represent positions of the XRD peaks expected for cubic zirconia phase.

Table 4.1. Interplanar spacings determined from the by SAED pattern of the dried zirconia colloid particles.

Ring	*d*-Spacing (Å)	Cubic Phase
1	2.95	(111)
2	2.57	(200)
3	1.79	(220)
4	1.54	(311)

The supramolecular-templated WZr-TMS14 has a highly porous structure after calcination at 600 °C, as illustrated in Figure 4.2(a). The unevenly-shaped pores appeared to be interconnected and to have a wormlike characteristic, suggesting that the material was comprised of a fully connected pore network. The mesoporosity was also evidenced by the Type IV nitrogen adsorption isotherm (Figure 4.3(a)). The pore openings were found to be 3-6 nm in diameter by HRTEM and from the BJH pore size distribution (Figure 4.3(b)). A BET surface area of 130 m^2/g was determined by nitrogen adsorption analysis.

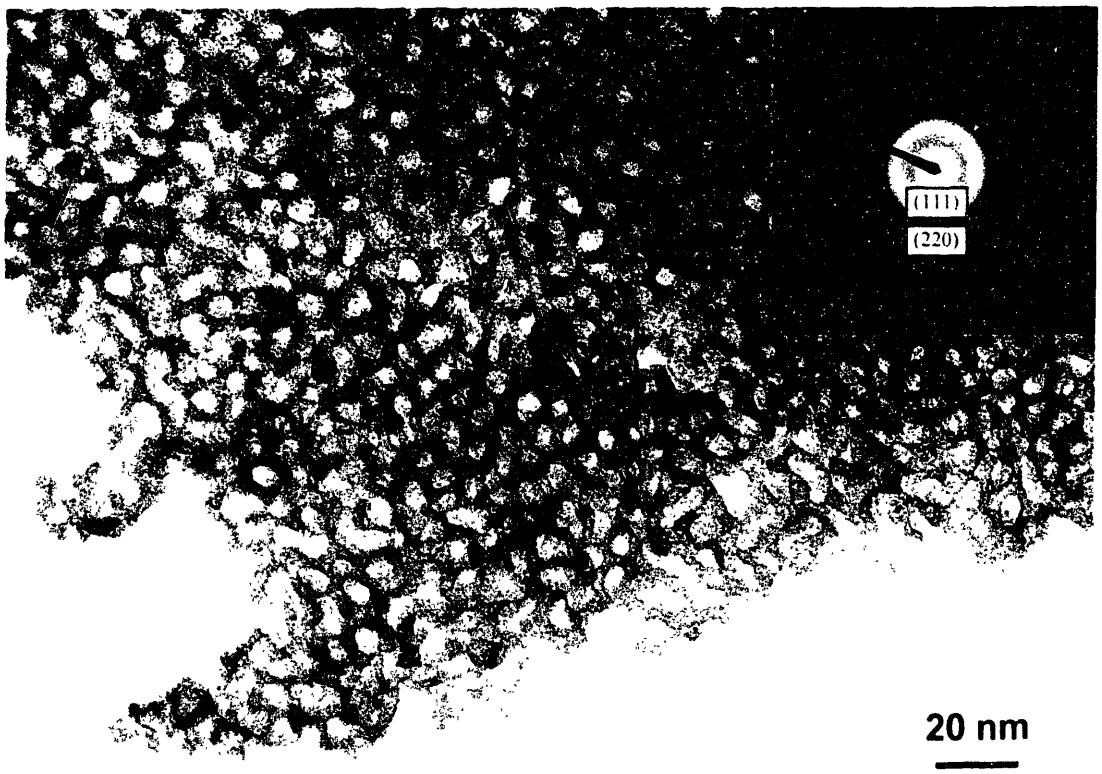

Figure 4.2. (a) TEM image of an ultramicrotomed section of WZr-TMS14 calcined at 600 °C. Inset shows the SAED pattern of WZr-TMS14.

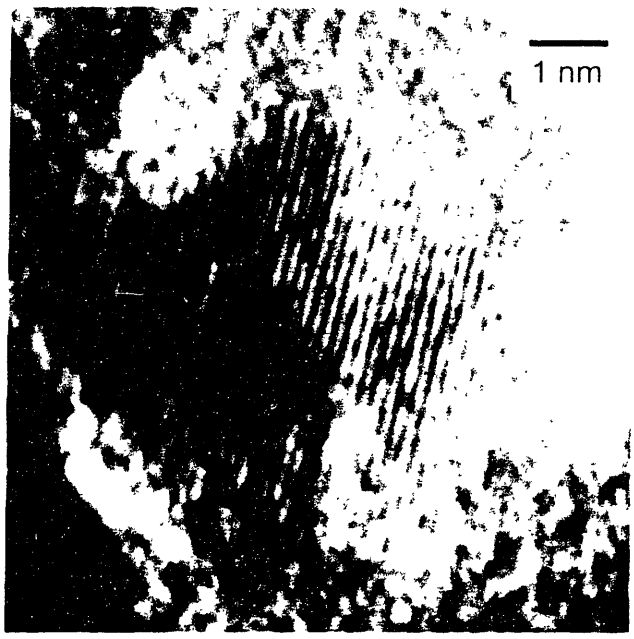

Figure 4.2. (b) HRTEM image of a zirconia grain in the framework of calcined WZr-TMS14.

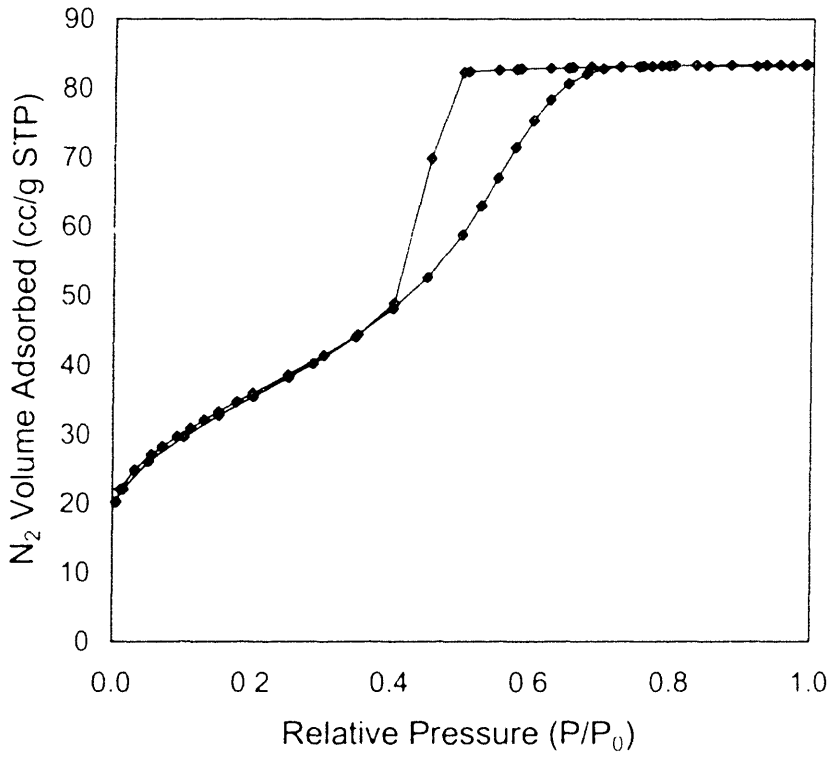

Figure 4.3. (a) Nitrogen adsorption isotherm of WZr-TMS14 calcined at 600 °C.

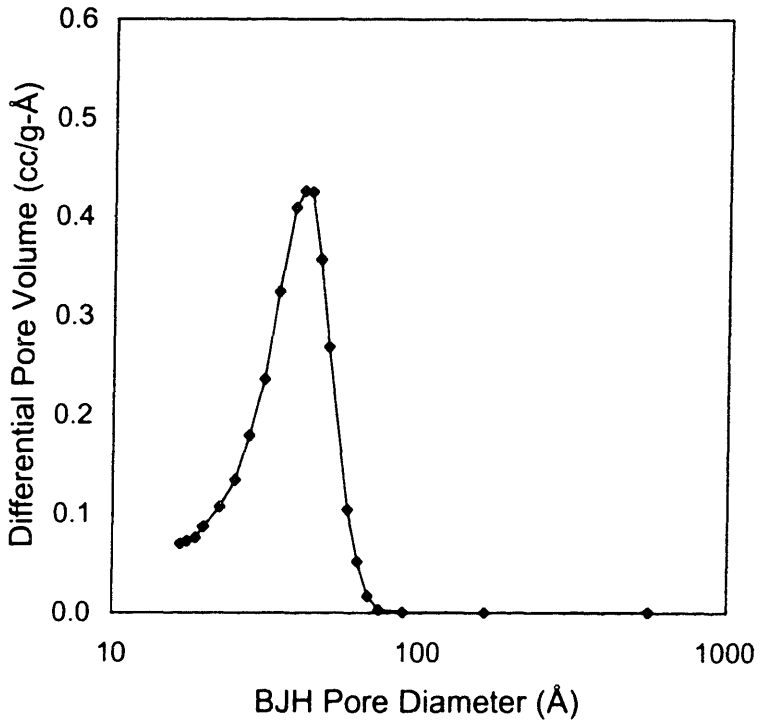

Figure 4.3. (b) BJH pore size distribution of WZr-TMS14 calcined at 600 °C.

Polymer surfactants of different chain lengths can be used (Table 4.2). Some dependence of the surfactants on the molecular weight and hydrophile-lypophile balance (HLB) values is noted in WZr-TMS14 materials, which have high surface areas and a narrow pore size distribution. Templating was not successful with surfactant molecules with molecular weights ≥ 7700 and HLB values ≥ 22. Much larger mesopores (15.0 nm) were formed by using the polymer nanospheres as the templating agent.

Table 4.2. Surface areas and pore sizes of WZr-TMS14 prepared with different templates.

Template used		Average MW (g/mol)	HLB	BET Surface Area (m^2/g)	Average Pore Size (nm)
$EO_5PO_{70}EO_5$	(L121)	4400	1	109	6.5
$EO_{20}PO_{70}EO_{20}$	(P123)	5750	8	130	4.0
$EO_{106}PO_{70}EO_{106}$	(F127)	12600	22	1	—
$EO_{17}PO_{60}EO_{17}$	(P103)	4950	9	59	3.5
$EO_{20}PO_{39}EO_{20}$	(P84)	4200	14	14	2.0
$EO_{63}PO_{39}EO_{63}$	(F87)	7700	24	3	—
Nanosphere (w/ F87)		—	—	127	15.0

The pore walls of WZr-TMS14 were measured to be 4-6 nm thick, suggesting that the walls can accommodate a single layer of zirconia colloid particles. Such particles were observed as 5-nm grains within the inorganic framework. Figure 4.2(b) shows the (220) planes in a single grain of cubic zirconia. The parent colloid particles constituted the framework walls, as further evidenced by the similarity of the SAED pattern of WZr-TMS14 (inset of Figure 4.2(a)) to that of cubic zirconia (Figure 4.1(b)). The diffraction rings are much more diffuse in the former and contain faint diffraction spots.

WZr-TMS14 exhibits a single peak in its SAXS patterns before and after calcination at 600 °C (Figures 4.4(a)-(b)). The Bragg spacing of this peak for as-synthesized WZr-TMS14 decreased by about 25% from 11.5 nm to 8.6 nm after calcination at 600 °C. This peak disappeared after the material was calcined at 800 °C.

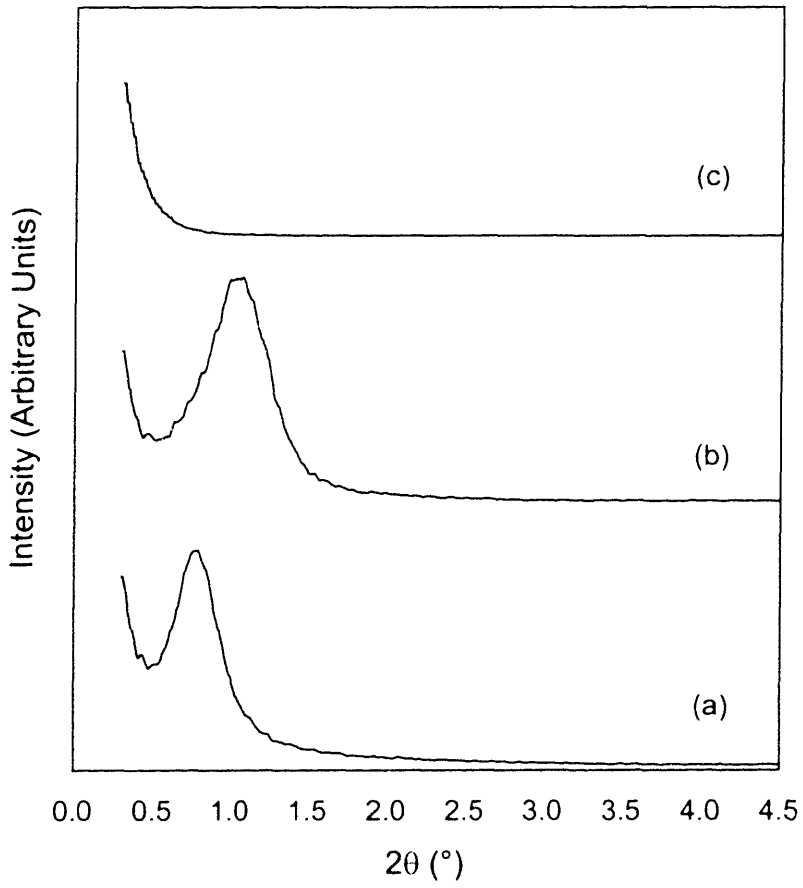

Figure 4.4. SAXS patterns of WZr-TMS14 prepared with zirconium oxide colloid precursor: (a) as-synthesized, (b) calcined at 600 °C, and (c) calcined at 800 °C.

WZr-TMS14 did not exhibit any XRD peaks before and after calcination at 600 °C (Figures 4.5(a)-(b)). Peaks corresponding to zirconium oxide and tungsten oxide phases emerged in the XRD pattern of the material calcined at 800 °C. Accompanying this change in structure between 600 °C and 800 °C were a reduction in surface area from 130 m^2/g to 23 m^2/g, and a color change from white to yellowish-green. The total amount of WO_3 in the framework of 600 °C-calcined WZr-TMS14 was determined to be 30.5 wt% by elemental analysis.

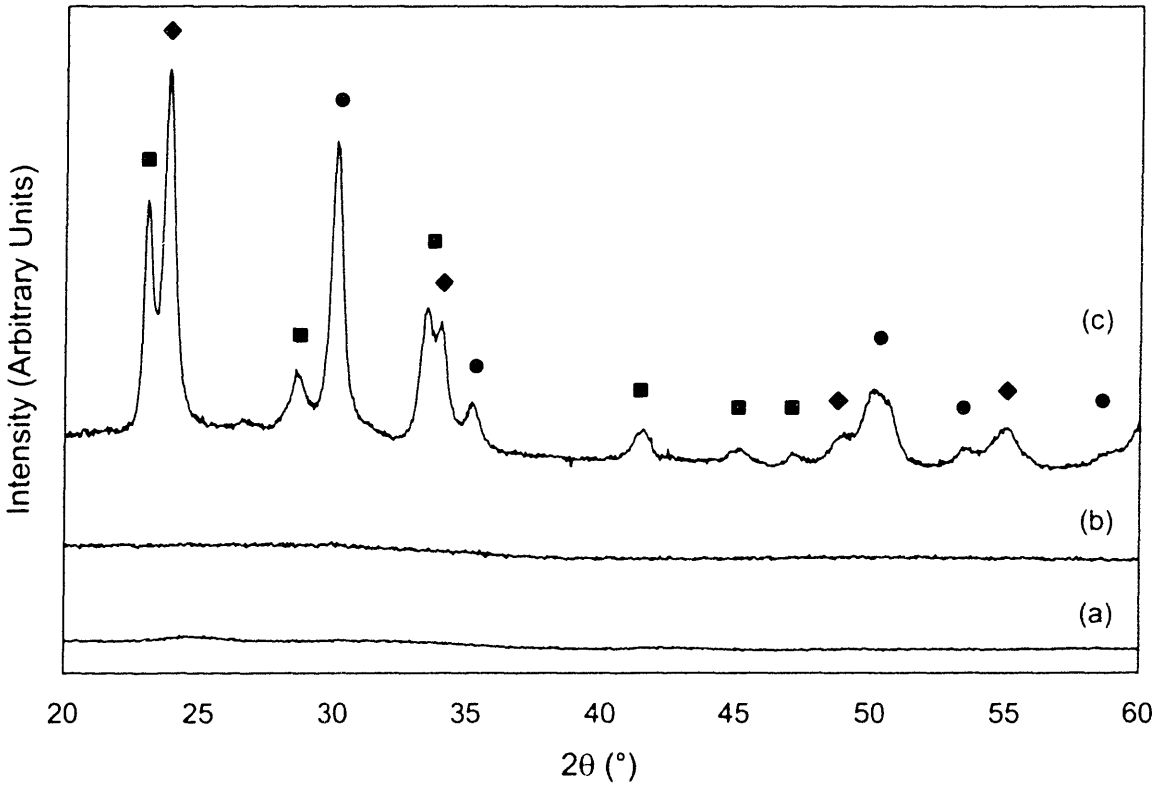

Figure 4.5. XRD patterns of WZr-TMS14 prepared with zirconium oxide colloid precursor: (a) as-synthesized, (b) calcined at 600 °C, and (c) calcined at 800 °C. ■ = orthorhombic WO_3 (#20-1324); ◆ = cubic WO_3 (#41-0905); ● = tetragonal ZrO_2 (#17-0923).

As-synthesized WZr-TMS14 lost 42.5% weight by 600 °C due to removal of the templating surfactant molecules, according to TGA results (Figure 4.6). The material experienced a further weight decrease of 1.2% at 800 °C. Concomitant with this weight loss was an exothermic peak centered at 715 °C in the DTA profile of WZr-TMS14 previously calcined at 600 °C (Figure 4.7(a)). This exothermic peak appeared at a significantly higher

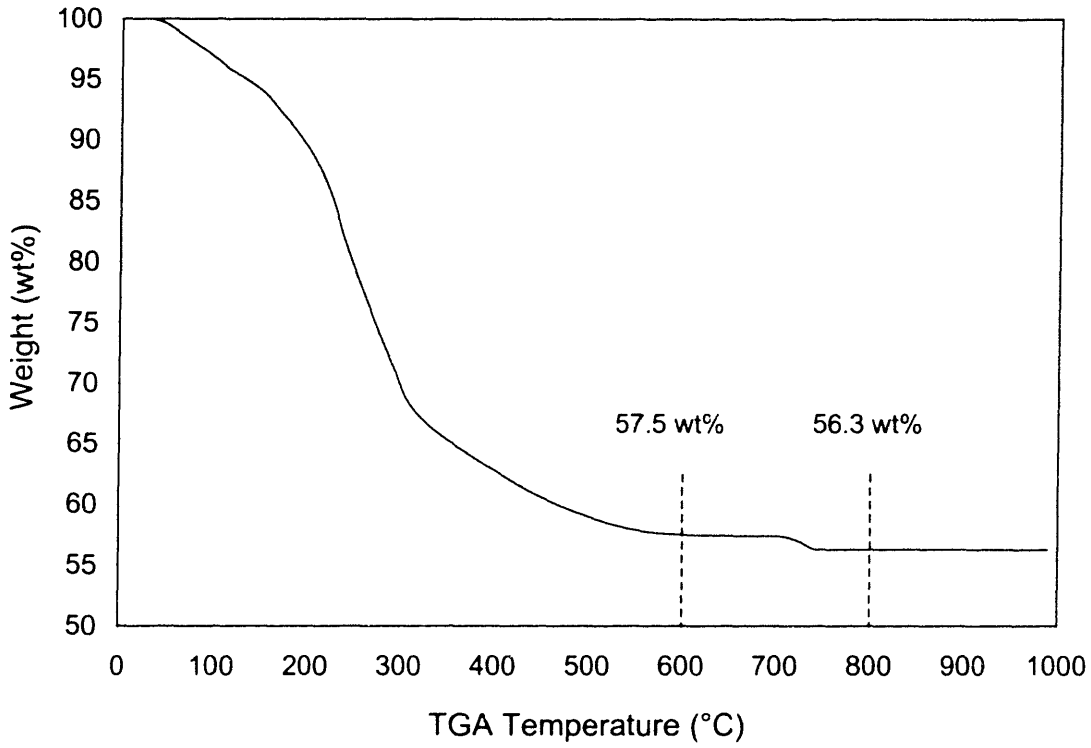

Figure 4.6. TGA profile of uncalcined WZr-TMS14. (Ramp rate = 5 °C/min, purge gas = air.)

temperature than those of dried zirconium oxide colloid particles (410-470 °C) (Figure 4.7(b)), hydrous zirconium oxide (428 °C) (Figure 4.7(c)), and tungsten hydroxide (390-460 °C) (Figure 4.7(d)).

The structural evolution of WZr-TMS14 was followed with *in situ* variable-temperature XRD (Figure 4.8). XRD peaks for tetragonal zirconia and tungsten oxides emerged at 650 °C, close to the crystallization temperature ascertained through DTA studies (715 °C). A number of substoichiometric tungsten oxides form easily from the reduction of WO_3 [19], but their overlapping XRD peaks are difficult to deconvolute.

The laser Raman spectrum of as-synthesized WZr-TMS14 exhibits bands at 1052, 1033, 986, 911, 863, 809, 760, 647, 544, 365, and 207 cm^{-1} (Figure 4.9). The bands at 1052 and 1033 cm^{-1} are found in the spectrum of the zirconia precursor, corresponding to residual nitrate anions [20]. The other bands are shifted slightly from those of the ammonium metatungstate precursor: 977, 966, 939, 887, 647, 529, 460, 351, and 217 cm^{-1}. Assignments for these Raman bands and for bands of isopolytungstate compounds, have been made: >900 cm^{-1} (W=O stretches), 900-800 cm^{-1} (symmetric O–W–O stretches), 600-400 cm^{-1} (symmetric

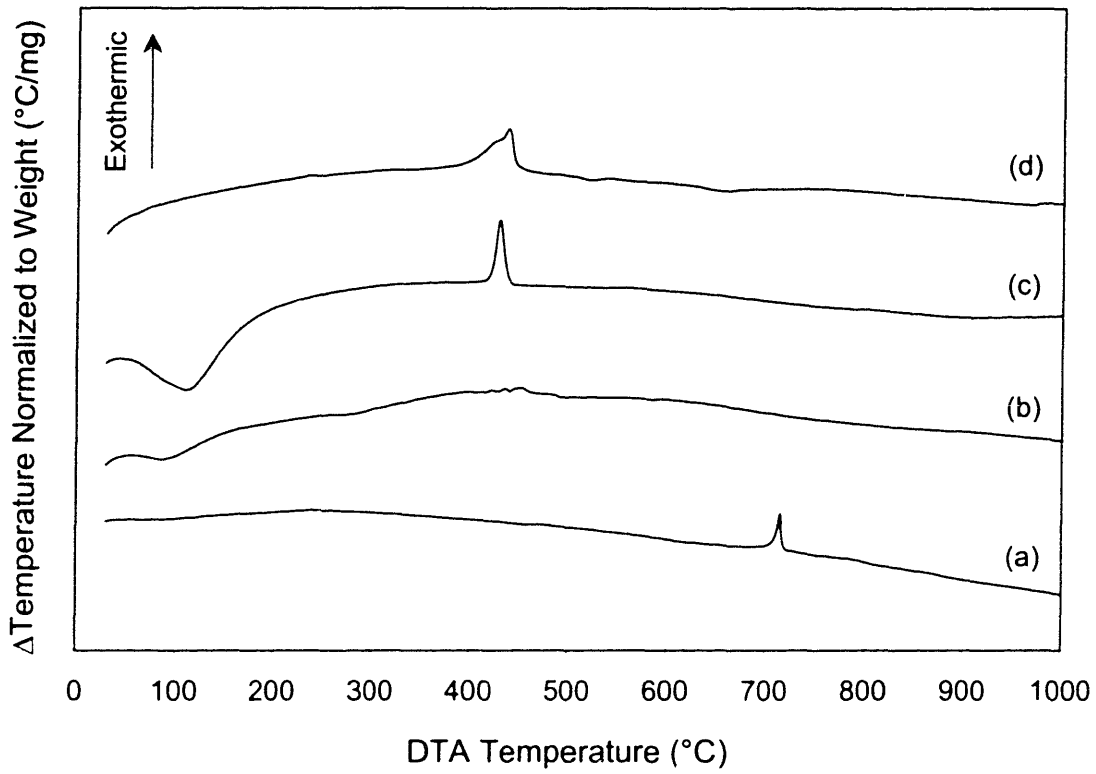

Figure 4.7. DTA profiles of (a) WZr-TMS14 calcined at 600 °C, (b) dried zirconia colloid particles, (c) hydrous zirconium oxide, and (d) hydrous tungsten oxide. (Ramp rate = 5 °C/min, purge gas = air.)

W–O–W stretches), and ~200 cm^{-1} (W–O–W bending modes) [21]. The Raman spectrum of as-synthesized WZr-TMS14 is a combination of those of ammonium metatungstate and of the zirconia colloid precursor. These bands are absent from the spectrum of WZr-TMS14 calcined at 600 °C, indicating the loss of the metatungstate molecular structure (Figure 4.9(d)). Broad bands at 945 and 380 cm^{-1} can be seen.

This sample of calcined WZr-TMS14 was further calcined at 750 °C. Its Raman spectrum (Figure 4.9(e)) differed greatly from the spectrum of 600 °C-calcined WZr-TMS14 (Figure 4.9(d)). The former showed strong bands (811, 716, and 281 cm^{-1}) coincident with those of tungsten oxide (Figure 4.9(f)) but not with tetragonal zirconia (Figure 4.9(f)) (650, 465, 323, 276, and 157 cm^{-1} [22]). The major Raman bands of monoclinic ZrO_2 (755, 637, 615, 558, 538, 501, 476, 382, 347, 333, 306, and 221 cm^{-1} [23]) and cubic ZrO_2 (490 cm^{-1}[24]) also were not detected in WZr-TMS14 calcined at 750 °C. Tungsten oxide has a

much greater Raman cross-section than zirconia [25], and can result in undetectable ZrO_2 Raman bands.

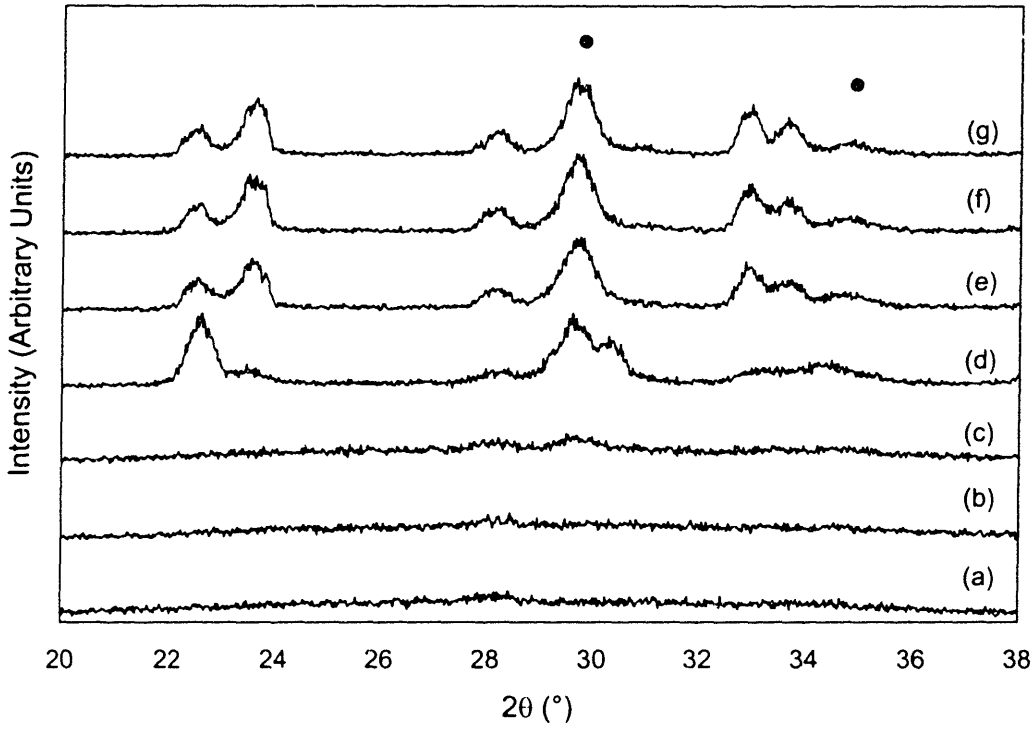

Figure 4.8. *In situ* XRD patterns of 600 °C-calcined WZr-TMS14 at (a) 25 °C, (b) 600 °C, (c) 650 °C, (d) 700 °C, (e) 750 °C, (f) 800 °C, and (g) 850 °C. ● = tetragonal ZrO_2; other peaks noted correspond to tungsten oxide phases.

In situ laser Raman spectroscopy revealed the effect of adsorbed water on WZr-TMS14 calcined at 600 °C (Figure 4.10). In addition to the bands at 945 and 380 cm^{-1}, weak bands at 817, 735, and 543 cm^{-1}, are also detected (Figure 4.10(a)). These smaller bands can be assigned to W–O–W stretching modes of polymeric WO_3 species [44]. A small band appeared at 1018 cm^{-1} after dehydration of the sample, assigned to the stretching vibration of a terminal tungsten monooxo (W=O) bond of surface WO_3 species [26], and the broad band at 945 cm^{-1} remained. The non-shifting of the 945 cm^{-1} after dehydration indicates that the particular bond is not affected by hydrogen-bonding, i.e. there is another population of WO_3 species in WZr-TMS14, besides WO_3 surface species.

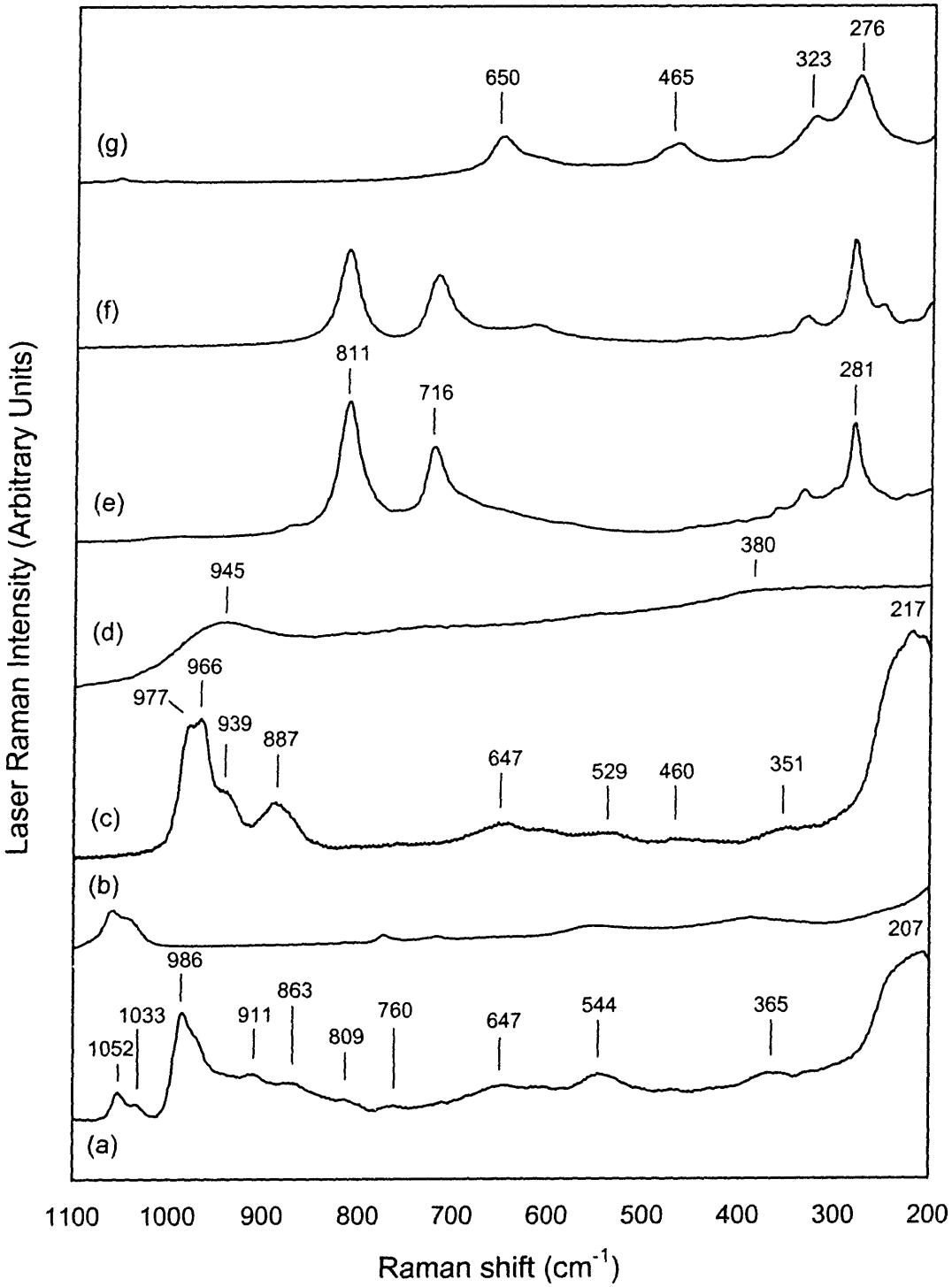

Figure 4.9. Laser Raman spectra collected under ambient conditions: (a) as-synthesized WZr-TMS14, (b) zirconia colloid precursor dried at 90 °C, (c) ammonium metatungstate, (d) WZr-TMS14 calcined at 600 °C, (e) WZr-TMS14 calcined at 600 °C, then at 750 °C, (f) tungsten oxide, and (g) tetragonal zirconium oxide.

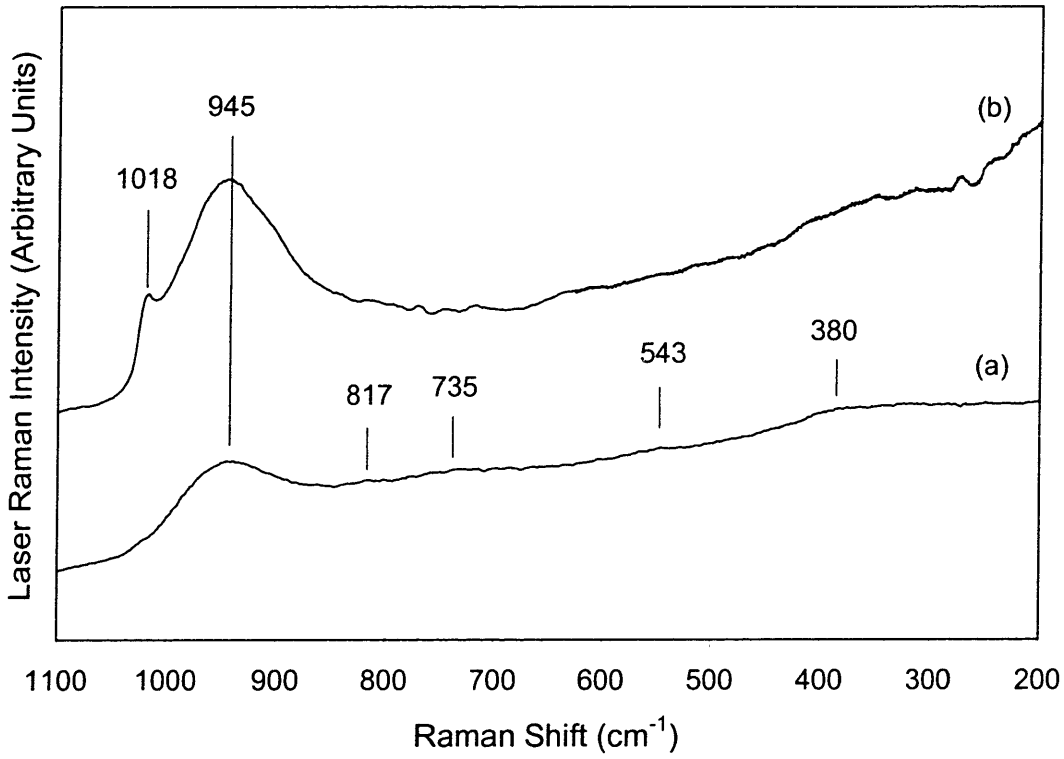

Figure 4.10. *In situ* laser Raman spectra of WZr-TMS14 calcined at 600 °C, collected under (a) ambient and (b) dehydrated conditions.

The nature of the tungsten oxide species in WZr-TMS14 was studied through UV-Vis spectroscopy. As-synthesized WZr-TMS14 exhibits an indirect band gap energy of 3.26±0.05 eV, close to the reported value of 3.23 eV for ammonium metatungstate [18]. After calcination of WZr-TMS14 at 600 °C, the absorption edge red-shifted from ~355 nm (Figure 4.11(b)) to ~385 nm (Figure 4.11(c)), with a decrease in band gap energy to 2.81±0.05 eV. As a reference sample, tungsten oxide gives the UV-Vis spectrum shown in Figure 4.11(d). Its band gap energy was determined to be 2.58±0.05 eV, close to a previously reported value of 2.59 eV [27]. The changes detected in the UV-Vis spectra of WZr-TMS14 due solely to the tungsten species, as the absorption edge of zirconium oxide occurs below 250 nm (Figure 4.11(a)).

The surface composition of WZr-TMS14 was determined via XPS spectroscopy (Figure 4.12). Tungsten, zirconium and oxygen were detected, with residual carbon adsorbed from the atmosphere. No other surface impurities were found. The surface atomic ratio W/Zr was 1.44, compared to the bulk value of 0.23 (equivalent to 30.5 wt% WO_3).

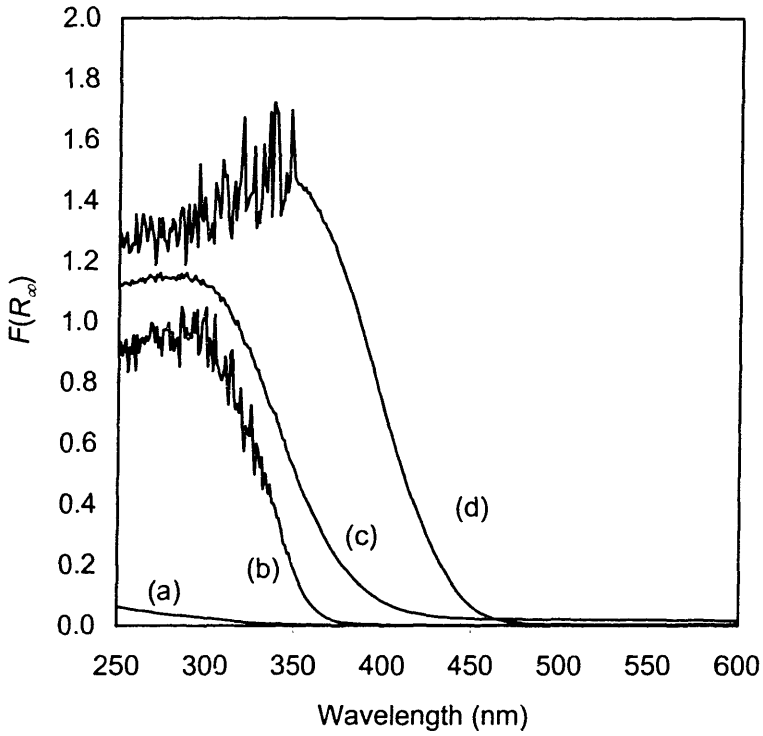

Figure 4.11. Diffuse reflectance UV-Vis spectra of (a) monoclinic ZrO_2, (b) as-synthesized WZr-TMS14, (b) WZr-TMS14 calcined at 600 °C (scaled by 1/16.5), and (d) bulk tungsten oxide (scaled by 1/5.5).

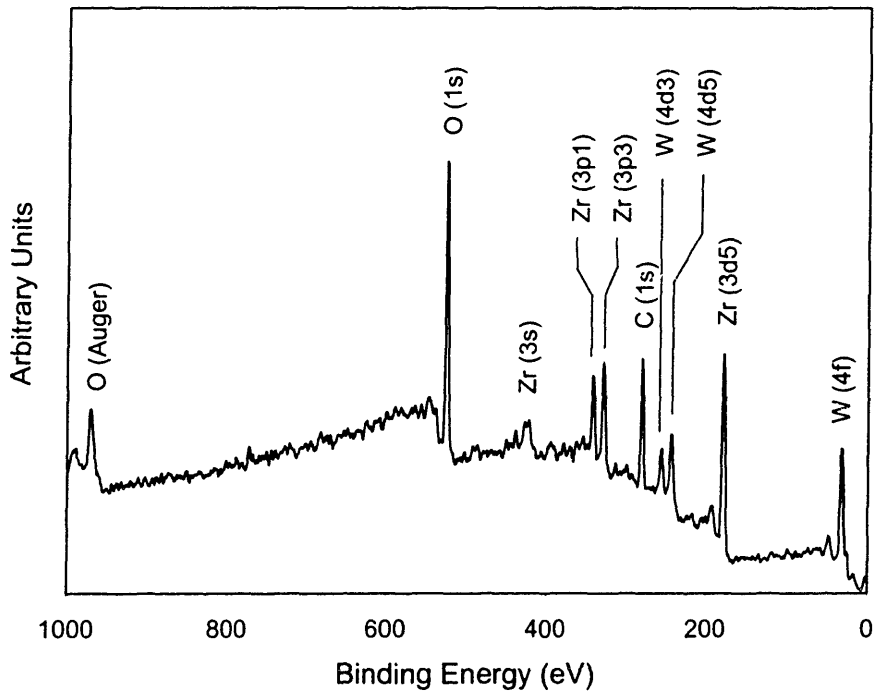

Figure 4.12. XPS spectrum of WZr-TMS14 calcined at 600 °C.

The nature of surface acidity of 600 °C-calcined WZr-TMS14 was determined through *in situ* pyridine-adsorption DRIFT spectroscopy (Figure 4.13). Pyridine exhibits different vibrational modes depending on how it binds to the surface of a particle, e.g. as a pyridinium ion on a Brønsted acid site (B), as a pyridine coordinatively bonded to a Lewis acid site (L), or as a hydrogen-bonded pyridine (H) [28]. For WZr-TMS14, the dominant modes for B and L acid sites are observed at 1538 cm^{-1} and 1446 cm^{-1}, respectively. Less intense bands are other vibrational modes of bound pyridine (1636 cm^{-1} (B), 1574 cm^{-1} (L)) and combinations of modes (1609 cm^{-1} (H+L), 1487 cm^{-1} (B+L)). B and L acid sites were present at 150 °C and at an elevated temperature of 350 °C. The B/L site ratios, estimated from the corresponding peak areas, were 0.36 and 0.46 at 150 °C and 350 °C, respectively. WZr-TMS14 was found active for the gas-phase isomerization of 1-butene, comparable to commercial sulfated zirconia (SZ) (Table 4.3).

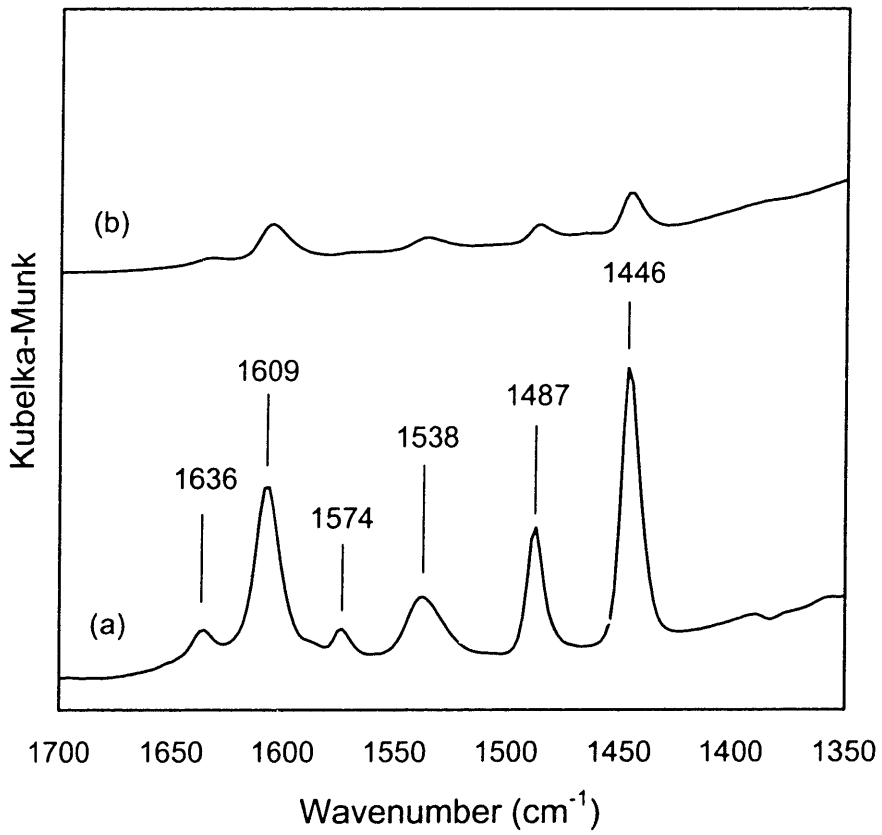

Figure 4.13. *In situ* DRIFT spectra of 600 °C-calcined WZr-TMS14 with adsorbed pyridine at (a) 150 °C and (b) 350 °C.

Table 4.3. 1-butene isomerization over WZr-TMS14 and SZ.[a]

Initial Product Distribution (%)[b]	WZr-TMS14	SZ
1-Butene	16.3	19.7
trans-2-Butene	48.2	40.7
cis-2-Butene	30.7	28.1
Isobutene	1.4	7.2
Others[c]	3.4	4.3

[a]Reaction conditions: 350 °C, WHSV = 3 hr^{-1}
[b]Calculated as (moles of product detected)/(moles of initial 1-butene)
[c]Difference by mole balance

WZr-TMS14 prepared with zirconyl nitrate was found to be stable upon surfactant removal, exhibiting a SAXS peak before and after calcination at 250 °C under nitrogen (Figure 4.14). The framework contracted by 20% upon calcination, as indicated by a decrease

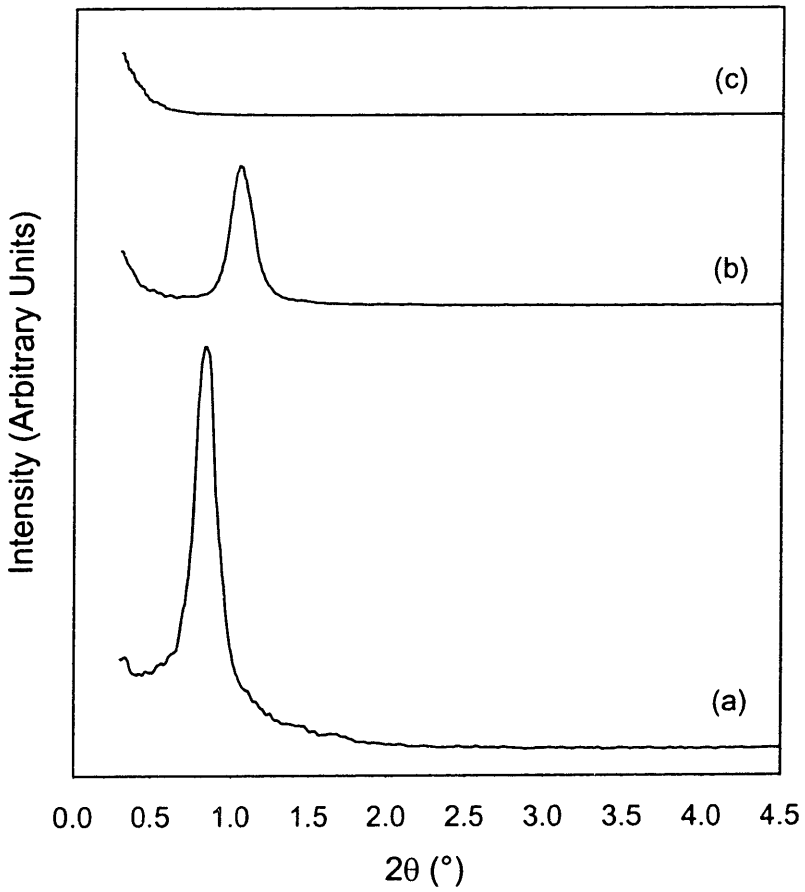

Figure 4.14. SAXS patterns of WZr-TMS14 prepared with zirconyl nitrate salt precursor: (a) as-synthesized, (b) calcined at 250 °C, and (c) calcined at 600 °C.

in the Bragg spacing, from 10.6 nm to 8.4 nm. Large regions of hexagonally-packed pores were observed via TEM (Figure 4.15). The mesoporous structure was corroborated by the

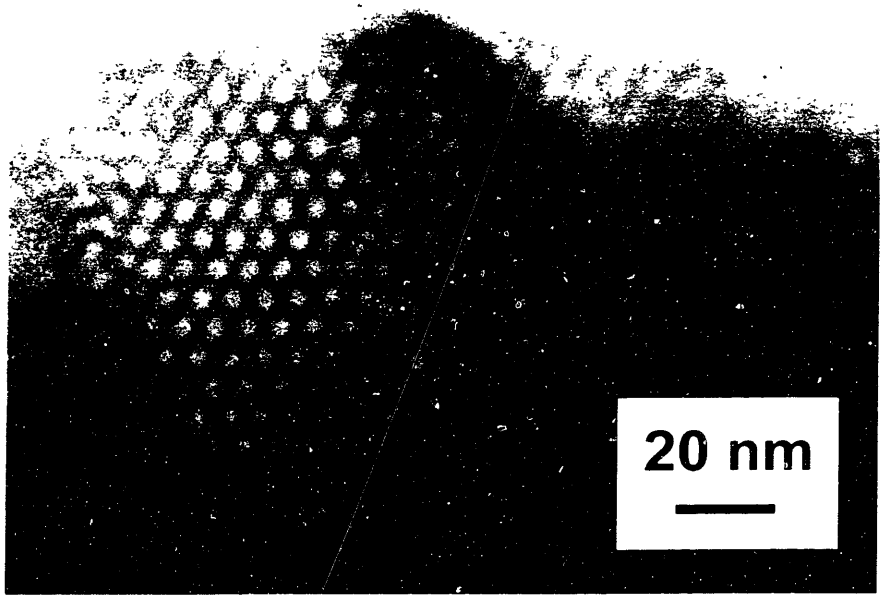

Figure 4.15. TEM image of 250 °C-calcined WZr-TMS14 prepared with zirconyl nitrate.

nitrogen adsorption isotherm and pore size distribution (Figure 4.16(a)). The sample has a narrow BJH pore size distribution (Figure 4.16(b)) and a BET surface area of 80 m^2/g. After calcination at 600 °C, the surface area of this material was reduced to 4 m^2/g and the SAXS peak disappeared (Figure 4.14(c)), indicating a collapse in the mesostructure of WZr-TMS14.

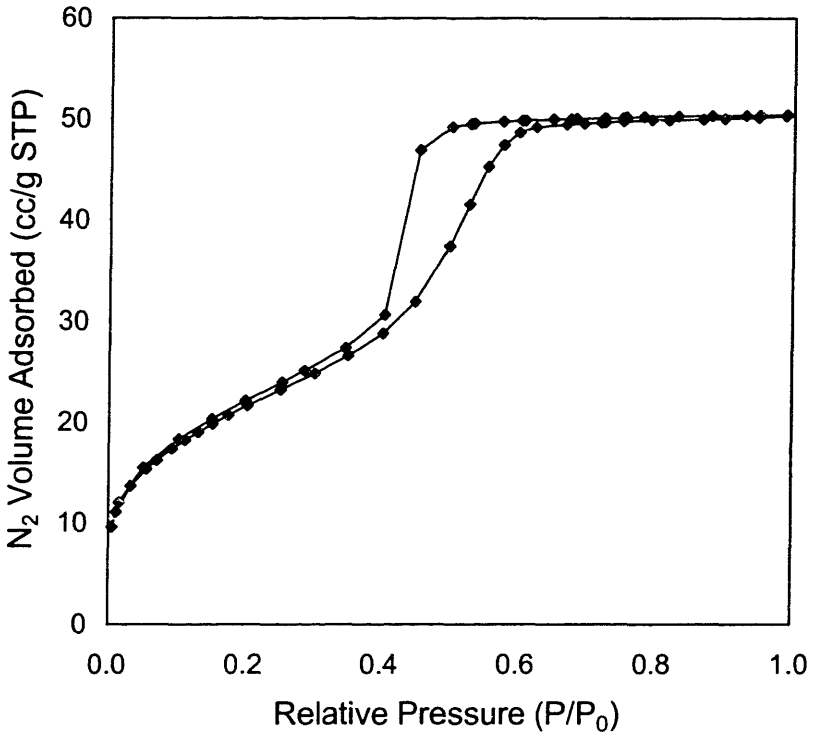

Figure 4.16. (a) Nitrogen adsorption isotherm of WZr-TMS14 prepared with zirconyl nitrate and calcined at 250 °C.

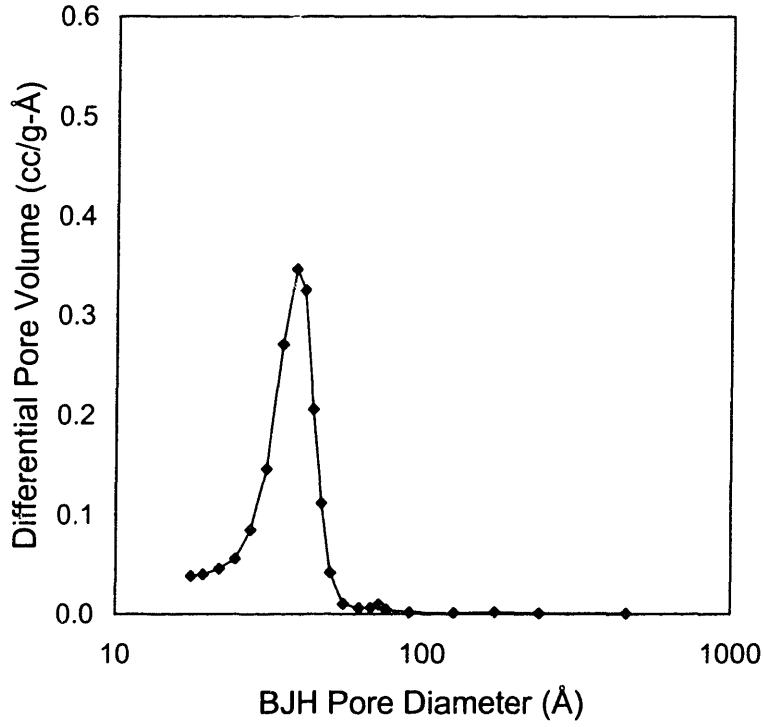

Figure 4.16. (b) BJH pore size distribution of WZr-TMS14 prepared with zirconyl nitrate and calcined at 250 °C.

4.4 Discussion

4.4.1 Microstructure of Mesoporous Tungstated Zirconia WZr-TMS14

Mesoporous tungstated zirconia was prepared successfully using zirconium oxide colloid particles as a precursor. Its porous structure is highly tortuous, as shown in Figure 4.2. Mesoporous WZr-TMS14 resembles supramolecular-templated mesoporous materials composed of disordered pores like KIT-1 [29], L_3 sponge [30], and MSU-1 [31], but there are some significant structural and compositional differences. WZr-TMS14 has larger pores (4 nm vs. ~2.5 nm) and thicker pore walls (4-6 nm vs. ~1 nm), due to the much longer templating molecules employed. In comparison, mesoporous silica SBA-15 silica prepared with the same triblock co-polymer P123 template has a pore size of 4.7-8.9 nm and pore walls of 3.1-6.4 nm, depending on aging conditions [32]. The use of the polymer template leads to thicker walls in mesoporous silicates, mesoporous non-silicates [3], and WZr-TMS14, with wall thicknesses that are on the same length scale as the 5-nm zirconia colloid nanoparticles used in WZr-TMS14 preparation. SBA-15 is completely amorphous compared to WZr-TMS14, which has a nanocrystalline zirconia framework, and possesses hexagonally-packed cylindrical pores that are quite different from the worm-like mesopores of WZr-TMS14.

WZr-TMS14 exhibits nanocrystallinity, since the ZrO_2 grains were too small to diffract X-rays (Figure 4.5(b)) but were detected via TEM studies (Figure 4.2(a) inset, Figure 4.2(b)). This feature was attributed to the nanocrystalline colloidal precursor (Figure 4.1) and reflected the zirconia nanoparticles set within the inorganic framework of WZr-TMS14. The pore walls of WZr-TMS14 were not completely crystalline though, as indicated by the apparent loss of the cubic ZrO_2 (200) and (311) diffraction rings and the broadness of the remaining rings in the SAED pattern (Figure 4.2(a), inset). The low crystallinity of WZr-TMS14 might be a consequence of the high tungsten oxide content. Tungsten oxide was not found as a separate crystalline phase despite a very high loading of 30.5 wt%, and so its ultrahigh dispersion with the zirconia nanoparticles was concluded.

Partial amorphization of the zirconia nanoparticles was also suggested by the diffuseness of the electron diffraction rings of WZr-TMS14 (Figure 4.2(a) inset). Inorganic metal oxides are known to adsorb ionic species from solution via ion-exchange or electrostatic interactions. For example, modelling studies by Karakonstantis *et al.* showed that tungstate species can deposit onto γ-alumina through both types of interactions, depending on the

exposed surface hydroxyl groups [33]. An additional mode of interaction was offered by Carrier *et al.*, who found that solubilized tungstate species can leach the surface of γ-alumina, even near neutral pH [34]. This "ligand-promoted oxide dissolution" resulted in the formation of aluminotungstate species, which are thought to deposit back onto the alumina. An extension of this phenomenon to zirconia nanoparticles could explain the partial loss in crystallinity of the zirconia grains within WZr-TMS14. In an analogous fashion, the zirconia surface would undergo dissolution and redeposition in the presence of the metatungstate salt. Tungsten cations could be incorporated within the top surface layer of the zirconia nanoparticles, noting that tungsten cations are slightly soluble in zirconium oxide (up to 2.5 mol% WO_3 below 1000 °C) [35]. Scheithauer *et al.* speculated that zirconium cations could be complexed with tungstates as a heteropolyacid-like species on the surface of tungstated zirconia catalysts [36].

Tungsten oxide might be visualized as an overlayer on the zirconia nanoparticles. The surface density of tungsten oxide on zirconia is calculated to be 6.0 WO_3/nm^2 (or 10.0 $\mu mol/m^2$), based on the tungsten oxide loading (30.5 wt%) and the overall BET surface area (130 m^2/g). A surface density of 4.0 WO_3/nm^2 (6.6 $\mu mol/m^2$) corresponded approximately to a monolayer coverage of tungsten oxide on a zirconia support, as determined from laser Raman spectroscopy studies [25] and gas titration experiments [37]. A surface density in excess of the monolayer value led to the formation of tungsten oxide for a variety of metal oxide supports [25], but no such phase segregation was found in WZr-TMS14.

This "colloid overlayer" model could be explored more closely by examining the surface area and tungsten oxide loading dependence on zirconia colloid size, assuming a spherical morphology for the zirconia particles. In general, the specific surface area (m^2/g) of a hard sphere is given by,

$$S_{sphere} = \frac{6000}{\rho D},$$

where ρ is density (g/cm^3) and D is diameter (nm). The relation is useful as an estimate for the maximum possible surface area, but becomes less accurate when applied to nanometer-sized particles since the physical properties of nanoparticles tend to deviate from those of the bulk. As an approximation, the density of bulk cubic zirconia, 6.206 g/cm^3, was be used.

Assuming the surface density of tungsten oxide to be 6.0 WO_3/nm^2 for all ZrO_2 nanoparticle sizes, the surface area (m^2/g) for the tungsten oxide-coated spheres is given by

$$S = \frac{S_{sphere}}{2.31\times10^{-3}S_{sphere}+1}.$$

The loading of tungsten oxide (wt%) is similarly derived as

$$W = \frac{2.31\times10^{-1}S_{sphere}}{2.31\times10^{-3}S_{sphere}+1}.$$

As illustrated in Figure 4.17, the theoretical surface area and tungsten oxide content would increase with decreasing ZrO_2 colloid size. The colloid overlayer model predicted that a colloid particle size of 5 nm would correspond to ~130 m^2/(g sample) and ~30 wt% WO_3, nearly identical to those values measured for WZr-TMS14. It was noted that the derivation of the model accounted only for the measured WO_3 surface density of WZr-TMS14. Thus, WZr-TMS14 could be accurately described as 5-nm zirconia colloid particles coated with tungsten oxide and arranged into a mesoporous framework.

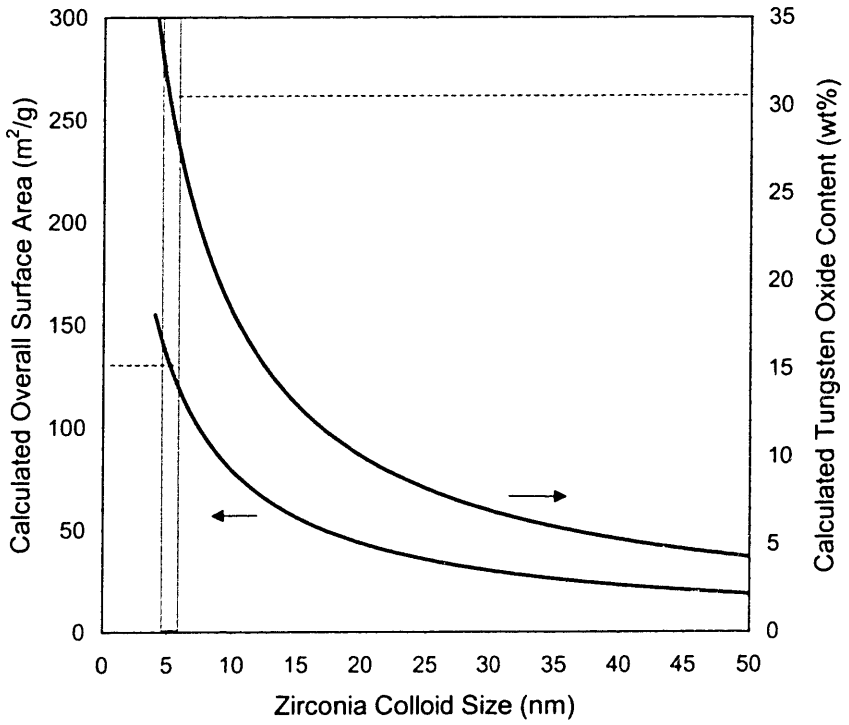

Figure 4.17. Theoretical overall surface area and tungsten oxide content of WZr-TMS14 as a function of zirconia colloid size.

A zirconia colloid precursor with a nominal particle size of 50 nm was used to prepare WZr-TMS14. The resulting material had a surface area of 108 m^2/g and a pore size of 50 Å, differing slightly from WZr-TMS14 prepared with 5-nm colloid particles. According to the colloid overlayer model, however, a colloid size of 50 nm should give a material with a surface area of ~18 m^2/g. This discrepancy results from the idealization of the colloid precursor as monodispered spherical particles. Ward and Ko reported that only half of the particles (by weight) in the 50-nm colloid precursor solution were actually 50 nm, and the other half of the particles were ~5 nm [12]. They inferred that the 50-nm particles were aggregates of 5-nm particles. Colloid particles smaller than 5 nm were calculated to give larger surface areas than 130 m^2/g, but zirconia colloid particles in this size range were not available.

WZr-TMS14 exhibited a distinct SAXS peak before and after calcination at 600 °C. This main scattering peak was broad, and there were no higher-order peaks that indicated a highly-defined pore arrangement. The low-angle scattering peak represented an average scattering distance between the inorganic walls, similar to that exhibited by disordered polymer-inorganic composites [38]. This X-ray scattering feature is not unlike the broad XRD band exhibited by amorphous materials, denoting a particular interatomic distance [39]. The 25% contraction of the WZr-TMS14 framework is large compared to typical values shown by SBA-15 (1-8%) [32].

4.4.2 Thermal Stability of WZr-TMS14

WZr-TMS14 was stable to at least 600 °C after surfactant removal via calcination, as confirmed by TEM, nitrogen adsorption analysis, XRD, SAXS, and Raman studies. An exothermic process was detected at 715 °C, and clearly represented the crystallization of the mesoporous framework of WZr-TMS14. *In situ* VT-XRD studies showed the transition from an amorphous WZr-TMS14 system to a mixture of tetragonal zirconia and tungsten oxide phases (Figure 4.8). The transition temperature of ~650 °C as detected through *in situ* VT-XRD was lower than the 715 °C determined from TGA/DTA due to different experimental conditions, e.g. different temperature ramp profiles and different atmospheres. The sudden weight loss detected above 700 °C was attributed to the release of water from the dehydroxylation and crystallization of the inorganic framework (Figure 4.6). Occurring with

the crystallization of WZr-TMS14 was the collapse of the mesostructure, marked by the loss of the SAXS peak.

WZr-TMS14 crystallized at a much higher temperature (by ≥250 °C) compared to either the hydrous zirconia or tungsten oxide materials. The suppression of crystallization further supported the notion of intimate mixing of tungsten and zirconium oxides in the porous framework of WZr-TMS14. Amorphous hydrous zirconium oxide crystallized to the tetragonal phase at a temperature of 428 °C. Such an exothermic process is known as the "glow phenomenon," typical of hydrous metal oxides [40,41]. The exotherm has an enthalpy of 21.0±1.4 kJ/mol (Figure 4.7(c)), which was within the range of values reported in literature (17-19 kJ/mol [41], 23.2 kJ/mol [25], 29-33 kJ/mol [42]). The discrepancies in the literature values were likely because the measured heat included the effects of desorption and/or decomposition of volatile species that accompanied crystallization.

The dried zirconia colloid precursor exhibited a series of small exothermic peaks (410-470 °C) with an estimated enthalpy of 6.3±2.1 kJ/mol (Figure 4.7(b)). The colloidal zirconia precursor had a much smaller exotherm than hydrous zirconia, suggesting that the pre-formed nanoparticles were thermodynamically more stable. However, there might have been an endothermic heat contribution from the desorption of residual nitrates, which would cause some underestimation of the enthalpy. The presence of nitrates was evidenced by the nitrate bands in the Raman spectrum of colloidal zirconia calcined at 450 °C (Figure 4.9(g)).

Hydrous tungsten oxide underwent crystallization between 390-460 °C (Figure 4.7(d)), as confirmed by XRD analysis of the material heated to 500 °C. The exotherm had an enthalpy of 38.4±2.7 kJ/mol, higher than those of colloid or hydrous zirconia. WZr-TMS14 was estimated to have a crystallization enthalpy of 9.1±2.7 kJ/(mol ZrO_2•0.23WO_3).

4.4.3 Nature of Tungsten Oxo Species in WZr-TMS14

The metatungstate species was essentially unchanged after incorporation into the supramolecular-templated mesostructure of WZr-TMS14, as indicated by the similarity of the Raman spectra (Figures 4.9(a) and (c)) and calculated E_g's of as-synthesized WZr-TMS14 and ammonium metatungstate. Calcination, however, drastically changed the nature of the tungstate species. The metatungstate anion is composed exclusively of WO_6 octahedra [43], and the Raman band at ~200 cm^{-1} illustrated the W-O-W connection between the octahedra.

The loss of this and the other Raman bands after calcination at 600 °C indicated the breakdown of the metatungstate in the as-synthesized WZr-TMS14, with the appearance of the broad band at 945 cm^{-1} indicating a new state of the tungsten oxo species (Figure 4.9(d)).

The Raman spectrum of calcined WZr-TMS14 differed from those of conventional tungstated zirconia prepared via impregnation. Scheithauer *et al.* found that tungstated zirconia exhibited Raman bands at 834 cm^{-1} and 930 cm^{-1} [36]. The bands were assigned to asymmetric stretching of W–O–W bonds and symmetric stretching of a terminal W=O bond, respectively. With increasing tungsten loading, the W=O band shifted to higher frequencies (up to 988 cm^{-1}) while the W–O–W band remained at 834 cm^{-1} [36]. The W–O–W bonds indicated the existence of a polymeric tungsten oxo species. It would seem that W=O stretching could be assigned to the 945 cm^{-1} band found in 600 °C-calcined WZr-TMS14 (Figure 4.10(a)).

Under the ambient conditions used to collect the Raman spectra, water was present as an adsorbed surface species. Water is known to hydrogen-bond with surface metal oxide bonds, especially those of terminal oxo species (M=O, metal-oxygen double bond), reducing its stretching frequency [25]. Dehydration of calcined WZr-TMS14 would be expected to shift the 945 cm^{-1} band to a higher frequency, and evidence of this blue-shifting was observed (Figure 4.10(b)). A new band at 1018 cm^{-1} emerged and was assigned to the terminal W=O stretching [25,36]. Unusually, the 945 cm^{-1} band remained in place, indicating the existence of a tungsten oxo species that was not affected by adsorbed water. Scheithauer *et al.* reported the W–O–W stretching band at 834 cm^{-1} did not shift upon dehydration of their tungstated zirconia samples [36], which shared the same behavior of the 945 cm^{-1} band. They also reported a new band at 900 cm^{-1}, which they tentatively attributed to W–O–Zr stretching. On the other hand, Wachs and co-workers found that under *in situ* dehydrated conditions, the W–O–W stretching band shifted to higher frequencies (as high as 875 cm^{-1} for 5 wt% WO_3 loading) with increasing tungsten loading on their tungstated zirconia samples [44]. The 1018 cm^{-1} Raman band of dehydrated WZr-TMS14 might represent a polymeric tungsten oxo species different from that of Scheithauer *et al.*'s samples. We attributed the 945 cm^{-1} band of WZr-TMS14 to W–O–W vibrations of a polymeric tungsten oxo species that was not affected by hydrogen-bonding from adsorbed water, but this band could also contain a contribution from W–O–Zr vibrations.

The new state of the tungstate oxo species was also manifested in the UV-Vis spectra of calcined WZr-TMS14 (Figure 4.11). Representing the metatungstate species, the absorption edge of as-synthesized WZr-TMS14 red-shifted after calcination at 600 °C, and the band gap energy decreased from 3.26 eV to 2.81 eV. The band gap energy is the photon energy required to cause a ligand-to-metal charge transfer (LMCT), and for a semiconductor like tungsten oxide, the $O^{2-} \rightarrow W^{6+}$ LMCT transition occurs at a measured E_g of 2.58 eV [27]. Band gap energies of nanocrystalline semiconducting systems exceed the E_g values of their bulk counterpart due to quantum confinement effects. The trend still holds in supported semiconductors, such as tungstated zirconia, even though the semiconducting domain may not be crystalline. The band gap energies depend on the nature of W–O bonds, e.g. connectivity, molecular structure, bond angles, and support effects [18]. The decrease in band gap energy of WZr-TMS14 after calcination suggested that the metatungstate species (containing 12 WO_6 octahedra) coalesced into larger tungsten oxo domains. Nanocrystalline tungsten oxide was not observed, as tungsten oxide bands were absent from the Raman spectrum of calcined WZr-TMS14 (Figure 4.9(d)). Tungsten oxide Raman bands were observed after WZr-TMS14 was calcined at 750 °C (Figure 4.9(e)), above the crystallization temperature of 715 °C (Figure 4.7(a)). The Raman bands at 811 and 716 cm^{-1} were assigned to W–O–W stretching modes, and the 281 cm^{-1} band was attributed to W–O–W bending [21b].

4.4.4 Surface Acidity of WZr-TMS14

Tungstated zirconia have been investigated as a solid acid catalyst ever since the discovery of its very strong acidity by Hino and Arata [45]. It can be prepared via impregnation through adsorption, impregnation through incipient-wetness, or coprecipitation. This study is the first report of a supramolecular templating synthesis route to tungstated zirconia.

WZr-TMS14 contained both Brønsted (B) and Lewis (L) acid sites (Figure 4.13). The absorbance peaks representating B and L sites decreased in intensity with a desorption temperature increase, but the B/L site ratio increased slightly from 0.36 to 0.46, suggesting the B sites were stronger than L sites. The B sites detected at 350 °C *vide infra* were responsible for the isomerization activity of WZr-TMS14 at 350 °C (Table 4.3). WZr-TMS14 was more active for double-bond isomerization than SZ, based on the relative abundance of

cis- and trans-2-butenes. SZ and WZr-TMS14 were both active for 1-butene skeletal isomerization, indicating the catalysts contained B sites. There were trace amounts of propene, pentane and pentenes (not listed), and carbonaceous deposits accounted for the carbon balance. SZ had a higher activity than WZr-TMS14, indicating either it contained stronger B sites or a greater number of B sites. However, the number of B sites did not correlate with surface dopant amount, as SZ and WZr-TMS14 had sulfate coverages of 3.22 S/nm^2 (Table 3.2) and 6.0 W/nm^2, respectively.

The surface acidity in WZr-TMS14 and conventional tungstated zirconia originated from the presence of the tungsten surface dopant. Tungsten oxide by itself is an acidic material [27], and has been investigated as an unsupported acid catalyst [19,46]. It can reduce easily to substoichiometric oxides [46], a characteristic also found in the tungsten oxide of tungstated zirconia systems [47,48]. Barton *et al.* suggested that the slightly reduced tungsten oxide surface clusters could act as B acid sites, especially if tungstated zirconia was doped with Pt and a H_2 reaction atmosphere was used [18,48]. Santiesteban *et al.* reported the beneficial effect of hydrogen spillover in the catalytic activity of Pt/tungstated zirconia for pentane hydroisomerization [47].

4.4.5 Proposed Method Of Mesostructure Formation

The supramolecular templating synthesis of WZr-TMS14 is thought to entail the cooperative interaction among the three components in order for self-assembly to occur. We propose that such interactions involves electrostatic attraction and hydrogen bonding (Figure 4.18). The three components assume a charge in solution under the low pH conditions used. Zirconia has a point-of-zero charge (PZC) between 4 and 6, the pH at which there is the net surface charge is zero [49]. In the precursor solution and synthesis mixture, the pH was ~0.5, below the PZC of zirconia, so the zirconia colloid particle surface would be protonated and assume a positive charge.

The metatungstate species is a molecular cluster with an overall charge of -6 and is unaffected by low pH's [50]. In fact, low pH's favor the formation of metatungstate and other isopolytungstates [43]. Through a simple charge attraction, the metatungstate species would adsorb onto the zirconia particle surface. A related tungstosilicate salt ($SiW_{12}O_{40}^{4-}$) was shown to deposit on positively-charged zirconia nanoparticles [51].

The triblock copolymer surfactant P123 is postulated to carry a positive charge. Such amphiphilic polymers have a hydrophobic poly(propylene oxide) (PPO) backbone and two hydrophilic poly(ethylene oxide) (PEO) ends. At the surfactant concentration used (5.7 wt%), P123 can form micelles, in which the PPO block comprises the micelle core and the PEO makes up the surrounding corona region. It is known that polyethylene glycol, a single PEO block of a particular length, is hydrated with 2-3 water molecules per EO group in aqueous solution [52], and so the PEO corona region in the micelle contains water which hydrogen bonds with the PEO ends. There is evidence that polyethylene glycol can interact with hydrated protons, presumably through hydrogen bonding [53], which supports the postulate that the PEO ends in the P123 micelles can hydrogen bond with hydrated protons. Thus, a positively-charged surfactant micelle can be effectively formed.

The formation of WZr-TMS14 could occur with the requisite charges in place (Figure 4.18), and the mechanism of formation could be described as $(S^0H^+)(\Gamma C^+)$, where S^0 represents the nonionic surfactant; H^+, the proton; Γ, the metatungstate; and C^+, the inorganic colloid. Through attractive electrostatic interactions, the metatungstate species would bind to both the micelle and zirconia colloid moieties, forming WZr-TMS14. Zhao *et al.* invoked a similar mechanistic argument $(S^0H^+)(X^-I^+)$ to explain the formation of large-pore mesoporous silicate SBA-15, where S^0 is the same type of nonionic surfactant; X^-, a halide anion; and I^+, the silica molecular precursor [32]. They too suggested that the triblock copolymer surfactant micelles hydrogen bonded with hydrated protons to attain an effective positive charge. In spite of the similarities in formation mechanism, WZr-TMS14 differs from SBA-15 in two ways: (1) the inorganic anion is retained and (2) the metal oxide precursor is colloidal in nature. In the formation of mesoporous non-silicates using triblock copolymer surfactants, Yang *et al.* proposed that there were crown-ether coordination bonds that occurred between the metal chloride precursor and the PEO of the micelles [3]. Such metal cation-chelating interactions would take place in nonaqueous solutions, as was found for metal cation-polyethylene glycol systems [54], but cannot occur in aqueous environments such as that used for WZr-TMS14 synthesis.

This "surfactant/colloid templating" mechanism for WZr-TMS14 formation was successfully extended to the preparation of other templated oxides, such as WTi-TMS14 and WAl-TMS14 (Chapter 5). The application of this approach to the colloidal solutions of other

metal oxides, such as titanium oxide and aluminum oxide, demonstrated the generality of the proposed mechanism. Direction substitution of the metatungstate anionic species with isopolymolybdates did not lead to mesostructured materials, as no precipitation occurred.

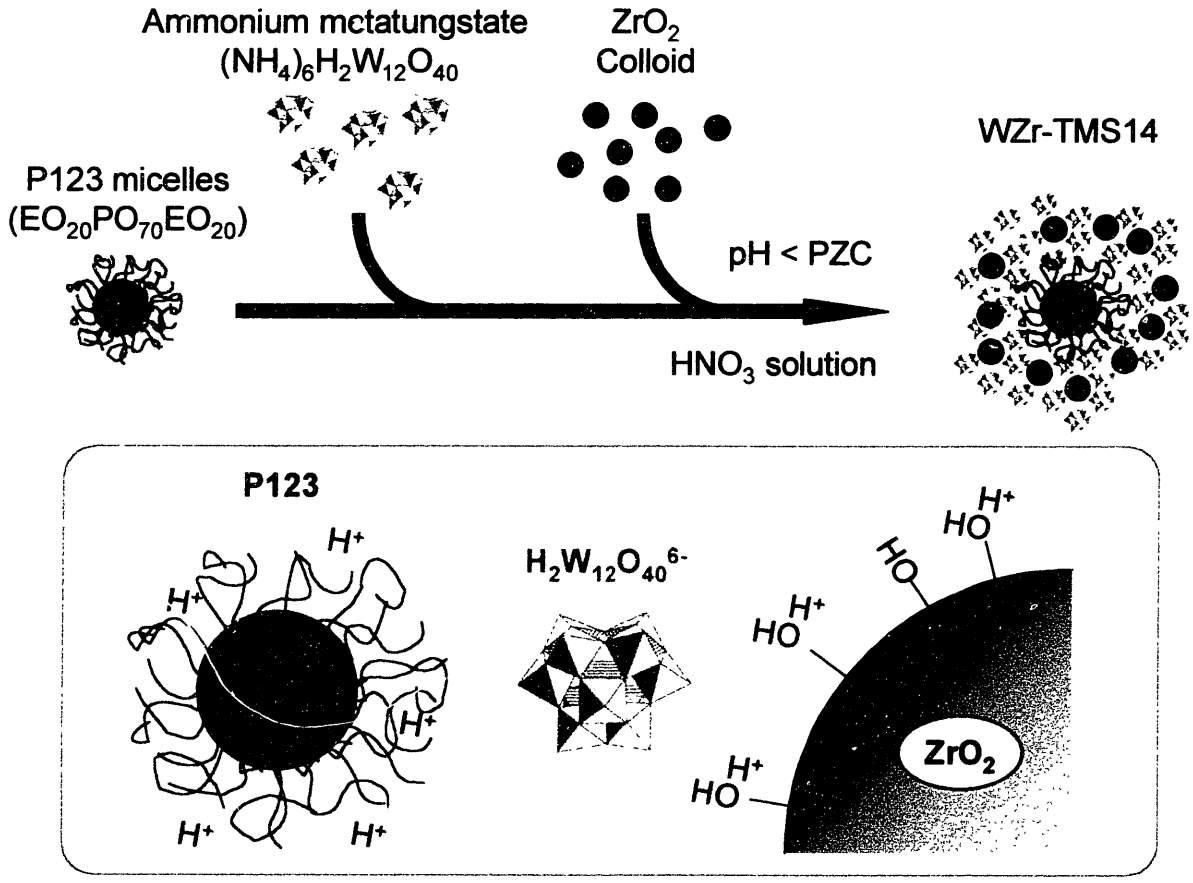

Figure 4.18. Schematic of the proposed mechanism of formation.

Molybdate salts can form anionic species similar to metatungstates under low pH's [43], but the solution chemistry is different enough to not offer the desired attractive interactions among the precursors and to preclude the mesostructure formation in this case.

The replacement of the zirconia colloid by a zirconium salt still led to a mesoporous tungstated zirconia material. WZr-TMS14 prepared with the $ZrO(NO_3)_2$ salt possessed mesopores with a highly ordered hexagonal packing (Figure 4.15), which was not observed in samples prepared with colloidal zirconia. Perhaps the finite size of the zirconia colloid nanoparticles restricted the packing of the micelles into hexagonal rods, which would be necessary to achieve a well-defined hexagonal pore packing. Indeed, the pore walls were

thinner in the WZr-TMS14 prepared with the zirconium salt than those prepared with the 5-nm colloid precursor. WZr-TMS14 prepared with the $ZrO(NO_3)_2$ salt was stable to at least 250 °C, but collapsed at 600 °C, indicating the lack of mesostructure stability otherwise found in WZr-TMS14 prepared with zirconia colloid nanoparticles. Other zirconium salts led to the formation of mesostructured surfactant-templated zirconia composites, but the resulting materials were not stable to calcination at 250 °C. These studies indicated the importance of the pore wall thickness and crystallinity in the thermal stability of WZr-TMS14, and the sensitivity towards the anion employed in the zirconium salt precursors.

The use of different polymer surfactants to control pore size was possible (Table 4.2). Pore size of WZr-TMS14 was found to be dependent on the size of the surfactant molecule, and the relative size of the hydrophilic PEO and hydrophobic PPO blocks. Surfactants with a smaller molecular weight were better templates than those with a larger MW, in terms of producing WZr-TMS14 with a high surface area and a distinct pore size. However, surfactants with similar MW (e.g. $EO_5PO_{70}EO_5$ and $EO_{20}PO_{39}EO_{20}$) led to materials with very different surface areas and pore sizes. The difference could be attributed in the relative hydrophobicity and hydrophilicity in the polymer surfactants, quantified by the HLB values [55]. While the HLB values have been typically used to determine emulsification properties of surfactants, they could provide a quantification of how oil-like a particular surfactant is compared to another [15]. A lower HLB value indicates a surfactant is more hydrophobic, and a higher HLB value indicates more hydrophilicity. Also, it is known that a more hydrophobilic surfactant would have a higher aggregation number and therefore a larger micelle size [59]. This might explain why the pores are larger in the material prepared with $EO_5PO_{70}EO_5$ (L121) than with $EO_{20}PO_{39}EO_{20}$ (P84) (Table 4.2). The L121 micelles would be larger than P84 micelles because the larger aggregation number of L121. P103 ($EO_{17}PO_{60}EO_{17}$) is a similarly-sized polymer with a HLB value of 9, compared to L121 (HLB = 1) and P84 (HLB = 14). Its use as a template resulted in a 600°C-calcined WZr-TMS14 material with a surface area and pore size intermediate to those prepared from L121 and P84. For a given size surfactant, a lower HLB value appeared to favor the formation of a mesoporous WZr-TMS14.

There was some indication that polymers with very high HLB values made for poor templating agents. F127 ($EO_{106}PO_{70}EO_{106}$) and F87 ($EO_{20}PO_{39}EO_{20}$) had HLB values of 22

and 24, respectively, and the resultant materials were nonporous (Table 4.2). The MW's were larger than the 4000~5000 range used above, and so there could also be a polymer size effect on mesostructure formation.

There was a significant effect of surfactant size on the physical properties of WZr-TMS14. P123 had a HLB value of 8, similar to that of P103, but P123 was 16% larger than P103. The material resulting from the larger P123 polymer had a higher surface area and a larger pore size. Thus, the pore size dependence on surfactant size was observed, for a given HLB value.

Mesoporous tungstated zirconia could be prepared using 15-nm latex spheres as a "hard" template also, instead of triblock copolymer surfactants. This material, WZr-TMS15, had a surface area of 127 m^2/g and a pore size of 15 nm, which was the size of the latex template (Table 4.2). Many recent reports have shown that ordered pores with diameters of 100 nm and larger could be attained by using latex polystyrene spheres as the templating agent [56,57]. The latex sphere-templated macroporous materials were prepared by forming a close-packed matrix of spheres and then infiltrating the matrix with the inorganic precursor. Such a sequential process differed markedly from that of surfactant-templated mesoporous materials, in which free energy drives the cooperative self-assembly of surfactant molecules and inorganics [8]. Stucky and co-workers showed that precise pore control on the macropore and mesopore regimes was possible through a combination of surfactant and latex sphere templating [58]. Unlike these synthesis routes which involve sequential processing, cooperative self-assembly occurred in the derivation of WZr-TMS15. The requisite interactions were presumably provided by residual F87 molecules on the surface of the latex nanospheres.

4.5 Summary

Mesoporous tungstated zirconia was successfully produced through a novel surfactant/colloid templating approach. This new synthesis route involved the cooperative self-assembly of a metatungstate salt, zirconia colloid particles, and triblock copolymer surfactants. The metatungstate species was critical to the colloid/surfactant templating synthesis approach as it acted to "glue" the zirconia colloid particles together. This role of the metatungstate species was demonstrated by the derivation of tungstated zirconia

mesostructures using both zirconium salts and zirconia colloid nanoparticles as precursors. The removal of the templating surfactant from colloid-derived materials via calcination could be accomplished without collapse of the pore structure. Structural stability of WZr-TMS14 materials could be attributed to the nanocrystalline framework constituted of zirconia colloid particles; lower thermal stability was noted in WZr-TMS14 prepared with zirconium salts. Pore size control was achieved through the use of triblock copolymer surfactants of different sizes and HLB values, and also with latex nanospheres.

4.6 References

[1] (a) Antonelli, D. M.; Ying, J. Y. *Angew. Chem. Int. Ed. Engl.* **1996**, *35*, 426. (b) Antonelli, D. M.; Nakahira, A.; Ying, J. Y. *Inorg. Chem.* **1996**, *35*, 3126. (c) Antonelli, D. M.; Ying, J. Y. *Chem. Mater.* **1996**, *8*, 874.

[2] (a) Sun, T.; Ying, J. Y. *Nature* **1997**, *389*, 704. (b) Sun, T.; Ying, J. Y. *Angew. Chem. Int. Ed. Engl.* **1998**, *37*, 664.

[3] (a) Yang, P.; Zhao, D.; Margolese, D. I.; Chmelka, B. F.; Stucky, G. D. *Nature* **1998**, *396*, 152. (b) Yang, P.; Zhao, D.; Margolese, D. I.; Chmelka, B. F.; Stucky, G. D. *Chem. Mater.* **1999**, *11*, 2813.

[4] Stein, A.; Fendorf, M.; Jarvie, T. P.; Mueller, K. T.; Benesi, A. J.; Mallouk, T. E. *Chem. Mater.* **1995**, *7*, 304.

[5] (a) Wong, M. S.; Antonelli, D. M.; Ying, J. Y. *Nanostr. Mater.* **1997**, *9*, 165. (b) Wong, M. S.; Ying, J. Y. *Chem. Mater.* **1998**, *10*, 2067.

[6] Linden, M.; Blanchard, J.; Schacht, S.; Schunk, S. A.; Schüth, F. *Chem. Mater.* **1999**, *11*, 3002.

[7] Tian, Z.-R.; Tong, W.; Wang, J.-Y.; Duan, N.-G.; Krishnan, V. V.; Suib, S. L. *Science* **1997**, *276*, 926.

[8] Huo, Q.; Margolese, D. I.; Ciesla, U.; Demuth, D. G.; Feng, P.; Gier, T. E.; Sieger, P.; Firouzi, A.; Chmelka, B. F.; Schüth, F.; Stucky, G. D. *Chem. Mater.* **1994**, *6*, 1176.

[9] Chen, C.-Y.; Li, H.-X.; Davis, M. E. *Micropor. Mater.* **1993**, *2*, 17.

[10] Kim, S. S.; Zhang, W.; Pinnavaia, T. J. *Science* **1998**, *282*, 1302.

[11] Knowles, J. A.; Hudson, M. J. *J. Chem. Soc. Chem. Commun.* **1995**, 2083.

[12] Ward, D. A.; Ko, E. I. *Langmuir* **1995**, *11*, 369.

[13] Murrell, L. L. *Catal. Today* **1997**, *35*, 225.

[14] Elder, S. H.; Gao, Y.; Li; X.; Liu, J.; McCready, D. E.; Windisch, Jr., C. F. *Chem. Mater.* **1998**, *10*, 3140.

[15] http://www.basf.com/

[16] Gao, X.; Bare, S. R.; Fierro, J. L. G.; Banares, M. A.; Wachs, I .E. *J. Phys. Chem. B* **1998**, *102*, 5653.

[17] Delgass, W. N.; Haller, G. L.; Kellerman, R.; Lunsford, J. H. *Spectroscopy in Heterogeneous Catalysis*; Academic Press: New York, 1979.

[18] Barton, D. G.; Shtein, M.; Wilson, R. D.; Soled, S. L.; Iglesia, E. *J. Phys. Chem. B* **1999**, *103*, 630.

[19] Logie, V.; Wehrer, P.; Katrib, A.; Maire, G. *J. Catal.* **2000**, *189*, 438.

[20] Ding, X.; Wu, G. *Spectrochim. Acta A* **1995**, *51*, 709.

[21] (a) Ostromecki, M. M.; Burcham, L. J.; Wachs, I. E.; Ramani, N.; Ekerdt, J. G. *J. Mol. Catal. A: Chem.* **1998**, *132*, 43. (b) Horsley, J. A.; Wachs, I. E.; Brown, J. M.; Via, G. H.; Hardcastle, F. D. *J. Phys. Chem.* **1987**, *91*, 4014.

[22] Ward, D. A.; Ko, E. I. *Chem. Mater.* **1993**, *5*, 956.

[23] Stefanic, G.; Music, S.; Grzeta, B.; Popovic, S.; Sekulic, A. *J. Phys. Chem. Solids* **1998**, *59*, 879.

[24] Srinivasan, R.; Harris, M. B.; Simpson, S. F.; DeAngelis, R. J.; Davis, B. H. *J. Mater. Res.* **1988**, *3*, 787.

[25] Wachs, I. E. *Catal. Today* **1996**, *27*, 437.

[26] Vuurman, M. A.; Wachs, I. E. *J. Phys. Chem.* **1992**, *96*, 5008.

[27] Ramis, G.; Cristiani, C.; Elmi, A. S.; Villa, P.; Busca, G. *J. Mol. Catal.* **1990**, *61*, 319.

[28] (a) Tanabe, K.; Misono, M.; Ono, Y.; Hattori, H. *New Solid Acids and Bases: Their Catalytic Properties, Studies in Surface Science and Catalysis*, Vol. 51; Kodansha: Tokyo, 1989. (b) Corma, A. *Chem. Rev.* **1995**, *95*, 559.

[29] Ryoo, R.; Kim, J. M.; Ko, C. H.; Shin, C. H. *J. Phys. Chem.* **1996**, *100*, 17718.

[30] McGrath, K. M.; Dabbs, D. M.; Yao, N.; Aksay, I. A.; Gruner, S. M. *Science* **1997**, *277*, 552.

[31] Bagshaw, S. A.; Prouzet, E.; Pinnavaia, T. J. *Science* **1995**, *269*, 1242.

[32] (a) Zhao, D.; Feng, J.; Huo, Q.; Melosh, N.; Fredrickson, G. H.; Chmelka, B. F.; Stucky. G. D. *Science* **1998**, *279*, 548. (b) Zhao, D.; Huo, Q.; Feng, J.; Chmelka, B. F.; Stucky, G. D. *J. Am. Chem. Soc.* **1998**, *120*, 6024.

[33] Karakonstantis, L.; Bourikas, K.; Lycourghiotis, A. *J. Catal.* **1996**, *162*, 295.

[34] Carrier, X.; d'Espinose de la Caillerie, J.-B.; Lambert, J.-F.; Che, M. *J. Am. Chem. Soc.* **1999**, *121*, 3377.

[35] Chang, L. L. Y.; Scroger, M. G.; Phillips, B. *J. Am. Ceram. Soc.* **1967**, *50*, 211.

[36] Scheithauer, M.; Grasselli, R. K.; Knözinger, H. *Langmuir* **1998**, *14*, 3019.

[37] Naito, N.; Katada, N.; Niwa, M. *J. Phys. Chem. B* **1999**, *103*, 7206.

[38] Landry, M. R.; Coltrain, B. K.; Landry, C. J. T.; O'Reilly, J. M. *J. Polym. Sci. Part B: Polym. Phys.* **1995**, *33*, 637.

[39] Klug, H. P.; Alexander, L. E. *X-Ray Diffraction Procedures for Polycrystalline and Amorphous Materials*; John Wiley & Sons: New York, 1954.

[40] Gimblett, G.; Rahman, A. A.; Sing, K. S. W. *J. Chem. Tech. Biotechnol.* **1980**, *30*, 51.

[41] Torralvo, M. J., Alario, M. A., Soria, J., J. Catal., 86, 473-476, 1984.

[42] Livage, J.; Doi, K.; Mazières, C. *J. Am. Ceram. Soc.* **1968**, *51*, 349.

[43] (a) Pope, M. T. *Heteropoly and Isopoly Oxometallates*; Springer-Verlag: Berlin, 1983. (b) Pettersson, L., in *Polyoxometallates*; Pope, M. T., Müller, A., Eds.; Kluwer Academic: Dordrecht, 1994; p. 27. (c) Baes, Jr., C. F.; Mesmer, R. E. *The Hydrolysis of Cations*; Wiley: New York, 1976.

[44] Kim, D. S.; Ostromecki, M.; Wachs, I. E. *J. Mol. Catal. A: Chem.* **1996**, *106*, 93.

[45] Hino, M.; Arata, K. *J. Chem. Soc. Chem. Commun.* **1988**, 1259.

[46] Bigey, C.; Hilaire, L.; Maire, G. *J. Catal.* **1999**, *184*, 406.

[47] (a) Santiesteban, J. G.; Vartuli, J. C.; Han, S.; Bastian, R. D.; Chang, C. D. *J. Catal.* **1997**, *168*, 431. (b) Santiesteban, J. G.; Calabro, D. C.; Borghard, W. S.; Chang, C. D.; Vartuli, J. C.; Tsao, Y. P.; Natal-Santiago, M. A.; Bastian, R. D. *J. Catal.* **1999**, *183*, 314.

[48] Barton, D. G.; Soled, S. L.; Meitzner, G. D.; Fuentes, G. A.; Iglesia, E. *J. Catal.* **1999**, *181*, 57.

[49] Parks, G. A. *Chem. Rev.* **1965**, *65*, 177.

[50] Hastings, J. J.; Howarth, O. W. *J. Chem. Soc. Dalton Trans.* **1992**, *2*, 209.

[51] Pérez-Maqueda, L. A.; Matijevic, E. *J. Mater. Res.* **1997**, *12*, 3286.

[52] Ananthapadmanabhan, K. P.; Goddard, E. D. *Langmuir* **1987**, *3*, 25.

[53] Bailey, Jr., F. E.; Callard, R. W. *J. Appl. Polym. Sci.* **1959**, 1, 56.

[54] Okada, T. *Analyst* **1993**, *118*, 959.

[55] Becher, P.; Birkmeier, R. L. *J. Am. Oil Chem. Soc.* **1964**, *41*, 169.

[56] (a) Holland, B. T.; Blanford, C. F.; Stein, A. *Science* **1998**, *281*, 538. (b) Holland, B. T.; Blanford, C. F.; Do, T.; Stein, A. *Chem. Mater.* **1999**, *11*, 795.

[57] (a) Velev, O. D.; Jede, T. A.; Lobo, R. F.; Lenhoff, A. M. *Nature* **1997**, *389*, 447. (b) Yin, J. S.; Wang, Z. L. *Adv. Mater.* **1999**, *11*, 469. (c) Subramania, G.; Constant, K.; Biswas, R.; Sigalas, M. M.; Ho, K.-M. *Appl. Phys. Lett.* **1999**, 74, 3933.

[58] Yang, P.; Deng, T.; Zhao, D.; Feng, P.; Pine, D.; Chmelka, B. F.; Whitesides, G. M.; Stucky, G. D. *Science* **1998**, *282*, 2244.

[59] Hiemenz, P. C.; Rajagopalan, R. *Principles of Colloid and Surface Chemistry*, 3rd Ed.; Marcel Dekker: New York; 1997.

Chapter 5. Mesoporous Tungstated Metal Oxide Systems

5.1 Introduction

The colloid/surfactant templating synthesis route to mesoporous tungstated zirconia (WZr-TMS14) is a new approach to bicomponent mesoporous materials. The inorganic framework of WZr-TMS14 is nanocrystalline, which comes from the use of the zirconia colloid nanoparticles as a precursor. According to the synthesis mechanism, positively-charged colloidal particles are capable of participating in the templating of a mesoporous material. In this chapter, this synthesis method is extended to inorganic colloids of other compositions, to successfully derive mesoporous tungstated titania alumina.

5.2 Experimental Methods

The preparation of mesoporous tungstated titania (WTi-TMS14) and tungstated alumina (WAl-TMS14) follows the method for WZr-TMS14. A solution of 2.1 M Ti^{4+} was prepared by adding 10 ml of $TiCl_4$ to 43.6 ml of water at 0 °C under flowing argon. Aliquots of this stock solution were diluted to 0.44 M Ti^{4+} with deionized water or with KOH solutions of varying concentrations (0.5, 1.0, 1.5 M). A 2.8 M Al^{3+} solution was prepared from dissolving $AlCl_3 \cdot 6H_2O$ in deionized water. A 0.45 M Al^{3+} solution was prepared using $AlCl_3 \cdot 6H_2O$ and adding NaOH at an Al^{3+}/OH^- molar ratio of 2.2. The solution became cloudy immediately, but cleared up after 10 days of stirring at room temperature. Amounts of metal precursor that gave a calculated weight of metal oxide equivalent to 1.62 g (the total amount of ZrO_2 used in a synthesis batch of WZr-TMS14) was used for all syntheses. Samples were calcined at 250 °C (ramp = 1 °C/min, soak time = 1 hr) or at 300 °C (ramp = 0.8 °C/min, soak time = 1 hr) either in a box furnace, or in a tube furnace under flowing nitrogen. Characterization results were collected in the same manner as previously described for WZr-TMS14 (Chapter 4.2). In addition, UV-Vis absorption spectra of $TiCl_4$ solutions/mixtures were collected on a Shimadzu UV-2401PC spectrophotometer.

5.3 Results and Discussion

5.3.1 Preparation of Colloid Nanoparticles of Titania

As colloidal titania was not commercially available, initial efforts focussed on its preparation. Colloid nanoparticles of titania were synthesized similar to previously published

synthesis routes [1,2]. Kormann *et al.* prepared a stable 5.0×10^{-3} M $TiCl_4$ solution and showed that colloidal titania with a particle size of 2.4 nm was formed [1]. They reported that a higher concentration of 3.6×10^{-2} M $TiCl_4$ solution led to precipitation of anatase titania after several hours of aging. Our 2.1 M $TiCl_4$ solution was found to have much greater long-term stability. No precipitation was observed after 1 month of stirring at room temperature, similar to what Kim *et al.* found in their TiO_2 precipitation studies [2]. Dilution of this stock solution to a concentration of 0.44 M led to a metastable colloid solution (Figure 5.1).

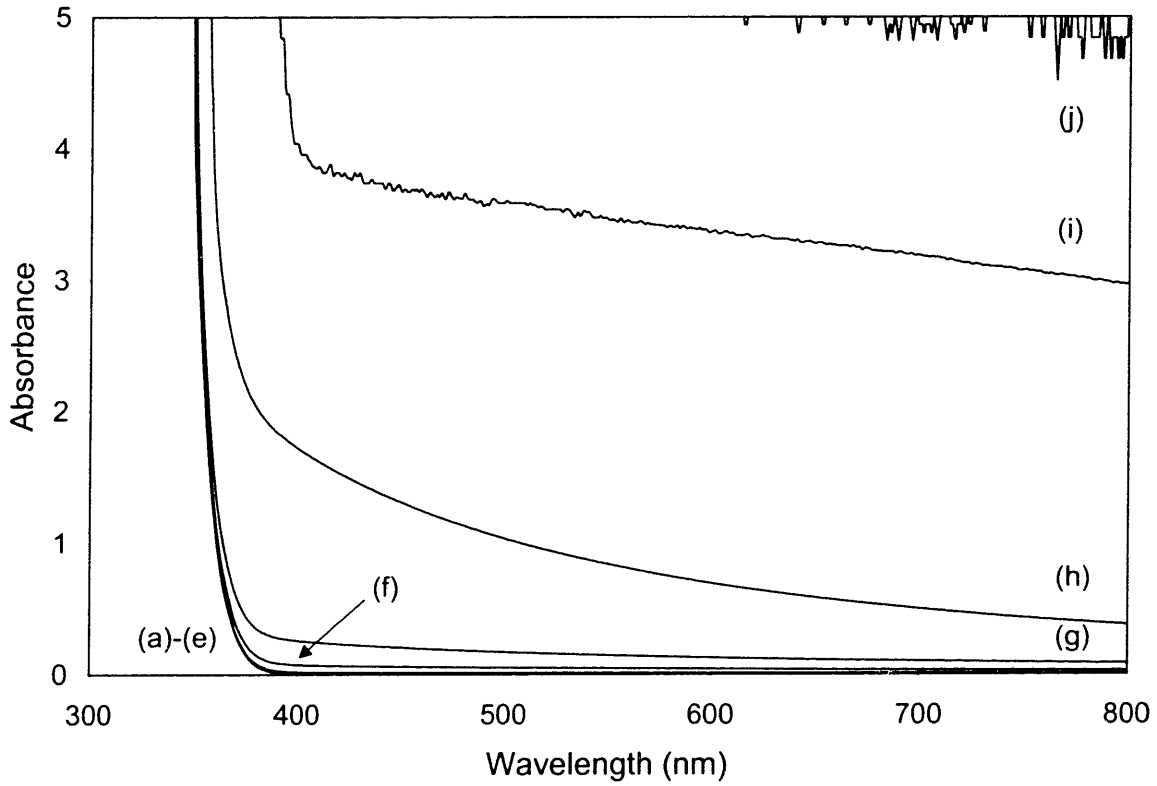

Figure 5.1. UV-Vis absorption spectra of TiO_2 colloid solution (total concentration = 0.44 M Ti^{4+}) at various times (hr): (a) 0, (b) 25, (c) 47, (d) 52, (e) 60, (f) 71, (g) 78, (h) 90, (i) 105, and (j) 129.

This 0.44 M $TiCl_4$ solution exhibited strong absorbance below 400 nm, which is attributed to absorption by TiO_2 colloids, as Kormann *et al.* found for their anatase TiO_2 colloid system [1]. This TiO_2 colloid solution remained unchanged for 60 hr before exhibiting an increase in UV-Vis absorbance at wavelengths > 350 nm. Visually, the clear TiO_2 colloid solution became cloudy after 60 hr, and was completely opaque after 129 hr,

characterized by the complete absorption of UV-Vis radiation between 300-800 nm (Figure 5.1(j)). The opacity arose from the formation and suspension of a very fine powder precipitate via homogeneous precipitation. The precipitate was the rutile phase of TiO_2 (Figure 5.2(a)), and Scherrer's analysis of the (110) rutile peak gave a grain size of 4.6 nm (Table 5.1). This is another method of preparing nanocrystalline rutile, which can be synthesized via homogeneous precipitation of titanium salts [2] or via hydrothermal treatment of titanium alkoxide solutions [4]. Titania colloid solutions that are stable against aggregation have been reported recently, in which the nanoparticle surfaces were passivated with organic complexation agents [5-6].

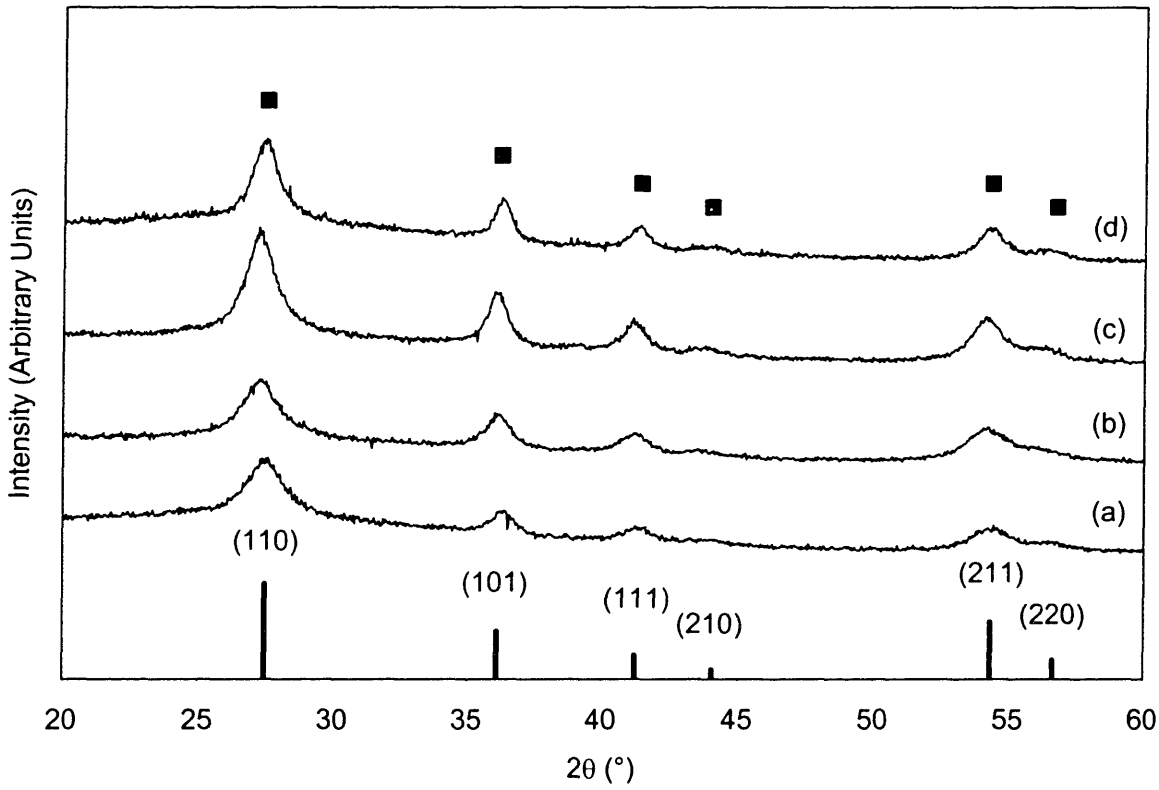

Figure 5.2. XRD of TiO_2 powder precipitated from 0.44 M $TiCl_4$ solution prepared with (a) water and KOH solutions with concentrations of (b) 0.5 M, (c) 1.0 M, and (d) 1.5 M. Symbols: ■ = rutile TiO_2 (#21-1276).

The change in the TiO_2 colloid solution as a function of aging time can be tracked by the absorbance at 400 nm (Figure 5.3). After 129 hr of aging, the absorbance increased to the detection limit of 5.0 (Figure 5.3(a)). The pH of this solution was <1. The sigmoidal shape of

the curve is typical of precipitation processes, whereby precipitation begins after an induction period, and accelerates to a maximum value before slowing down and terminating [7]. The preparation of colloidal dispersions, in which the size of monodisperse particles range between 10-100 nm, through homogeneous precipitation has been well-studied [8]. Particle formation is initiated with the nucleation of primary particles, and followed by the growth and/or aggregation of these primary particles [9]. The non-aggregated primary particles of TiO_2 are desired in our colloid/surfactant templating synthesis.

Table 5.1. Grain size of rutile TiO_2 prepared from different KOH concentrations.

KOH Precursor Concentration (M)	Final KOH Concentration (M)	Grain Size (nm)
0.0	0.0	4.6
0.5	0.4	5.1
1.0	0.8	6.2
1.5	1.2	7.0

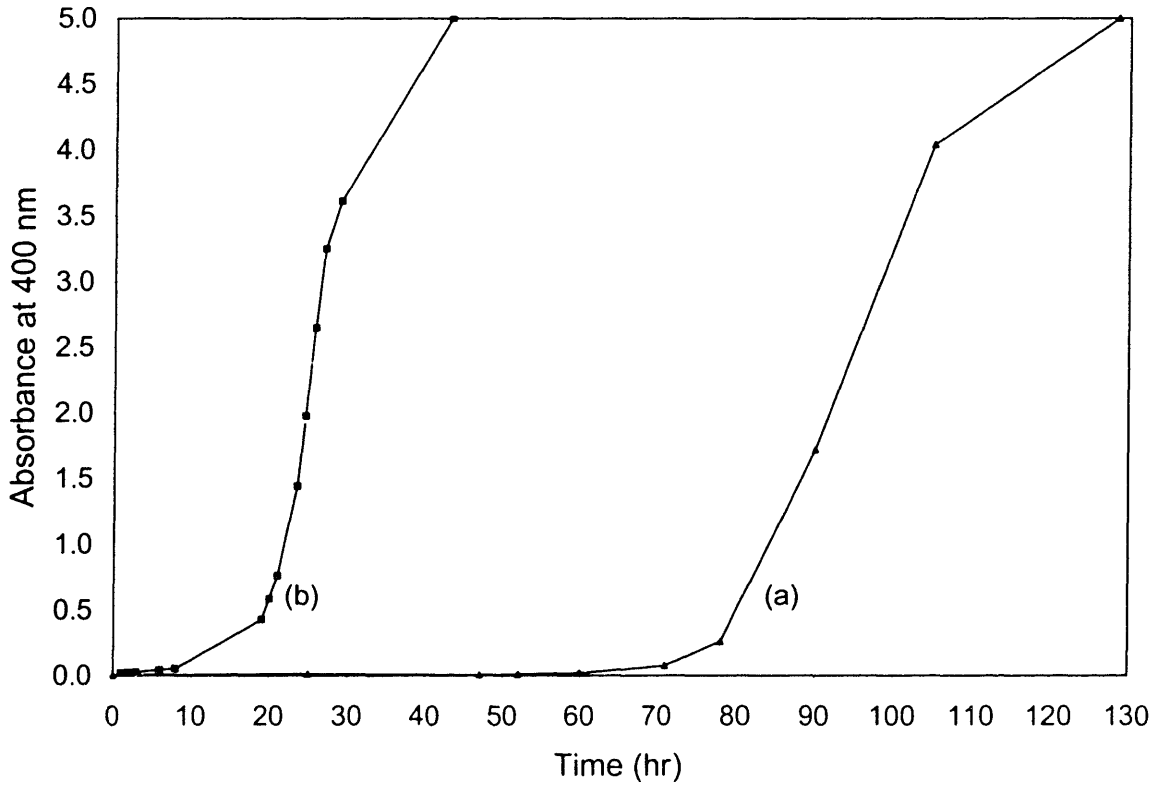

Figure 5.3. UV-Vis absorption-time profiles of TiO_2 colloid solution (0.44 M $TiCl_4$) prepared from 2.1 M $TiCl_4$ solution (a) with water or (b) with 1.0 KOH solution.

Colloidal TiO_2 (0.44 M $TiCl_4$) was also prepared by adding a KOH solution of varying concentrations to the 2.1 M $TiCl_4$ stock solution; the final pH of these colloidal sols was <1. Representive of TiO_2 sols prepared with other base concentrations, colloidal TiO_2 sol prepared with 1.0 M KOH was kinetically less stable than the sol prepared without KOH (Figure 5.3(b)). Precipitation was complete by 43 hr instead of 129 hr, also resulting in rutile TiO_2 particles (Figure 5.2(c)). The grain size of rutile TiO_2 increased with higher concentrations of KOH solution, suggesting that, prior to precipitation, the TiO_2 colloid particles in solution also scaled with increasing KOH concentrations (Table 5.1).

TEM showed that the TiO_2 precipitates typically consisted of large particles (~100 nm) with a rice-like particle morphology, resulting from an aggregation growth process [3]. Figure 5.4(a) shows the precipitated TiO_2 particles resulting from the 1.5 M KOH solution, and Figure 5.4(b) shows the individual rutile grains comprising the particles.

There is further indirect evidence that the TiO_2 colloidal particles increased in size with base concentration. The absorption edge of the UV-Vis spectrum of colloidal TiO_2 sol is displaced to a higher wavelength when prepared with KOH (Figure 5.5). This red shift is characteristic of quantum dots, or semiconducting nanoparticles, growing in particle size [1,10-12].

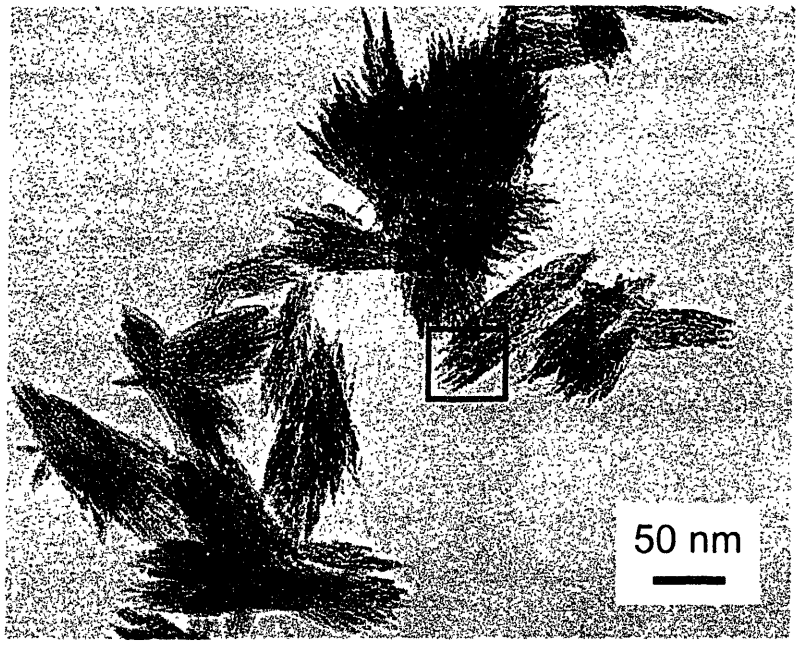

Figure 5.4. (a) TEM image of TiO_2 powder precipitated from a 0.44 M $TiCl_4$ / 1.2 M KOH solution.

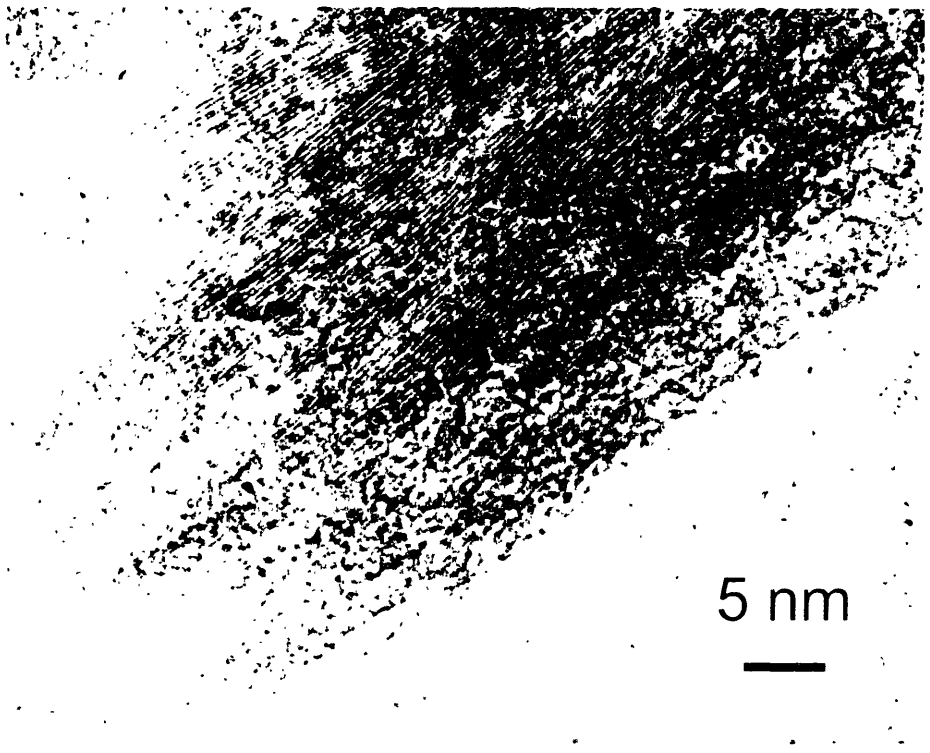

Figure 5.4. (b) HRTEM image of the indicated region of the rutile TiO_2 particle.

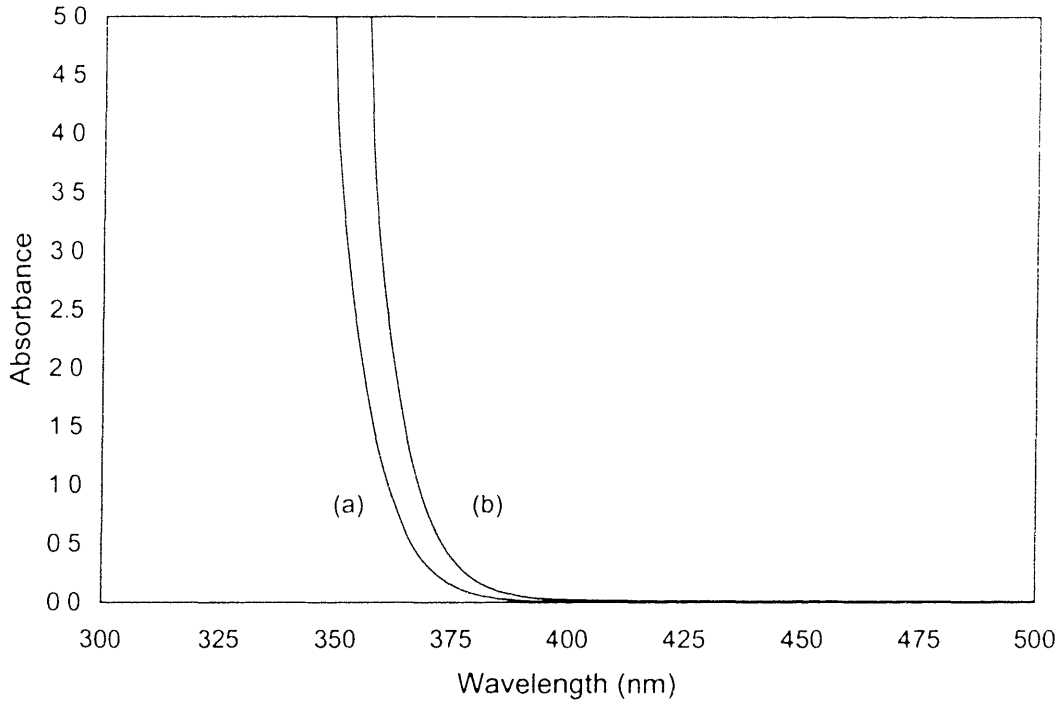

Figure 5.5. UV-Vis absorption spectra of TiO_2 colloid solution (0.44 M $TiCl_4$) prepared from 2.1 M $TiCl_4$ solution with (a) water and (b) 1.0 M KOH solution.

5.3.2 Preparation of Mesoporous Tungstated Titania (WTi-TMS14)

Colloidal TiO_2 was prepared without KOH and with KOH solutions of different concentrations (0.5 M, 1.0 M, and 1.5 M), and then used in the preparation of WTi-TMS14. Figure 5.6 shows the SAXS patterns of the resultant materials. The Bragg spacing of the SAXS peak increased in value with KOH concentration of the colloidal TiO_2 (Table 5.2). This would be consistent with the framework walls containing larger TiO_2 colloidal nanoparticles, as a thicker wall increases the Bragg spacing given the same pore or micelle size. The Bragg spacing did not scale with rutile TiO_2 grain size, however (Table 5.1). There is also likely a pH effect on the Bragg spacing of the supramolecular-templated mesostructure as the proposed charge interactions would be sensitive to synthesis pH. The pH in all final mixtures were <1. After calcination at 250 °C, the WTi-TMS14 materials prepared with 1.0 M and 1.5 M KOH appeared to retain a mesostructure, as characterized by a SAXS peak with a smaller Bragg spacing (Figure 5.7). Temperatures of 250 °C are needed to volatilize the copolymer surfactant, as found for WZr-TMS14.

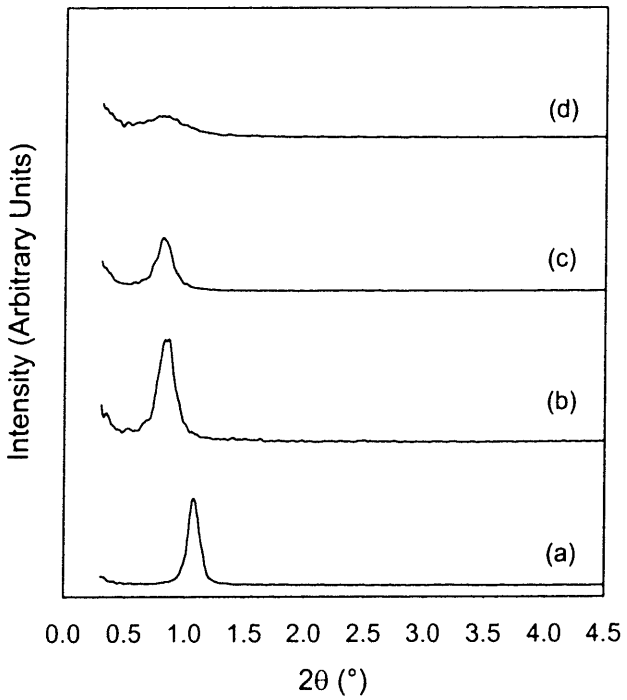

Figure 5.6. SAXS patterns of as-synthesized WTi-TMS14 prepared with (a) 0 M, (b) 0.5 M, (c) 1.0 M, and (d) 1.5 M KOH solutions.

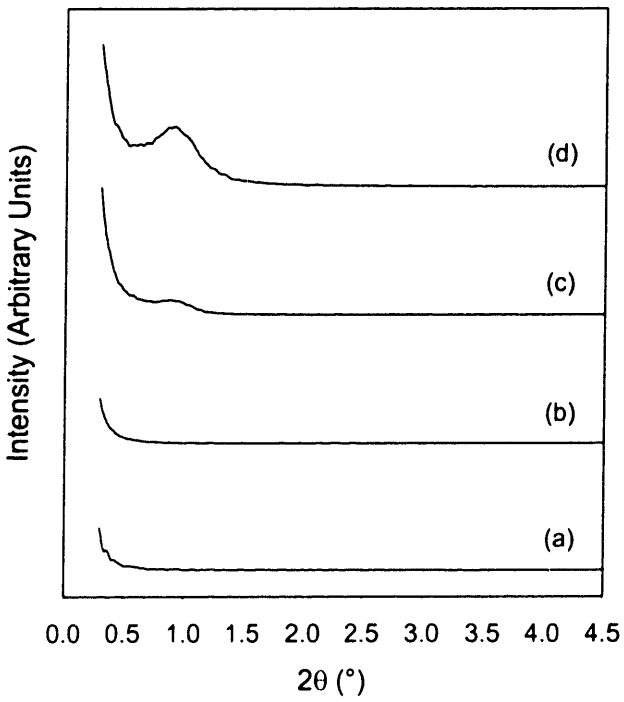

Figure 5.7. SAXS patterns of 250 °C-calcined WTi-TMS14 prepared with (a) 0 M, (b) 0.5 M, (c) 1.0 M, and (d) 1.5 M KOH solutions.

The BET surface areas of the 250 °C-calcined WTi-TMS14 materials are shown in Table 5.2. For samples prepared with water or 0.5 M KOH, the loss of the mesostructure after calcination led to non-porous materials ≤ 2 m^2/g. WTi-TMS14 prepared with 1.0 M or 1.5 M KOH solutions had a much higher surface area and a Type IV nitrogen adsorption isotherm, indicating some mesoporosity (Figure 5.8). The sample prepared with 1.0 M KOH had a surface area of 15 m^2/g after calcination; its nitrogen adsorption isotherm suggested partial pore collapse after template removal.

Table 5.2. Physical properties of WTi-TMS14 prepared with different KOH solutions.

Concentration of KOH (M)	Bragg Spacing (nm) Uncalcined	Calcined	Surface Area (m^2/g)	Pore Size (nm)
0.0	8.3	—	<1	—
0.5	10.3	—	2	—
1.0	10.8	9.8	15	4.4
1.5	10.8	9.8	126	3.9

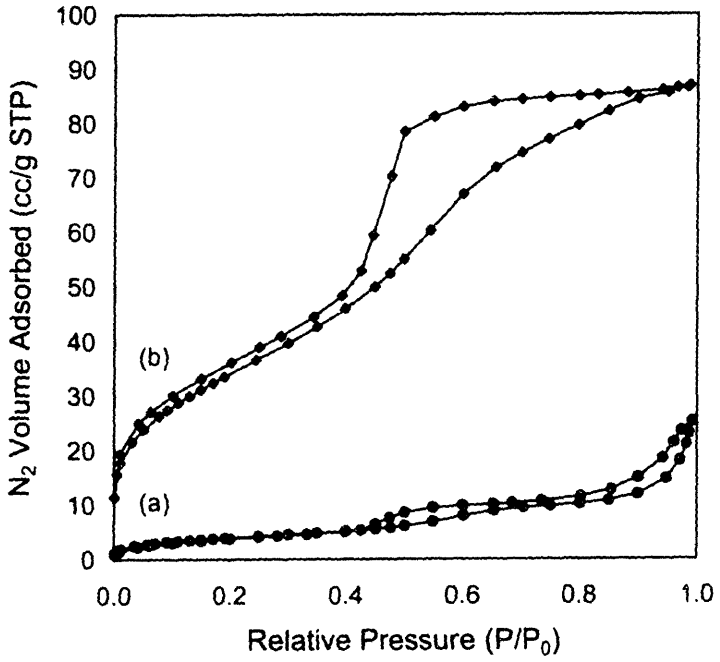

Figure 5.8. Nitrogen adsorption isotherms of 250 °C-calcined WTi-TMS14 prepared with (a) 1.0 M and (b) 1.5 M KOH solutions.

As-synthesized WTi-TMS14 prepared with no KOH was did not exhibit XRD peaks for rutile TiO_2 before calcination and after calcination at 250 °C (Figures 5.9(a)-(b), respectively). Representative of materials derived with base solutions, WTi-TMS14 prepared with 1.5 M KOH solution also did not exhibit XRD peaks for rutile TiO_2 before calcination (Figure 5.9(c)). After calcination at 250 °C, a small broad XRD peak emerged and was identified as anatase TiO_2 (Figure 5.9(d)). Calculated from this (101) anatase peak, the grain size was 1.4 nm, and increased to 1.6 nm, after calcination at 400 °C (Figure 5.9(e)).

Calcination at 600 °C led to a larger grain size of 6.3 nm and to the appearance of higher-order anatase XRD peaks and a mixture of hydrogen tungsten oxides ($H_{0.23}WO_3$, $H_{0.33}WO_3$), suggesting a breakdown of the WTi-TMS14 material (Figure 5.9(f)). No rutile TiO_2 was found at any calcination temperature.

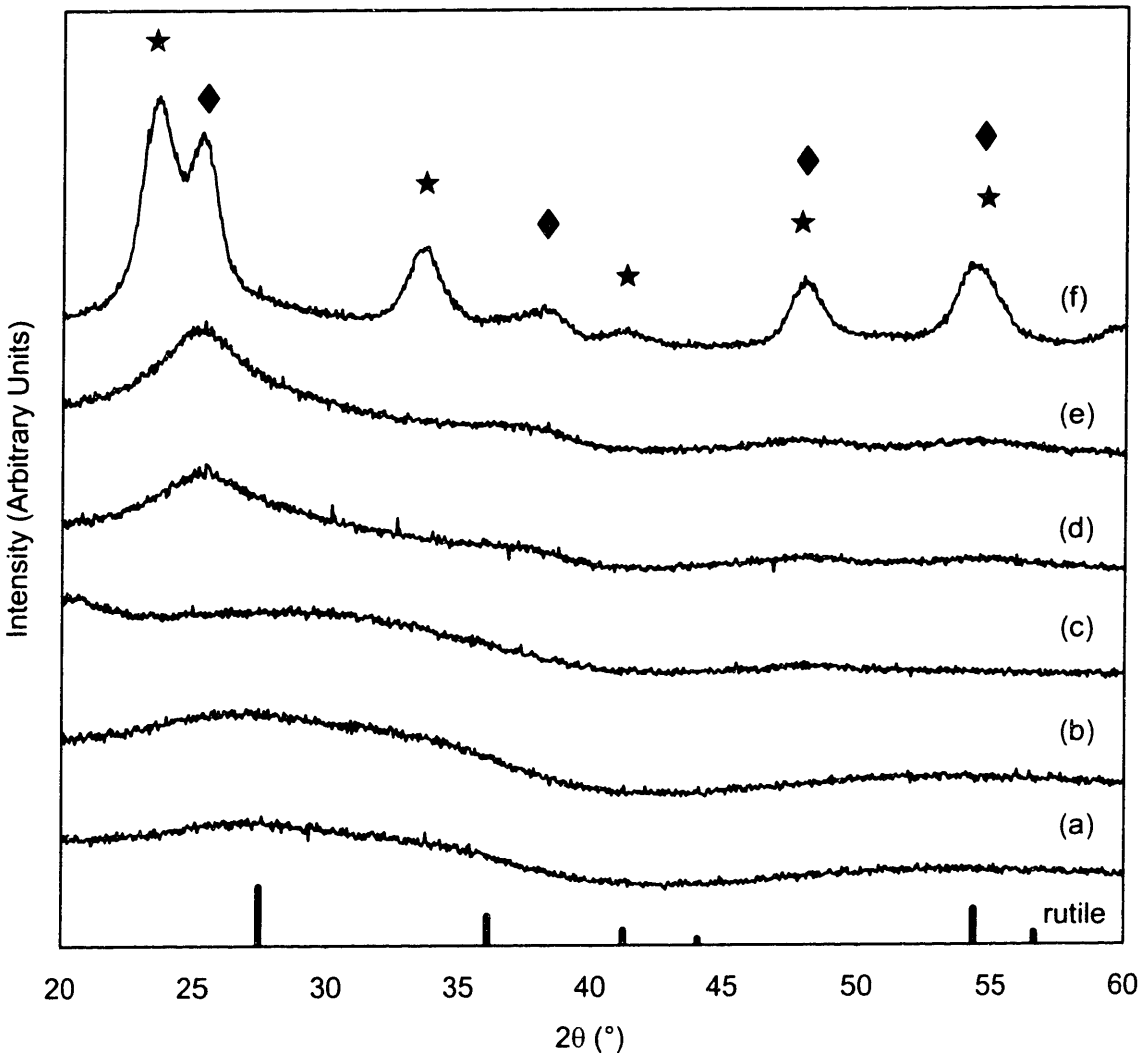

Figure 5.9. XRD of WTi-TMS14 prepared with (a,b) 0 M and (c-f) 1.5 M KOH solutions, (a,c) before calcination and after calcination at (b,d) 250 °C, (e) 400 °C and (f) 600 °C. Symbols: ★ = mixture of hydrogen tungsten oxides; ♦ = anatase TiO_2 (#21-1272).

As indicated earlier, WTi-TMS14 prepared with 1.5 M KOH solution and calcined at 250 °C under nitrogen was mesoporous (Figure 5.8). Calcination at 400 °C under air led to a material with the same pore size but with a higher surface area (Table 5.3). This may be attributed to the loss of residual carbon, which adds to the overall weight but not the total surface area. WTi-TMS14 calcined at 250 °C, 400 °C, and 600 °C all exhibited Type IV nitrogen adsorption isotherms with a hysteresis loop of type H2. However, the 600 °C-calcined material showed an isotherm shifted significantly to higher relative pressures (Figure 5.10), resulting in an increase in the calculated pore size (Figure 5.11). The calcination at 600

°C led to a partial collapse of the mesoporous framework with the loss in surface area and in the SAXS pattern (Table 5.3).

Table 5.3. Physical properties of WTi-TMS14 prepared with 1.5 M KOH and calcined at various temperatures.

Calcination Temperature (°C)	Bragg Spacing (nm)	Surface Area (m^2/g)	Pore Size (nm)
250	9.8	126	3.9
400	9.2	168	4.3
600	—	67	8.1

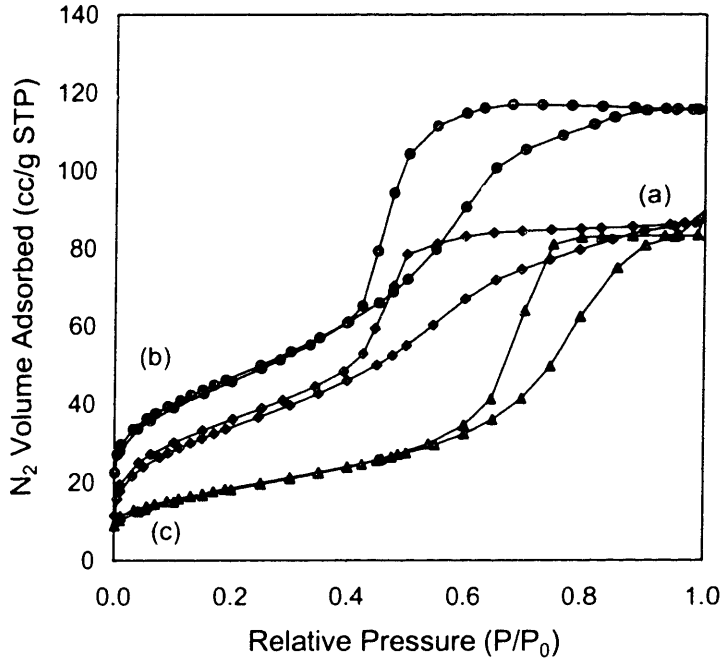

Figure 5.10. Nitrogen adsorption isotherms of WTi-TMS14 calcined at (a) 250 °C under nitrogen, (b) 400 °C under air, and (c) 600 °C under air.

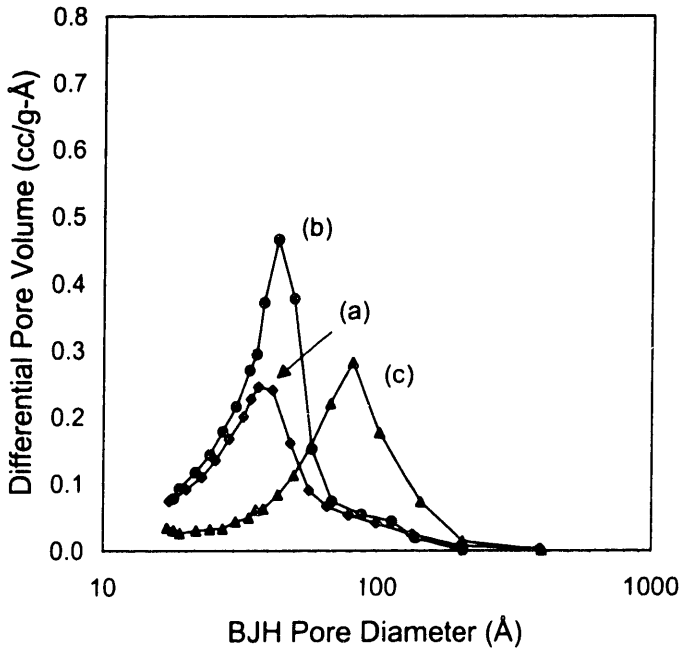

Figure 5.11. Pore size distribution of WTi-TMS14 calcined at (a) 250 °C under nitrogen, (b) 400 °C under air, and (c) 600 °C under air.

The mesoporous structure of 400 °C-calcined WTi-TMS14 prepared with 1.5 M KOH solution is illustrated by TEM (Figure 5.12). The pores were about 4-6 nm in diameter, and arranged in a disordered fashion. The pore wall thickness was measured to be 2-4 nm, on the same order as the anatase TiO_2 grain size of 1.6 nm, although smaller than the rutile TiO_2 grains in the powder precipitated from the precursor sol (Table 5.1). The electron diffraction pattern showed several rings, indicative of nanocrystallinity (Figure 5.12, inset). Three rings were observed and assigned to the (101), (004) and (200) sets of planes of anatase TiO_2. A further magnification of the boxed area in Figure 5.12 revealed the nanocrystalline grains of anatase TiO_2 (Figure 5.13).

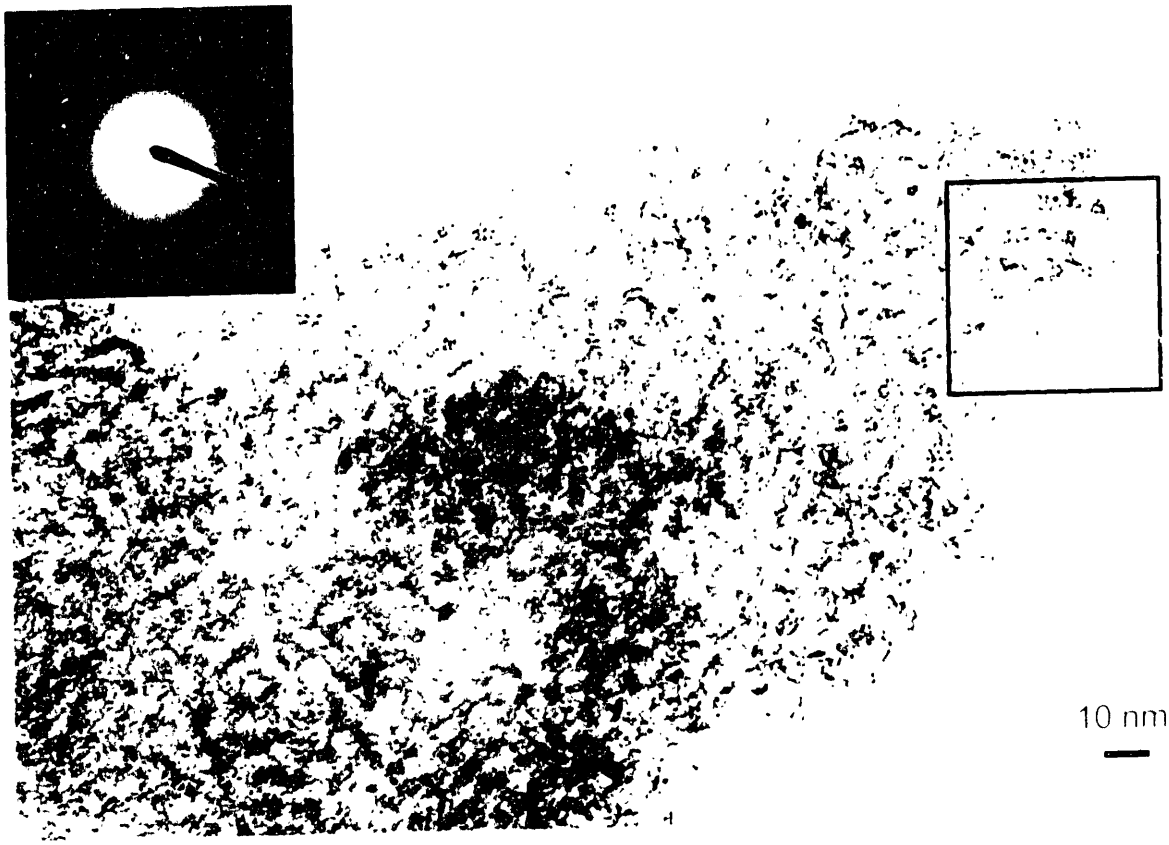

Figure 5.12. TEM image of 400 °C-calcined Ti-TMS14 prepared with 1.5 M KOH solution. Inset: SAED pattern.

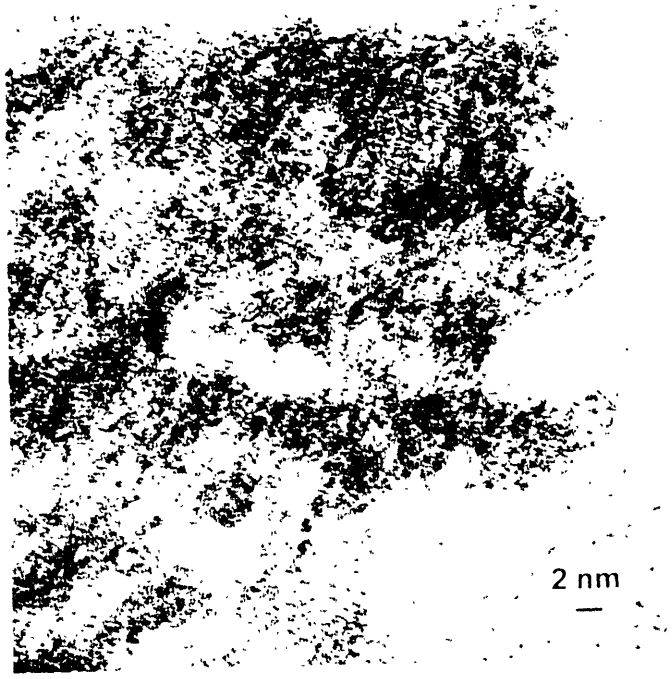

Figure 5.13. HRTEM image of 400 °C-calcined Ti-TMS14.

5.3.3 Preparation of Tungstated Alumina WAl-TMS14

Colloidal alumina refers to a solution of $[AlO_4Al_{12}(OH)_{24}(H_2O)_{12}]^{7+}$ ("Al_{13}") polycations, which are ~1 nm in size [13]. Its preparation was based on a well-known synthesis route, but the formation of Al_{13} is rather sensitive to synthesis conditions, e.g. Al^{3+}/OH^- ratio, rate of base addition, and mixing rate. While the Al_{13} species is well-defined, a freshly-prepared colloidal alumina solution contains unreacted Al^{3+} cations in addition to Al_{13} polycations. Furthermore, the Al_{13} polycation itself is metastable in solution [14]. Thus it is unlikely that our colloidal alumina solution contains solely Al_{13}, and interactions with the surfactant and/or the metatungstate could involve Al^{3+} as well.

WAl-TMS14 prepared with colloidal alumina was found to be mesostructured, displaying a small, broad SAXS peak (Figure 5.14). After calcination at 300 °C, WAl-TMS14 retained its mesostructure with the SAXS peak shifting slightly to a higher 2θ angle, corrsponding to a reduction in Bragg spacing from 14.0 nm to 12.1 nm. Calcination at 400 °C reduced the Bragg spacing further to 10.9 nm. Calcination at 600 °C led to the loss of the SAXS pattern, suggesting the breakdown of the mesoporous structure. The Bragg values were greater than those of WZr-TMS14 and WTi-TMS14; either the templating micelles or templated pores were larger or the framework walls were thicker.

WAl-TMS14 did not exhibit XRD peaks of alumina, before and after calcination at 300 °C and at 400 °C (Figure 5.15). The NaCl impurity found in the sample was a byproduct of NaOH and $AlCl_3$. Calcination of WAl-TMS14 at 600 °C led to the appearance of WO_3 and $Na_2W_2O_7$ XRD peaks, indicating the onset of crystallization of the material (Figure 5.15(d)).

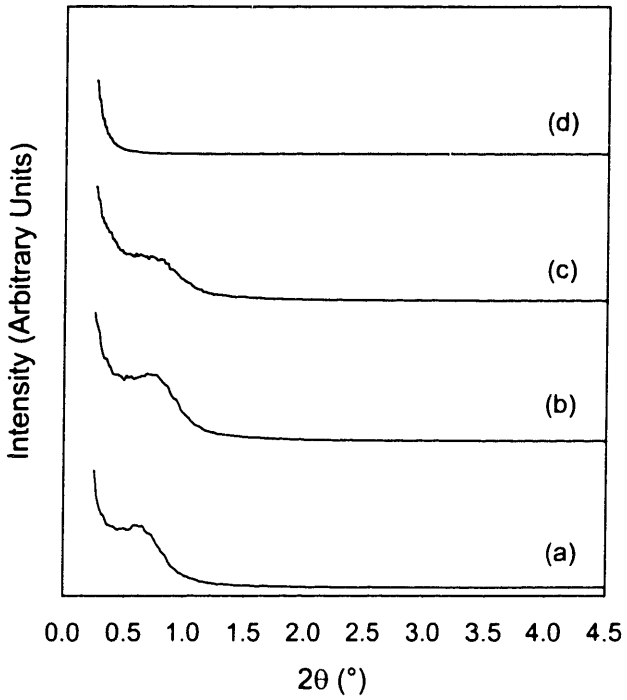

Figure 5.14. SAXS patterns of WAl-TMS14 (a) before and after calcination at (b) at 300 °C in nitrogen, (c) 400 °C in air, and (d) 600 °C in air.

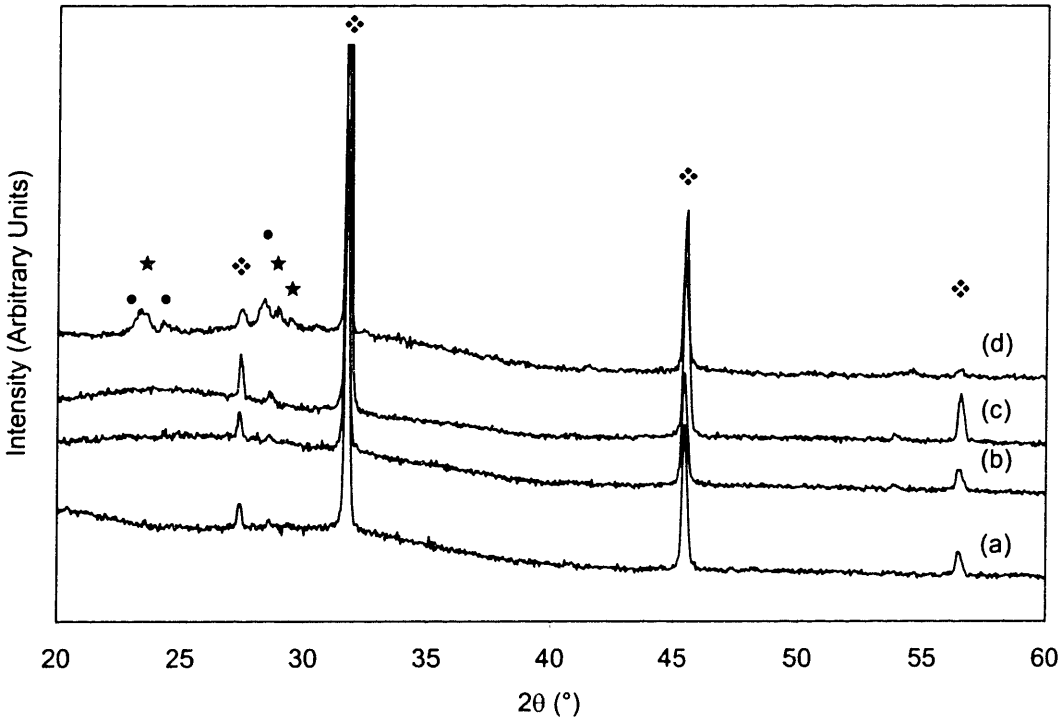

Figure 5.15. XRD of WAl-TMS14 (a) before and after calcination at (b) 300 °C under nitrogen, (c) 400 °C under air, and (d) 600 °C under air. Symbol: • = WO_3 (#32-1395); ★ = $Na_2W_2O_7$ (#32-1185); ❖ = NaCl (#05-0628).

WAl-TMS14 calcined at 300 °C had a high BET surface area of 130 m^2/g and a Type IV nitrogen adsorption isotherm (Figure 5.16(a)). Its BJH pore size distribution (based on adsorption branch) was centered at 6.7 nm, which is larger than those of WZr-TMS14 and WTi-TMS14 (Figure 5.17(a)). This is consistent with the larger Bragg spacing of WAl-TMS14. Although the same surfactant template was used, it is not surprising that the microstructure and physical properties for the various mesoporous tungstated metal oxide systems are different since the solution chemistry of various inorganic colloids and the resulting supramolecular templating chemistry might vary substantially.

Calcination at 400 °C led to a similar WAl-TMS14 material, with a surface area of 134 m^2/g and a pore size of 6.7 nm (Figures 5.16(b) and 5.17(b)). Calcination at 600 °C led to a nonporous material with a negligible surface area of ~1 m^2/g, indicating complete collapse of the mesoporous structure (Figures 5.16(c) and 5.17(c)).

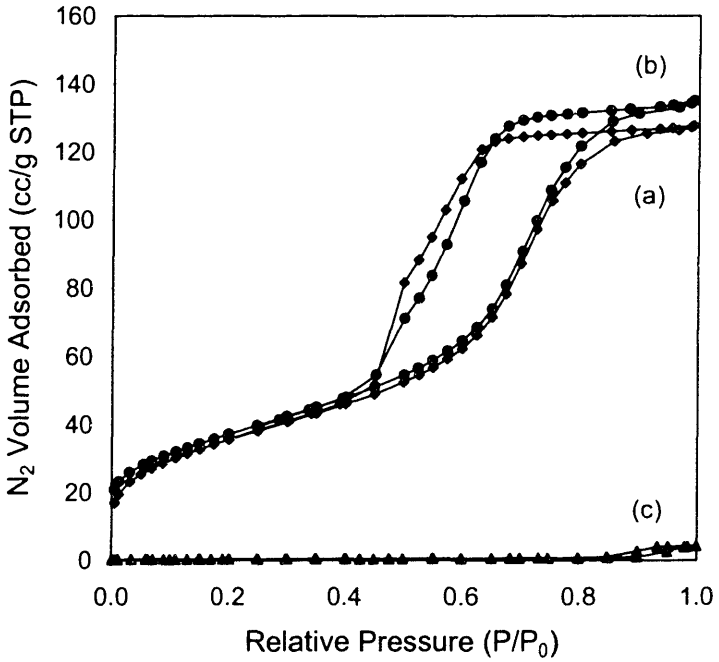

Figure 5.16. Nitrogen adsorption isotherm of WAl-TMS14 calcined at (a) 300 °C under nitrogen, (b) 400 °C under air, and (c) 600 °C under air.

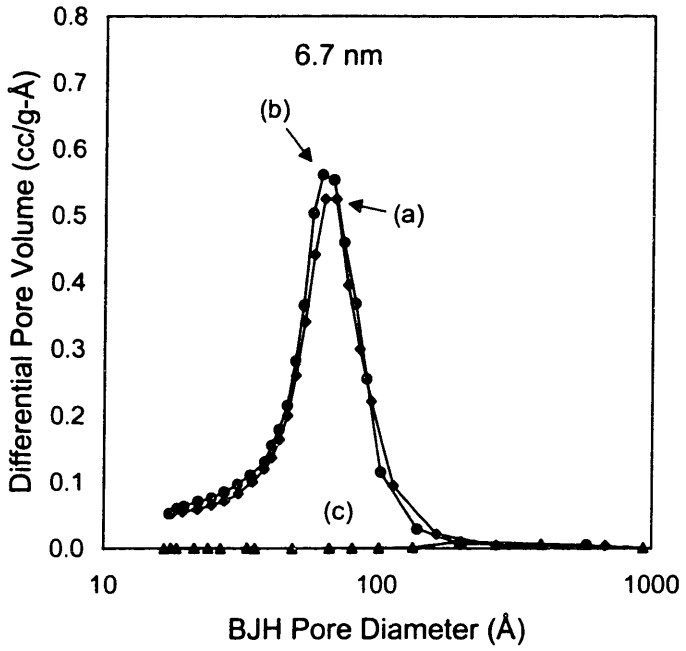

Figure 5.17. Pore size distribution of WAl-TMS14 calcined calcined at (a) 300 °C under nitrogen, (b) 400 °C under air, and (c) 600 °C under air.

TEM confirmed the mesoporosity of calcined WAl-TMS14 (Figure 5.18). The pores measured about 7-8 nm, and were arranged with no long-range ordering. The wall thickness was approximately 5-7 nm. As Al_{13} polycations are much smaller (~1 nm), the pore walls cannot be composed of a single layer of Al_{13} colloid particles. This does not preclude the possibility of the pore walls being composed of aggregates of Al_{13}.

The effects of pH and Al^{3+} concentration on WAl-TMS14 synthesis were studied in order to illustrate the importance of Al_{13} (Table 5.4). A highly concentrated Al^{3+} solution (2.8 M) combined with P123/AWO solution led to the precipitation of a mesostructured WAl-TMS14 (Figure 5.19(a)). In addition to the main SAXS peak (d_{100} = 11.6 nm), smaller peaks were found at higher 2θ angles. Their calculated Bragg spacings are 1/2 and 1/3 of 11.6 nm, indicating that the mesostructure is a lamellar phase. Such a mesophase would be structurally unstable to surfactant removal, which was confirmed by the loss of all SAXS peaks after calcination at 250 °C (Figure 5.19(b)).

The use of a lower concentration of Al^{3+} solution (0.45 M) did not result in precipitation at all. The reason is likely due to the higher pH of the synthesis mixture (~4.5), rather than its dilution.

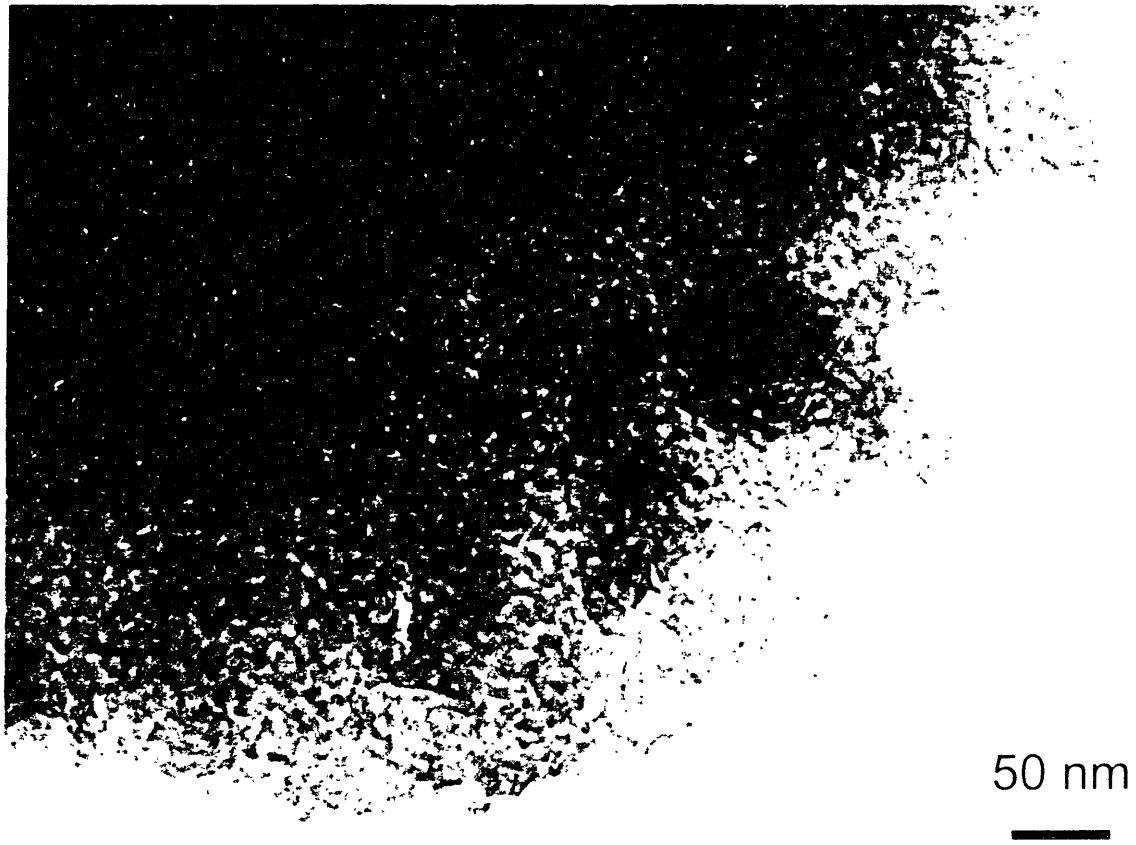

Figure 5.18 TEM image of W-Al-TMS14 calcined at 300 °C under nitrogen

Table 5.4 Effect of pH on the synthesis of W-Al-TMS14

Concentration of Al Solution (M)	pH of Final Mixture	Bragg Spacings of Mesostructure (nm)
2.8	0.5	11.6, 5.9, 3.9
0.45	4.5	
0.45 (with NaOH)	5	14.0

However, precipitation of the W-Al-TMS14 mesostructure was obtained at a slightly higher pH of 5 using the 0.45 M Al – NaOH addition. This sol contained colloidal alumina, suggesting that the Al_{13} polycations participated in the formation of W-Al-TMS14 and that Al^{3+} alone would not result in W-Al-TMS14. Very little NaOH was added to the 0.45 M Al solution that the pH increased only slightly, and so any effect of increased electrolyte amount from the Na^+ cations was negligible.

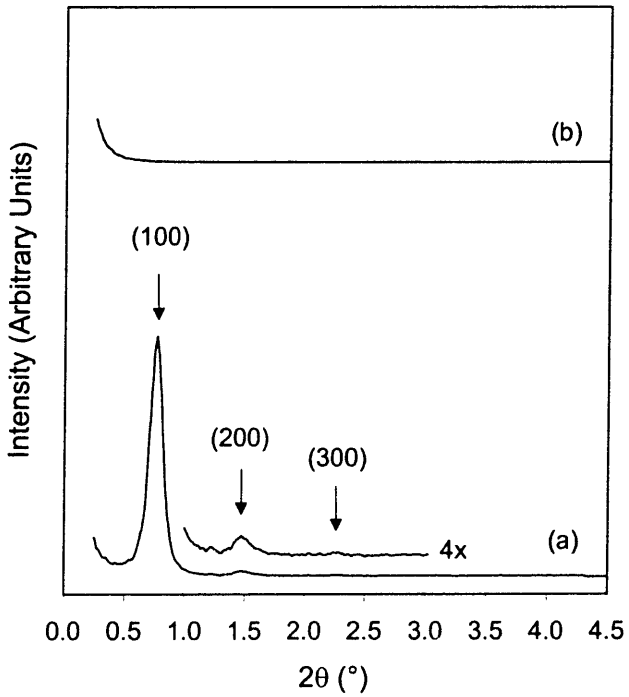

Figure 5.19. SAXS patterns of WAl-TMS14 prepared with 2.8 M Al^{3+} solution, (a) before and (b) after calcination at 250 °C in nitrogen.

5.3.4 Generalized Colloid/Surfactant Templating Mechanism

The supramolecular-templated materials of WZr-TMS14, WTi-TMS14 and WAl-TMS14 materials are mesostructured and are stable to surfactant removal, but their microstructure and physical properties differ significantly. There are intrinsic chemical differences among the metal oxides, which manifest during the supramolecular templating synthesis. In the colloid/surfactant templating mechanism, the point of zero charge, or pzc, is a critical material-dependent property. In general, insoluble metal oxides develop a surface charge when placed in water [15]. On the surface are hydroxyl groups that can interact with water in the following manner:

$$-M-OH + H_2O \leftrightarrow -M-OH_2^+ + OH^-$$

$$-M-OH + H_2O \leftrightarrow -M-O^- + H_3O^+$$

where M represents a metal cation. These surface reactions are a function of pH, and the pzc is the pH corresponding to a zero net charge for the metal oxide surface. If the pH of the aqueous solution is above the pzc for a particular metal oxide, the metal oxide surface will be negatively charged, and vice-versa. The pzc can be interpreted as a measure of the surface acidity or basicity of a metal oxide.

The pzc's for the various metal oxides of interest are listed in Table 5.5. There is a rather wide range in experimentally-determined pzc values for many reasons, such as inhomogeneous test samples, surface impurities, and different measurement techniques [16]. In spite of this, it can be concluded that ZrO_2 and TiO_2 are more acidic than Al_2O_3. An empirical relation exists between the total ionization potential (IP) of a cation and pzc of the corresponding metal oxide, given by pzc = 12.22 – 0.89 × 0.09648 × IP [20].

Table 5.5. Values of pzc for various metal oxides.

Metal Oxide	pzc Values		Cation IP (eV) [19]	Calculated pzc [20]
ZrO_2	4-6.7	[16]	77.09	5.6
	8.2	[17]		
TiO_2	4.8-6.7	[16]	91.16	4.4
	5.1	[1]		
Al_2O_3	7.7-9.4	[16]	53.26	7.6
	8.5	[18]		

In the preparation of mesoporous tungstated metal oxides, the synthesis pH was held below the pzc of the metal oxides, allowing for the colloid nanoparticles to assume a positive charge needed for favorable electrostatic interactions to occur. Our supramolecular templating model does not take into account other potentially important factors, however, and this may be responsible for the differences seen among the different tungstated metal oxides. It is noted that surface charge is also affected by electrolyte concentration in solution and by adsorption of ions on the particle surface [15]. The effective surface charge of the nanoparticles, characterized by the zeta potential [21], would thus differ among the metal oxides. Also, the colloid nanoparticles appear to be very reactive, e.g. can undergo dissolution, phase transformation, and grain growth.

More investigation into the colloid/surfactant templating route revealed some interesting insights into the mechanism. Instead of either a metal salt or metal oxide colloid solution, a 10 wt% nitric acid solution was added to an AWO/P123 surfactant synthesis solution. After two days of aging at room temperature, a translucent gel was obtained. The recovered gel was dried at room temperature and then at 95 °C for several days. This product was mesostructured, as indicated by a single SAXS peak with a Bragg spacing of 9.8 nm (Table 5.6). Calcination at 400 °C under flowing air (ramp = 2 °C/min; soak time = 3 hr)

yielded a yellow tungsten oxide powder with a grain size of 11 nm (Figure 5.20). Nitrogen adsorption analysis gave a BET surface area of 53 m^2/g and a BJH pore size of 5.0 nm, but no mesoporous structure was observed through TEM analysis.

Table 5.6. Tungsten amount in various WM-TMS14 materials.

Primary Metal Oxide	Metal Oxide Precursor	Bragg Spacing[a] (nm)	W^{6+}/M^{n+} Ratio[b]
ZrO_2	Colloidal ZrO_2	11.5	0.31[c]
	$ZrCl_4$	10.6	4.41
	$ZrO(NO_3)_2$	10.6	2.45
TiO_2	Colloidal TiO_2	10.8	0.51
Al_2O_3	Colloidal Al_2O_3	14.0	0.48
	$AlCl_3$	11.6	1.84
None	AWO only	9.8	∞

[a]Before calcination.
[b]Determined through HRTEM/EDS system.
[c]Deviation from the bulk value (0.23) due to batch-to-batch variations.

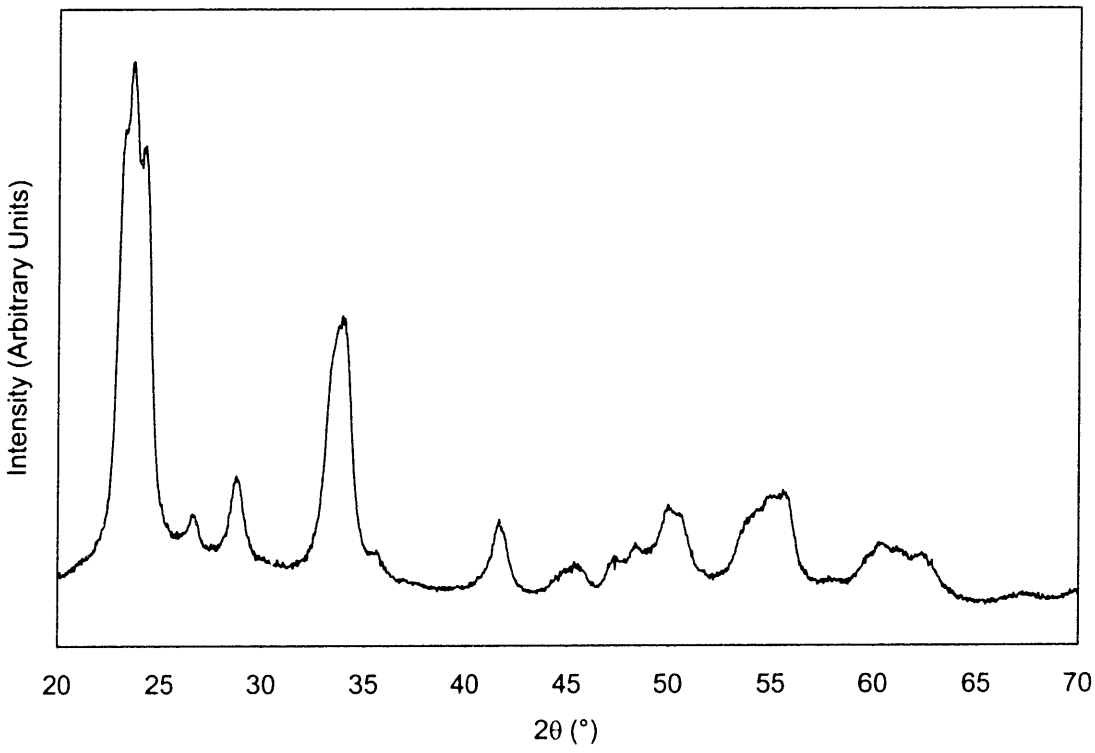

Figure 5.20. XRD pattern of nanocrystalline WO_3 calcined at 400 °C under air.

Compatible with the colloid/surfactant templating mechanism, the preparation of mesostructured tungsten oxide in this manner demonstrates that the metal salt or metal oxide

colloid precursor is not necessary for self-assembly. In this case, the negatively-charged metatungstate species act to "glue" the positively-charged surfactant micelles together.

However, to achieve materials with high thermal stability and well-defined mesopores, the addition of a metal salt or metal oxide colloid precursor is necessary. As a pure tungsten oxide mesostructure has low thermal stability, reducing the tungsten content in WM-TMS14 materials (i.e. the W^{6+}/M^{n+} ratio) would be advantageous. WZr-TMS14 materals prepared with colloidal zirconia and with zirconium salts seem to support this argument (Table 5.6). The colloid-prepared WZr-TMS14 was stable to >700 °C and had a W^{6+}/Zr^{4+} ratio of 0.31, while $ZrO(NO_3)_2$ salt-prepared WZr-TMS14 was not stable at 600 °C and had a ratio of 2.45. With an even higher value of 4.41, $ZrCl_4$ salt-prepared WZr-TMS14 could not be calcined to remove the surfactant. The same can be said for WAl-TMS14, although the material prepared with the Al^{3+} salt precursor was a layered phase and inherently had no thermal stability.

Lower W^{6+}/M^{n+} ratios appear to be associated with metal oxide colloids than with metal salts. A colloid nanoparticle has a much lower charge per cation (due to the internal cations) than a metal cation in solution would. According to our charge interaction scheme, more nanoparticles would be needed to interact with the metatungstate anions compared to metal cations, which would result in a lower W^{6+}/M^{n+} ratio. Mesostructures composed of nanoparticles have less tungstates in the framework and are more stable as a result, unlike those composed of metal salts which have more tungstates in the framework.

5.4 Summary

The supramolecular templating chemistry developed for mesoporous tungstated zirconia has been successfully extended to tungstated titania and tungstated alumina systems. Through the colloid/surfactant templating route, mesoporous WTi-TMS14 and WAl-TMS14 were achieved, respectively, although their syntheses could be optimized further for higher surface areas, narrower pore size distributions, and greater thermal stability. Synthesis parameters associated with the use of these colloidal systems were elucidated and explored, e.g. base amount, pH effect, and stability of colloid solution. The role of the metatungstate anion in "gluing" the framework together was further demonstrated. This colloid/surfactant supramolecular templating approach has been shown viable, opening opportunities to the synthesis of multicomponent metal oxides with controlled mesoporosity.

5.5 References

[1] Kormann, C.; Bahnemann, D. W.; Hoffmann, M. R. *J. Phys. Chem.* **1988**, *92*, 5196.

[2] Kim, S.-J.; Park, S.-D.; Jeong, Y. H. *J. Am. Ceram. Soc.* **1999**, *82*, 927.

[3] Wang, C.-C. Ph.D. Thesis, MIT, 2000.

[4] Wang, C.-C.; Ying, J. Y. *Chem. Mater.* **1999**, *11*, 3113.

[5] Scolan, E.; Sanchez, C. *Chem. Mater.* **1998**, *19*, 3217.

[6] Trentler, T. J.; Denler, T. E.; Bertone, J. F.; Agrawal, A.; Colvin, V. L. *J. Am. Chem. Soc.* **1999**, *121*, 1613.

[7] Nielsen, A. E. *Kinetics of Precipitation*; Macmillan: New York, 1964.

[8] Matijevic, E. *Langmuir* **1994**, *10*, 8.

[9] Ocaña, M.; Radriguez-Clemente, R.; Serna, C. J. *Adv. Mater.* **1995**, *7*, 212.

[10] Hoffmann, M. R.; Martin S. T.; Choi, W. Y.; Bahnemann, D. W. *Chem. Rev.* **1995**, *95*, 69.

[11] Alivisatos, A. P. *J. Phys. Chem.* **1996**, *100*, 13226.

[12] Empedocles, S.; Bawendi, M. *Acc. Chem. Res.* **1999**, *32*, 389.

[13] Cool, P., Vansant, E. F., in *Molecular Sieves: Science and Technology*, Vol. 1; Karge, H. G., Weitkamp J., Eds.; Springer-Verlag: Berlin, 1998; p. 265.

[14] Kloprogge, J. T.; Seykens, D.; Jansen, J. B. H.; Geus, J. W. *J. Non.-Cryst. Solids* **1992**, *142*, 94.

[15] Pugh, R. J., in *Surface and Colloid Chemistry in Advanced Ceramics Processing*; Pugh, R. J., Bergström, L., Eds.; Marcel Dekker: New York, 1994; p.127.

[16] Parks, G. A. *Chem. Rev.* **1965**, *65*, 177.

[17] Pérez-Maqueda, L. A.; Matijevic, E. *J. Mater. Res.* **1997**, 12, 3286.

[18] Park, J., Regalbuto, J. R. *J. Colloid Interface Sci.* **1995**, 175, 239.

[19] *CRC Handbook of Chemistry and Physics*, 75th Ed.; Lide, D. R., Ed.; CRC Press: Boca Raton, 1994.

[20] McHale, A. E. *Phase Diagrams and Ceramic Processes*; Chapman & Hall: New York, 1998.

[21] Hiemenz, P. C.; Rajagopalan, R. *Principles of Colloid and Surface Chemistry*, 3rd Ed.; Marcel Dekker: New York, 1997.

Chapter 6. Recommendations for Future Work

In this thesis, the application of supramolecular templating chemistry to a number of zirconia-based compositions was investigated. Materials with these compositions were created with well-defined pore sizes and higher surface areas than previously achieved through conventional catalyst preparation methods. They have been shown to exhibit surface acidity and activity for acid-catalyzed reactions. It would be of great interest to explore other applications of these new materials. Mesoporous phosphated zirconia could be an improvement upon low surface area α-zirconium phosphate as an ion-exchange material. Mesoporous and microporous zirconia-silicates showed promise as a partial oxidation catalyst for cyclooctene and could be useful for the partial oxidation of other substrates, such as cyclohexane to produce adipic acid, a precursor to nylon. Mesoporous tungstated zirconia has a high surface concentration of tungsten oxide, which was shown to lead to surface acidity for 1-butene isomerization. This material, with its high structural stability and ultrahigh dispersion of surface tungsten species, might be an excellent olefin metathesis catalyst.

Supramolecular templating was successfully studied and applied to a variety of zirconia-based compositions. The particular chemistries developed could be extended further to provide greater compositional flexibility. The covalent-bond route that used surfactants with a reactive anionic head group and zirconium n-propoxide could lead to new nanostructured compositions by using other metal precursors. For example, a carboxylate surfactant and a calcium salt might lead to a layered calcium carbonate material, and an alkylthiol and a cadmium salt might lead to a layered cadmium sulfide material.

The colloid/surfactant templating route was successfully developed for tungstated metal oxides. The synthesis strategy of using inorganic colloids could be further investigated and elaborated upon to give new classes of two-component metal oxides. Interesting possibilities include colloid sols such as cadmium sulfide quantum dots, other polyoxometallates such as tungstophosphates, and organic templating agents such as latex spheres of > 200 nm.

Chapter 7. Conclusions

Zirconia-based compositions offered great flexibility among metal oxides for tailoring surface acidity. In this thesis, three different zirconia-based materials were prepared via supramolecular templating. The derivation of nanoporous zirconia-based materials by this wet-chemical approach provided for new systems of acid catalysts with ultrahigh surface areas, well-controlled pore size, and dispersion of active species.

Each zirconia-based nanoporous system was possible through the successful development of key concepts in supramolecular templating chemistry. The covalent interaction between phosphate surfactant and zirconium alkoxide was exploited to produce mesoporous phosphated zirconia. The surface phosphates contributed to the stability of the zirconia framework and to the moderate acid strength.

Mesoporous and microporous zirconia-silicates were prepared under extremely low pH conditions. Synthesis pH and zirconium salt precursor were found to be the most important parameters in the amount of zirconium dopant incorporated. As high as 20 wt% Zr could be introduced into the silicate framework successfully through this approach. Surface sulfates on these materials contributed to their high acidic strength.

The use of zirconia colloid nanoparticles, as opposed to metal alkoxide or salt precursors, as building blocks for the inorganic framework was central to the production of stable, mesoporous tungstated zirconia. As a result of using colloid nanoparticles, the materials have a nanocrystalline framework, unlike the typical supramolecular-templated amorphous mesoporous materials. The ultrahigh dispersion of tungstate species and zirconia nanoparticles contributed to the structural stability and strong acidity of the materials. The surfactant/colloid templating approach was successfully extended to the derivation of novel tungstated titania and alumina nanoporous systems